The Dissertation Committee for Arun Kumar Tiruvannamalai Annamalai Certifies that this is the approved version of the following dissertation:

CHEMICAL, STRUCTURAL, AND ELECTROCHEMICAL CHARACTERIZATION OF 5 V SPINEL AND COMPLEX LAYERED OXIDE CATHODES OF LITHIUM ION BATTERIES

Committee:

Arumugam Manthiram, Supervisor

Desiderio Kovar

Harovel G. Wheat

Paulo Ferreira

Keith Stevenson

CHEMICAL, STRUCTURAL, AND ELECTROCHEMICAL CHARACTERIZATION OF 5 V SPINEL AND COMPLEX LAYERED OXIDE CATHODES OF LITHIUM ION BATTERIES

by

Arun Kumar Tiruvannamalai Annamalai, B.Tech.; M.S.E.

Dissertation

Presented to the Faculty of the Graduate School of
The University of Texas at Austin
in Partial Fulfillment
of the Requirements
for the Degree of

Doctor of Philosophy

The University of Texas at Austin
August 2007

Dedication

To my parents

Acknowledgements

I would like to thank my supervisor Dr. Arumugam Manthiram, for his immense support throughout the course of this work. I am deeply grateful for his patient guidance and encouragement during desperate times. I would also like to thank my committee members, Drs. Harovel Wheat, Desiderio Kovar, Paulo Ferreira, and Keith Stevenson for their helpful advice and review of my work.

I like to thank all the past and present members of Prof. Manthiram's group, in particular, Dr. Arunachala Kannan, Dr. Venkataraman Sivaramakrishnan, Dr. Jeh-won Choi, and Dr. Wonchang Choi for their support and guidance throughout my graduate studies. Above all, I like to thank Dr. Emilio Alvarez for his immense help with PGAA analysis. I also thank Welch Foundation, NASA, and DOE for financial support.

Chemical, Structural, and Electrochemical Characterization of 5 V Spinel and Complex Layered Oxide Cathodes of Lithium Ion Batteries

Publication No._____________

Arun Kumar Tiruvannamalai Annamalai, Ph.D.
The University of Texas at Austin, 2007

Supervisor: Arumugam Manthiram

Lithium ion batteries have revolutionized the portable electronics market since their commercialization first by Sony Corporation in 1990. They are also being intensively pursued for electric and hybrid electric vehicle applications. Commercial lithium ion cells are currently made largely with the layered $LiCoO_2$ cathode. However, only 50% of the theoretical capacity of $LiCoO_2$ can be utilized in practical cells due to the chemical and structural instabilities at deep charge as well as safety concerns. These drawbacks together with the high cost and toxicity of Co have created enormous interest in alternative cathodes. In this regard, spinel $LiMn_2O_4$ has been investigated widely as Mn is inexpensive and environmentally benign. However, $LiMn_2O_4$ exhibits severe capacity fade on cycling, particularly at elevated temperatures. With an aim to overcome the capacity fading problems, several cationic substitutions to give $LiMn_{2-y}M_yO_4$ (M = Cr, Fe, Co, Ni, and Cu) have been pursued in the literature. Among the cation-substituted systems, $LiMn_{1.5}Ni_{0.5}O_4$ has become attractive as it shows a high capacity of ~ 130 mAh/g (theoretical capacity: 147 mAh/g) at around 4.7 V.

With an aim to improve the electrochemical performance of the 5 V $LiMn_{1.5}Ni_{0.5}O_4$ spinel oxide, various cation-substituted $LiMn_{1.5-y}Ni_{0.5-z}M_{y+z}O_4$ (M = Li, Mg, Fe, Co, and Zn) spinel oxides have been investigated by chemical lithium extraction. The cation-substituted $LiMn_{1.5-y}Ni_{0.5-z}M_{y+z}O_4$ spinel oxides exhibit better cyclability and rate capability in the 5 V region compared to the unsubstituted $LiMn_{1.5}Ni_{0.5}O_4$ cathodes although the degree of manganese dissolution does not vary significantly. The better electrochemical properties of $LiMn_{1.5-y}Ni_{0.5-z}M_{y+z}O_4$ are found to be due to a smaller lattice parameter difference among the three cubic phases formed during the charge-discharge process. In addition, while the spinel $Li_{1-x}Mn_{1.58}Ni_{0.42}O_4$ was chemically stable, the spinel $Li_{1-x}Co_2O_4$ was found to exhibit both proton insertion and oxygen loss at deep lithium extraction due to the chemical instability arising from a overlap of the $Co^{3+/4+}$:3d band on the top of the O^{2-}:2p band.

The irreversible oxygen loss during the first charge and the consequent reversible capacities of the solid solutions between $Li[Li_{1/3}Mn_{2/3}]O_2$ and $Li[Co_{1-y}Ni_y]O_2$ has been found to be determined by the amount of lithium in the transition metal layer of the O3 type layered structure. The lithium content in the transition metal layer is, however, sensitively influenced by the tendency of Ni^{3+} to get reduced to Ni^{2+} and the consequent volatilization of lithium during synthesis. Moreover, high Mn^{4+} content causes a decrease in oxygen mobility and loss. In addition, the chemically delithiated samples were found to adopt either the parent O3 type structure or the new P3 or O1 type structures depending upon the composition and synthesis temperature of the parent samples and the proton content inserted into the delithiated sample. In essence, the chemical and structural stabilities and the electrochemical performance factors of the layered (1-z) $Li[Li_{1/3}Mn_{2/3}]O_2 \cdot$ (z) $Li[Co_{1-y}Ni_y]O_2$ solid solution cathodes are found to be maximized by optimizing the contents of the various ions.

Table of Contents

List of Tables xii

List of Figures xiii

CHAPTER 1 1

Introduction 1

- 1.1 Electrochemical power sources 1
- 1.2 Principles of electrochemical cells 2
- 1.3 Batteries 6
- 1.4 The primary battery systems 6
- 1.5 The secondary battery systems 7
  - 1.5.1 Lead-Acid battery 7
  - 1.5.2 Nickel-Cadmium battery 8
  - 1.5.3 Nickel-Metal hydride battery 9
  - 1.5.4 Lithium Ion batteries 9
- 1.6 Lithium Ion batteries 10
  - 1.6.1 Design considerations 10
  - 1.6.2 Cathode materials 14
    - 1.6.2.1 Lithium cobalt oxide ($LiCoO_2$) cathode 14
    - 1.6.2.2 Lithium nickel oxide ($LiNiO_2$) cathode 16
    - 1.6.2.3 Lithium manganese oxide ($LiMn_2O_4$) cathode 17
    - 1.6.2.4 High voltage spinel ($LiMn_{2-x}M_xO_4$) cathodes 20
    - 1.6.2.5 Other cathode materials 22
  - 1.6.3 Anode materials 24
  - 1.6.4 Electrolytes 24
  - 1.6.5 Separators 25
  - 1.6.6 Safety devices 26
- 1.7 Objectives 26

CHAPTER 2 **28**

Experimental Procedures 28
2.1 Materials synthesis 28
2.2 Chemical delithiation 28
2.3 Manganese dissolution 29
2.4 Materials characterization 29
  2.4.1 X-ray powder diffraction (XRD) 29
  2.4.2 Atomic absorption spectroscopy (AAS) 30
  2.4.3 Redox titration 30
  2.4.4 Thermogravimetric analysis (TGA) 31
  2.4.5 Scanning electron microscopy (SEM) 31
  2.4.6 Prompt gamma-ray activation analysis (PGAA) 31
2.5 Electrochemical characterization 32

CHAPTER 3 **33**

Influence of Lattice Parameter Differences on the Electrochemical Performance of the 5 V Spinel $LiMn_{1.5-y}Ni_{0.5-z}M_{y+z}O_4$ (M = Li, Mg, Fe, Co, and Zn) Cathodes 33
3.1 Introduction 33
3.2 Experimental 34
3.3 Results and discussion 35
  3.3.1 Electrochemical performance of the cation substituted 5 V spinel cathodes 35
  3.3.2 Phase transitions occurring in the 5 V $LiMn_{1.5-y}Ni_{0.5-z}M_{y+z}O_4$ cathodes during the charge-discharge process 40
  3.3.3 Influence of lattice parameter differences between the cubic phases on the capacity fade of the 5 V spinel cathodes 52
  3.3.4 Manganese ion dissolution from 5 V spinel cathodes 55
3.4 Conclusions 56

CHAPTER 4 **58**

Proton Insertion and Oxygen Loss in the Spinel Oxide Systems................................58

4.1 Introduction..58

4.2 Experimental..60

4.3 Results and discussion 61

4.3.1 Proton insertion and oxygen loss in the $Li_{1-x}Mn_{1.58}Ni_{0.42}O_4$ and $Li_{1-x}Co_2O_4$ systems..61

4.3.2 TGA analysis of the $Li_{1-x}Co_2O_4$ system..62

4.4 Conclusions..63

CHAPTER 5 **64**

Chemical and Electrochemical Characterization of Complex Layered Cathodes in the $Li[Li_{1/3}Mn_{2/3}]O_2$ - $LiCoO_2$ - $LiNiO_2$ Solid Solution 64

5.1 Introduction..64

5.2 Experimental..65

5.3 Results and discussion 66

5.3.1 (1-z) $Li[Li_{1/3}Mn_{2/3}]O_2 \cdot$ (z) $Li[Co_{1-y}Ni_y]O_2$ ($0 \leq y \leq 1$ and $z = 0.5$) series synthesized at 900 °C..66

5.3.1.1 Crystal chemistry 66

5.3.1.2 Electrochemical performance 71

5.3.1.3 Chemical stability of delithiated samples 73

5.3.2 (1-z) $Li[Li_{1/3}Mn_{2/3}]O_2 \cdot$ (z) $Li[Co_{1-y}Ni_y]O_2$ ($0 \leq y \leq 1$ and $z = 0.5$) series synthesized at 750 °C..77

5.3.2.1 Crystal chemistry 77

5.3.2.2 Electrochemical performance 80

5.3.3 (1-z) $Li[Li_{1/3}Mn_{2/3}]O_2 \cdot$ (z) $Li[Co_{1-y}Ni_y]O_2$ ($0 \leq y \leq 1$ and $z = 0.7$) series synthesized at 900 °C..84

5.3.3.1 Crystal chemistry 84

5.3.3.2 Chemical stability of delithiated samples 88

  - 5.3.4 (1-z) $Li[Li_{1/3}Mn_{2/3}]O_2 \cdot (z) Li[Co_{1-y}Ni_y]O_2$ ($y = 0.5$ and $0.2 \leq z \leq 0.7$) series synthesized at 900 °C........89
    - 5.3.4.1 Crystal chemistry........89
    - 5.3.4.2 Electrochemical performance........93
    - 5.3.4.3 Chemical stability of delithiated samples........95
  - 5.3.5 (1-z) $Li[Li_{1/3}Mn_{2/3}]O_2 \cdot (z) Li[Co_{1-y}Ni_y]O_2$ ($y = 0.5$ and $0.2 \leq z \leq 0.7$) series synthesized at 750 °C........98
    - 5.3.5.1 Crystal chemistry........98
    - 5.3.5.2 Electrochemical performance........100
    - 5.3.5.3 Chemical stability of delithiated samples........104
  - 5.3.6 Correlation between lithium content in the transition metal layer and oxygen loss in the $Li[Li_{1/3}Mn_{2/3}]O_2 – LiCoO_2 – LiNiO_2$ solid solution cathodes........107
- 5.4 Conclusions........112

CHAPTER 6 **114**

Structural Stability of Chemically Delithiated $Li[Li_{1/3}Mn_{2/3}]O_2 – LiCoO_2 – LiNiO_2$ Solid Solution Oxides........114
- 6.1 Introduction........114
- 6.2 Experimental........116
- 6.3 Results and discussion........117
  - 6.3.1 Structural stability of chemically delithiated (1-z) $Li[Li_{1/3}Mn_{2/3}]O_2 \cdot (z) Li[Co_{1-y}Ni_y]O_2$ ($0 \leq y \leq 1$ and $0 \leq z \leq 1$) solid solution oxides........117
  - 6.3.2 Influence of proton content and cation disorder on phase transformations........130
- 6.4 Conclusions........133

CHAPTER 7 **134**

Summary........134

References........137

Vita........146

List of Tables

Table 1.1: The primary battery systems. 7

Table 1.2: The secondary battery systems. 8

Table 3.1: Manganese dissolution in spinel oxide cathodes. 56

Table 4.1: Chemical analysis and PGAA data of the chemically delithiated (with NO_2BF_4 in acetonitrile medium) spinel oxide cathodes. 61

Table 5.1: Observed chemical compositions and electrochemical data of (1-z) $Li[Li_{1/3}Mn_{2/3}]O_2 \cdot$ (z) $Li[Co_{1-y}Ni_y]O_2$ ($0 \le y \le 1$ and $z = 0.5$) samples synthesized at 900 °C. 68

Table 5.2: Chemical analysis data of chemically delithiated (1-z) $Li[Li_{1/3}Mn_{2/3}]O_2 \cdot$ (z) $Li[Co_{1-y}Ni_y]O_2$ ($0 \le y \le 1$ and $z = 0.5$) samples synthesized at 900°C. ..75

Table 5.3: Observed chemical compositions and electrochemical data of (1-z) $Li[Li_{1/3}Mn_{2/3}]O_2 \cdot$ (z) $Li[Co_{1-y}Ni_y]O_2$ ($0 \le y \le 1$ and $z = 0.5$) samples synthesized at 750 °C. 79

Table 5.4: Observed chemical compositions of the parent and chemically delithiated (1-z) $Li[Li_{1/3}Mn_{2/3}]O_2 \cdot$ (z) $Li[Co_{1-y}Ni_y]O_2$ ($0 \le y \le 1$ and $z = 0.7$) samples synthesized at 900 °C. 85

Table 5.5: Observed chemical compositions and electrochemical data of (1-z) $Li[Li_{1/3}Mn_{2/3}]O_2 \cdot$ (z) $Li[Co_{1-y}Ni_y]O_2$ ($y = 0.5$ and $0.2 \le z \le 0.7$) samples synthesized at 900 °C. 92

Table 5.6: Chemical analysis data of chemically delithiated (1-z) $Li[Li_{1/3}Mn_{2/3}]O_2 \cdot$ (z) $Li[Co_{1-y}Ni_y]O_2$ ($y = 0.5$ and $0.2 \le z \le 0.7$) samples synthesized at 900 °C 97

Table 5.7: Observed chemical compositions and electrochemical data of (1-z) $Li[Li_{1/3}Mn_{2/3}]O_2 \cdot$ (z) $Li[Co_{1-y}Ni_y]O_2$ ($y = 0.5$ and $0.2 \le z \le 0.7$) samples synthesized at 750 °C. 101

Table 5.8: Chemical analysis data of chemically delithiated (1-z) $Li[Li_{1/3}Mn_{2/3}]O_2 \cdot$ (z) $Li[Co_{1-y}Ni_y]O_2$ ($y = 0.5$ and $0.2 \le z \le 0.7$) samples synthesized at 750 °C. 106

Table 5.9: Observed chemical compositions of the parent and chemically delithiated (1-z) $Li[Li_{1/3}Mn_{2/3}]O_2 \cdot$ (z) $Li[Co_{1-y}Ni_y]O_2$ ($0 \le y \le 1$ and $0 \le z \le 1$) samples synthesized at 900 °C. 108

List of Figures

Figure 1.1: Schematic representation of an electrochemical cell. 2

Figure 1.2: Variation of cell voltage with operating current illustrating polarization losses: (a) ohmic polarization, (b) activation polarization, and (c) concentration polarization. 4

Figure 1.3: Comparison of the gravimetric and volumetric energy densities of popular rechargeable battery systems. 10

Figure 1.4: Relative energy diagram of a lithium cell at open circuit. 11

Figure 1.5: Schematic illustration of the charge/discharge process in a rechargeable lithium ion battery. 12

Figure 1.6: Crystal structure of $LiCoO_2$ having the O3 type layered structure. The Li^+ ions occupy the octahedral interstitial sites between the CoO_2 layers....15

Figure 1.7: Comparison of the qualitative energy diagrams of $Li_{0.5}CoO_2$, $Li_{0.5}NiO_2$, and $Li_{0.5}Mn_2O_4$. 16

Figure 1.8: Crystal structure of $LiMn_2O_4$ spinel. The Li^+ ions occupy the tetrahedral interstitial sites of the MnO_6 octahedra framework. 18

Figure 1.9: Cubic to tetragonal (Jahn-Teller) distortion arising from Mn^{3+}:$3d^4$ due to the single electron present in the e_g orbital. 19

Figure 1.10: The first discharge curves of the 5 V cation substituted $LiMn_{2-x}M_xO_4$ (M= Cr, Co, Ni, Fe, and Cu) spinel oxides. 21

Figure 1.11: Crystal structure of olivine $LiFePO_4$ 22

Figure 1.12: Rate capability of the 5 V olivine $LiCoPO_4$ 23

Figure 3.1: X-ray diffraction patterns of (a) $LiMn_{1.5}Ni_{0.5}O_4$, (b) $LiMn_{1.58}Ni_{0.42}O_4$ and (c) $Li_{1.053}Mn_{1.527}Ni_{0.42}O_2$ synthesized by the hydroxide precursor method. The reflections marked with (hkl) values refer to spinel and those marked with * refer to the impurity phase $Li_xNi_{1-x}O$. 36

Figure 3.2: First discharge profiles of $LiMn_{1.5}Ni_{0.5}O_4$, $LiMn_{1.58}Ni_{0.42}O_4$ and $Li_{1.053}Mn_{1.527}Ni_{0.42}O_2$, recorded at a current density of 0.2 mA/cm^2 between 5 and 3.5 V..37

Figure 3.3: Comparison of the cycling performances of the $LiMn_{1.58}Ni_{0.42}O_4$ and $Li_{1.053}Mn_{1.527}Ni_{0.42}O_2$ cathodes with that of $LiMn_{1.5}Ni_{0.5}O_4$. The data were collected at a current density of 0.2 mA/cm^2 between 5.0 - 3.5 V.......38

Figure 3.4: Comparison of the cycling performances of the cation substituted spinel $LiMn_{1.5-y}Ni_{0.5-z}M_{y+z}O_4$ (M = Li, Fe, Co, and Zn) cathodes with that of $LiMn_{1.5}Ni_{0.5}O_4$. The data were collected at a current density of 0.2 mA/cm^2 between 5.0 and 3.5 V at room temperature.................................39

Figure 3.5: Comparison of the discharge profiles of $LiMn_{1.5}Ni_{0.5}O_4$ and $LiMn_{1.42}Ni_{0.42}Co_{0.16}O_4$ at various rates, illustrating the rate capability. 40

Figure 3.6: X-ray diffraction patterns of the 4 V spinel $Li_{1-x}Mn_2O_4$ samples that were obtained by chemically extracting lithium with NO_2BF_4. 41

Figure 3.7: Variations of the lattice parameters with lithium content (1-x) in $Li_{1-x}Mn_2O_4$: first cubic phase (■) and second cubic phase (○). 41

Figure 3.8: X-ray diffraction patterns of the 5 V spinel $Li_{1-x}Mn_{1.5}Ni_{0.5}O_4$ samples that were obtained by chemically extracting lithium with NO_2BF_4. 42

Figure 3.9: Variations of the lattice parameters with lithium content (1-x) in $Li_{1-x}Mn_{1.5}Ni_{0.5}O_4$: first cubic phase (■); second cubic phase (○); and third cubic phase (▲)..42

Figure 3.10: X-ray diffraction patterns of the 5 V spinel $Li_{1-x}Mn_{1.5}Ni_{0.5}O_4$ samples that were obtained by electrochemically extracting lithium........................43

Figure 3.11: X-ray diffraction patterns of the 5 V spinel $Li_{1-x}Mn_{1.58}Ni_{0.42}O_4$ samples that were obtained by chemically extracting lithium with NO_2BF_4. 44

Figure 3.12: Variations of the lattice parameters with lithium content (1-x) in $Li_{1-x}Mn_{1.58}Ni_{0.42}O_4$: first cubic phase (■); second cubic phase (○); and third cubic phase (▲)..44

Figure 3.13: X-ray diffraction patterns of the 5 V spinel $Li_{1-x}Li_{0.053}Mn_{1.527}Ni_{0.42}O_4$ samples that were obtained by chemically extracting lithium with NO_2BF_4. 45

Figure 3.14: Variations of the lattice parameters with lithium content (1-x) in $Li_{1-x}Li_{0.053}Mn_{1.527}Ni_{0.42}O_4$: first cubic phase (■); second cubic phase (○); and third cubic phase (▲)...45

Figure 3.15: X-ray diffraction patterns of the 5 V spinel $Li_{1-x}Mn_{1.5}Ni_{0.42}Mg_{0.08}O_4$ samples that were obtained by chemically extracting lithium with NO_2BF_4. 46

Figure 3.16: Variations of the lattice parameters with lithium content (1-x) in $Li_{1-x}Mn_{1.5}Ni_{0.42}Mg_{0.08}O_4$: first cubic phase (■); second cubic phase (○); and third cubic phase (▲). 46

Figure 3.17: X-ray diffraction patterns of the 5 V spinel $Li_{1-x}Li_{0.026}Mn_{1.474}Ni_{0.42}Fe_{0.08}O_4$ samples that were obtained by chemically extracting lithium with NO_2BF_4. 47

Figure 3.18: Variations of the lattice parameters with lithium content (1-x) in $Li_{1-x}Li_{0.026}Mn_{1.474}Ni_{0.42}Fe_{0.08}O_4$: first cubic phase (■); second cubic phase (○); and third cubic phase (▲). 47

Figure 3.19: X-ray diffraction patterns of the 5 V spinel $Li_{1-x}Mn_{1.42}Ni_{0.42}Fe_{0.16}O_4$ samples that were obtained by chemically extracting lithium with NO_2BF_4. 48

Figure 3.20: Variations of the lattice parameters with lithium content (1-x) in $Li_{1-x}Mn_{1.42}Ni_{0.42}Fe_{0.16}O_4$: first cubic phase (■); second cubic phase (○); and third cubic phase (▲). 48

Figure 3.21: X-ray diffraction patterns of the 5 V spinel $Li_{1-x}Li_{0.026}Mn_{1.474}Ni_{0.42}Co_{0.08}O_4$ samples that were obtained by chemically extracting lithium with NO_2BF_4. 49

Figure 3.22: Variations of the lattice parameters with lithium content (1-x) in $Li_{1-x}Li_{0.026}Mn_{1.474}Ni_{0.42}Co_{0.08}O_4$: first cubic phase (■); second cubic phase (○); and third cubic phase (▲). 49

Figure 3.23: X-ray diffraction patterns of the 5 V spinel $Li_{1-x}Mn_{1.42}Ni_{0.42}Co_{0.16}O_4$ samples that were obtained by chemically extracting lithium with NO_2BF_4. 50

Figure 3.24: Variations of the lattice parameters with lithium content (1-x) in $Li_{1-x}Mn_{1.42}Ni_{0.42}Co_{0.16}O_4$: first cubic phase (■); second cubic phase (○); and third cubic phase (▲). 50

Figure 3.25: X-ray diffraction patterns of the 5 V spinel $Li_{1-x}Mn_{1.5}Ni_{0.42}Zn_{0.08}O_4$ samples that were obtained by chemically extracting lithium with NO_2BF_4. 51

Figure 3.26: Variations of the lattice parameters with lithium content (1-x) in $Li_{1-x}Mn_{1.5}Ni_{0.42}Zn_{0.08}O_4$: first cubic phase (■); second cubic phase (○); and third cubic phase (▲). 51

Figure 3.27: Variations of the lattice parameters with lithium content (1-x) in $Li_{1-x}Mn_{1.5}Ni_{0.5}O_4$ and $Li_{1-x}Mn_{1.42}Ni_{0.42}Co_{0.16}O_4$: first cubic phase (■); second cubic phase (○); and third cubic phase (▲).....................................53

Figure 3.28: Correlation of the % capacity loss to the lattice parameter difference between the cubic phases formed during the charge-discharge process of the 5 V $LiMn_{1.5-y}Ni_{0.5-z}M_{y+z}O_4$ (M = Li, Mg, Fe, Co, and Zn) cathodes investigated in this study. Δa_1 is the maximum lattice parameter differences between the first and second cubic phases and Δa_2 is that between the second and third cubic phases formed during the charge-discharge process. (1) $Li_{1-x}Mn_{1.42}Ni_{0.42}Co_{0.16}O_4$,
(2) $Li_{1-x}Mn_{1.5}Ni_{0.42}Zn_{0.08}O_4$, (3) $Li_{1-x}Mn_{1.42}Ni_{0.42}Fe_{0.16}O_4$,
(4) $Li_{1-x}Li_{0.026}Mn_{1.474}Ni_{0.42}Co_{0.08}O_4$, (5) $Li_{1-x}Mn_{1.5}Ni_{0.42}Mg_{0.08}O_4$,
(6) $Li_{1-x}Li_{0.026}Mn_{1.474}Ni_{0.42}Fe_{0.08}O_4$, (7) $Li_{1-x}Mn_{1.58}Ni_{0.42}O_4$,
(8) $Li_{1-x}Li_{0.053}Mn_{1.527}Ni_{0.42}O_4$, and (9) $Li_{1-x}Mn_{1.5}Ni_{0.5}O_4$.............................54

Figure 4.1: Comparisons of the variations of the average oxidation state of the transition metal ions with lithium content (1-x) in $Li_{1-x}Ni_{1-y-z}Mn_yCo_zO_2$. The solid line refers to the theoretically expected oxidation state...............59

Figure 4.2: TGA plot of chemically delithiated $Li_{1-x}Co_2O_4$ oxide.................................62

Figure 5.1: Phase diagram of the $Li[Li_{1/3}Mn_{2/3}]O_2$ - $LiCoO_2$ - $LiNiO_2$ system. The compositions studied in the (1-z) $Li[Li_{1/3}Mn_{2/3}]O_2 \cdot$ (z) $Li[Co_{1-y}Ni_y]O_2$ ($0 \leq y \leq 1$ and $z = 0.5$) system are indicated by closed circles. 67

Figure 5.2: XRD patterns of (1-z) $Li[Li_{1/3}Mn_{2/3}]O_2 \cdot$ (z) $Li[Co_{1-y}Ni_y]O_2$ ($0 \leq y \leq 1$ and $z = 0.5$) samples synthesized at 900 °C. 69

Figure 5.3: Variations of the lattice parameters *a* and *c*, *c/a* ratio, and cation disorder (fraction of lithium sites occupied by transition metal ions in the lithium layer) with y in (1-z) $Li[Li_{1/3}Mn_{2/3}]O_2 \cdot$ (z) $Li[Co_{1-y}Ni_y]O_2$ ($0 \leq y \leq 1$ and $z = 0.5$) samples synthesized at 900 °C. 70

Figure 5.4: Comparison of the first charge-discharge profiles (recorded at 12.5 mA/g between 2.0 - 4.8 V) of the (1-z) $Li[Li_{1/3}Mn_{2/3}]O_2 \cdot$ (z) $Li[Co_{1-y}Ni_y]O_2$ ($0 \leq y \leq 1$ and $z = 0.5$) samples synthesized at 900 °C. The dashed vertical lines separate the initial sloping region A from the plateau region B. 72

Figure 5.5: Comparison of the cyclability data (12.5 mA/g between 2.0 – 4.8 V) of the (1-z) $Li[Li_{1/3}Mn_{2/3}]O_2 \cdot$ (z) $Li[Co_{1-y}Ni_y]O_2$ ($0 \leq y \leq 1$ and $z = 0.5$) samples synthesized at 900 °C. 73

Figure 5.6: XRD patterns of (1-z) $Li[Li_{1/3}Mn_{2/3}]O_2 \cdot$ (z) $Li[Co_{1-y}Ni_y]O_2$ ($0 \leq y \leq 1$ and $z = 0.5$) samples synthesized at 750 °C. 77

Figure 5.7: Variations of the lattice parameters *a* and *c*, *c/a* ratio, and cation disorder with y in (1-z) $Li[Li_{1/3}Mn_{2/3}]O_2 \cdot$ (z) $Li[Co_{1-y}Ni_y]O_2$ ($0 \leq y \leq 1$ and $z = 0.5$) samples synthesized at 750 °C. 78

Figure 5.8: Comparison of the first charge-discharge profiles (recorded at 12.5 mA/g between 2.0 - 4.8 V) of the (1-z) $Li[Li_{1/3}Mn_{2/3}]O_2 \cdot$ (z) $Li[Co_{1-y}Ni_y]O_2$ ($0 \leq y \leq 1$ and $z = 0.5$) samples synthesized at 750 °C. The dashed vertical lines separate the initial sloping region A from the plateau region B. 81

Figure 5.9: Comparison of the cyclability data (12.5 mA/g between 2.0 – 4.8 V) of the (1-z) $Li[Li_{1/3}Mn_{2/3}]O_2 \cdot$ (z) $Li[Co_{1-y}Ni_y]O_2$ ($0 \leq y \leq 1$ and $z = 0.5$) samples synthesized at 750 °C. 82

Figure 5.10: XRD patterns of (1-z) $Li[Li_{1/3}Mn_{2/3}]O_2 \cdot$ (z) $Li[Co_{1-y}Ni_y]O_2$ ($0 \leq y \leq 1$ and $z = 0.5$; synthesized at 750 °C) cathodes after 20 cycles......83

Figure 5.11: Phase diagram of the $Li[Li_{1/3}Mn_{2/3}]O_2$ - $LiCoO_2$ - $LiNiO_2$ system. The compositions studied in the (1-z) $Li[Li_{1/3}Mn_{2/3}]O_2 \cdot$ (z) $Li[Co_{1-y}Ni_y]O_2$ ($0 \leq y \leq 1$ and $z = 0.7$) system are indicated by closed circles. 84

Figure 5.12: XRD patterns of (1-z) $Li[Li_{1/3}Mn_{2/3}]O_2 \cdot$ (z) $Li[Co_{1-y}Ni_y]O_2$ ($0 \leq y \leq 1$ and $z = 0.7$) samples synthesized at 900 °C. 86

Figure 5.13: Variations of the lattice parameters *a* and *c*, *c/a* ratio, and cation disorder (fraction of lithium sites occupied by transition metal ions in the lithium layer) with y in (1-z) $Li[Li_{1/3}Mn_{2/3}]O_2 \cdot$ (z) $Li[Co_{1-y}Ni_y]O_2$ ($0 \leq y \leq 1$ and $z = 0.7$) samples synthesized at 900 °C. 87

Figure 5.14: Phase diagram of the $Li[Li_{1/3}Mn_{2/3}]O_2$ - $LiCoO_2$ - $LiNiO_2$ system. The compositions studied in the (1-z) $Li[Li_{1/3}Mn_{2/3}]O_2 \cdot$ (z) $Li[Co_{1-y}Ni_y]O_2$ ($y = 0.5$ and $0.2 \leq z \leq 0.7$) system are indicated by closed circles. 89

Figure 5.15: XRD patterns of the (1-z) $Li[Li_{1/3}Mn_{2/3}]O_2 \cdot$ (z) $Li[Co_{1-y}Ni_y]O_2$ ($y = 0.5$ and $0.2 \leq z \leq 0.7$) samples synthesized at 900 °C. The expanded region on the right shows the superstructure reflections arising from an ordering among Li^+, Mn^{4+}, and Ni^{2+}. 90

Figure 5.16: Variations of the unit cell parameters with z in the (1-z) $Li[Li_{1/3}Mn_{2/3}]O_2 \cdot$ (z) $Li[Co_{1-y}Ni_y]O_2$ ($y = 0.5$ and $0.2 \leq z \leq 0.7$) samples synthesized at 900 °C...91

Figure 5.17: Comparison of the first charge-discharge profiles (recorded at 12.5 mA/g between 2.0 – 4.8 V) of the (1-z) $Li[Li_{1/3}Mn_{2/3}]O_2 \cdot$ (z) $Li[Co_{1-y}Ni_y]O_2$ (y = 0.5 and $0.2 \leq z \leq 0.7$) samples synthesized at 900 °C. The dashed vertical lines separate the initial sloping region A from the plateau region B. 94

Figure 5.18: Comparison of the cyclability data (12.5 mA/g between 2.0 – 4.8 V) of the (1-z) $Li[Li_{1/3}Mn_{2/3}]O_2 \cdot$ (z) $Li[Co_{1-y}Ni_y]O_2$ (y = 0.5 and $0.2 \leq z \leq 0.7$) samples synthesized at 900 °C. 95

Figure 5.19: XRD patterns of the (1-z) $Li[Li_{1/3}Mn_{2/3}]O_2 \cdot$ (z) $Li[Co_{1-y}Ni_y]O_2$ (y = 0.5 and $0.2 \leq z \leq 0.7$) samples synthesized at 750 °C. The expanded region on the right shows the superstructure reflections arising from an ordering among Li^+, Mn^{4+}, and Ni^{2+}. 98

Figure 5.20: Variations of the unit cell parameters with z in the (1-z) $Li[Li_{1/3}Mn_{2/3}]O_2 \cdot$ (z) $Li[Co_{1-y}Ni_y]O_2$ (y = 0.5 and $0.2 \leq z \leq 0.7$) samples synthesized at 750 °C. 99

Figure 5.21: Comparison of the first charge-discharge profiles (recorded at 12.5 mA/g between 2.0 – 4.8 V) of the (1-z) $Li[Li_{1/3}Mn_{2/3}]O_2 \cdot$ (z) $Li[Co_{1-y}Ni_y]O_2$ (y = 0.5 and $0.2 \leq z \leq 0.7$) samples synthesized at 750 °C. The dashed vertical lines separate the initial sloping region A from the plateau region B. 102

Figure 5.22: Comparison of the cyclability data (12.5 mA/g between 2.0 – 4.8 V) of the (1-z) $Li[Li_{1/3}Mn_{2/3}]O_2 \cdot$ (z) $Li[Co_{1-y}Ni_y]O_2$ (y = 0.5 and $0.2 \leq z \leq 0.7$) samples synthesized at 750 °C. 103

Figure 5.23: SEM images of the (1-z) $Li[Li_{1/3}Mn_{2/3}]O_2 \cdot$ (z) $Li[Co_{1-y}Ni_y]O_2$ (y = 0.5 and z = 0.2) sample synthesized at (a) 900 °C and (b) 750 °C. 105

Figure 5.24: Phase diagram of the $Li[Li_{1/3}Mn_{2/3}]O_2$ - $LiCoO_2$ - $LiNiO_2$ system. The compositions studied in this section are indicated by open circles, while the composition studied in the previous sections are indicated by closed circles. 107

Figure 5.25: Correlation between lithium content in the transition metal layer and oxygen loss in the $Li[Li_{1/3}Mn_{2/3}]O_2$ – $LiCoO_2$ – $LiNiO_2$ solid solution cathodes. (a) $Li[Li_{0.08}Mn_{0.37}Ni_{0.55}]O_2$, (b) $Li[Li_{0.10}Mn_{0.36}Co_{0.13}Ni_{0.41}]O_2$, (c) $Li[Li_{0.21}Mn_{0.48}Co_{0.155}Ni_{0.155}]O_2$, (d) $Li[Li_{0.23}Mn_{0.47}Co_{0.15}Ni_{0.15}]O_2$, (e) $Li[Li_{0.2}Mn_{0.49}Ni_{0.31}]O_2$, (f) $Li[Li_{0.23}Mn_{0.47}Co_{0.3}]O_2$, (g) $Li[Li_{0.27}Mn_{0.53}Co_{0.1}Ni_{0.1}]O_2$, and (h) $Li[Li_{0.33}Mn_{0.67}]O_2$. 111

Figure 6.1: Crystal structures of (a) O3 type $LiMO_2$, (b) P3 type MO_2, and (c) O1 type MO_2 viewed along the (100) plane. 115

Figure 6.2: Phase diagram of the $Li[Li_{1/3}Mn_{2/3}]O_2$ - $LiCoO_2$ - $LiNiO_2$ system. The compositions studied in the (1-z) $Li[Li_{1/3}Mn_{2/3}]O_2 \cdot$ (z) $Li[Co_{1-y}Ni_y]O_2$ ($0 \le y \le 1$ and $0 \le z \le 1$) system are indicated by closed circles. 117

Figure 6.3: XRD patterns of the chemically delithiated samples obtained from the (1-z) $Li[Li_{1/3}Mn_{2/3}]O_2 \cdot$ (z) $Li[Co_{1-y}Ni_y]O_2$ (y = 0 and $0 \le z \le 1$) series synthesized at 900 °C. The reflections marked with hkl values refer to the layered O3 phase and those marked with o refer to the P3 phase. (a) $Li_{0.98}H_{0.02}[Li_{0.33}Mn_{0.67}]O_{2.01}$, (b) $Li_{0.26}H_{0.17}[Li_{0.23}Mn_{0.47}Co_{0.3}]O_{1.78}$, (c) $Li_{0.04}H_{0.18}[Li_{0.17}Mn_{0.33}Co_{0.5}]O_{1.66}$, (d) $Li_{0.07}H_{0.24}[Li_{0.1}Mn_{0.2}Co_{0.7}]O_{1.78}$, (e) $Li_{0.04}H_{0.44}[Li_{0.06}Mn_{0.13}Co_{0.81}]O_{1.88}$, (f) $Li_{0.02}H_{0.36}[Li_{0.02}Mn_{0.07}Co_{0.91}]O_{1.94}$, and (g) $Li_{0.02}H_{0.40}[Co]O_{1.99}$............119

Figure 6.4: Rietveld fitting of the X-ray diffraction data of the chemically delithiated (1-z) $Li[Li_{1/3}Mn_{2/3}]O_2 \cdot$ (z) $Li[Co_{1-y}Ni_y]O_2$ (y = 0 and z = 0.9) sample synthesized at 900 °C. $a = 2.8399(8)$ Å, $c = 13.597(9)$ Å, $V = 94.97(7)$ Å^3, $R_{wp} = 12.21$ %, $R_p = 9.51$ %, and $s = 2.13$. Squares and lines correspond, respectively, to the observed and calculated intensities. The difference between the observed and calculated patterns and the peak positions corresponding to the P3 type phase are also shown. 120

Figure 6.5: XRD patterns of the chemically delithiated samples obtained from the (1-z) $Li[Li_{1/3}Mn_{2/3}]O_2 \cdot$ (z) $Li[Co_{1-y}Ni_y]O_2$ (y = 0.25 and $0 \le z \le 1$) series synthesized at 900 °C. The reflections marked with hkl values refer to the layered O3 phase and those marked with o and * refer to the P3 and O1 phases, respectively. (a) $Li_{0.98}H_{0.02}[Li_{0.33}Mn_{0.67}]O_{2.01}$, (b) $Li_{0.09}H_{0.15}[Li_{0.14}Mn_{0.34}Co_{0.39}Ni_{0.13}]O_{1.72}$, (c) $Li_{0.01}H_{0.26}[Li_{0.12}Mn_{0.27}Co_{0.46}Ni_{0.15}]O_{1.76}$, (d) $Li_{0.04}H_{0.38}[Li_{0.08}Mn_{0.2}Co_{0.54}Ni_{0.18}]O_{1.86}$, (e) $Li_{0.02}H_{0.41}[Li_{0.04}Mn_{0.13}Co_{0.62}Ni_{0.21}]O_{1.91}$, (f) $Li_{0.08}H_{0.34}[Li_{0.01}Mn_{0.07}Co_{0.69}Ni_{0.23}]O_{1.98}$, and (g) $Li_{0.02}H_{0.36}Ni_{0.02}[Co_{0.77}Ni_{0.23}]O_{1.95}$. 121

Figure 6.6: XRD patterns of the chemically delithiated samples obtained from the (1-z) $Li[Li_{1/3}Mn_{2/3}]O_2 \cdot$ (z) $Li[Co_{1-y}Ni_y]O_2$ ($y = 0.5$ and $0 \leq z \leq 1$) series synthesized at 900 °C. The reflections marked with hkl values refer to the layered O3 phase and those marked with * refer to the O1 phase.
(a) $Li_{0.98}H_{0.02}[Li_{0.33}Mn_{0.67}]O_{2.01}$,
(b) $Li_{0.33}H_{0.03}[Li_{0.27}Mn_{0.53}Co_{0.1}Ni_{0.1}]O_{1.72}$,
(c) $Li_{0.19}H_{0.09}[Li_{0.21}Mn_{0.48}Co_{0.155}Ni_{0.155}]O_{1.70}$,
(d) $Li_{0.04}H_{0.12}[Li_{0.16}Mn_{0.42}Co_{0.21}Ni_{0.21}]O_{1.73}$,
(e) $Li_{0.05}H_{0.18}[Li_{0.12}Mn_{0.36}Co_{0.26}Ni_{0.26}]O_{1.78}$,
(f) $Li_{0.08}H_{0.26}[Li_{0.08}Mn_{0.28}Co_{0.32}Ni_{0.32}]O_{1.86}$,
(g) $Li_{0.02}H_{0.43}[Li_{0.05}Mn_{0.21}Co_{0.37}Ni_{0.37}]O_{1.90}$,
(h) $Li_{0.01}H_{0.46}[Li_{0.02}Mn_{0.14}Co_{0.42}Ni_{0.42}]O_{1.93}$,
(i) $Li_{0.02}H_{0.30}Ni_{0.01}[Mn_{0.07}Co_{0.47}Ni_{0.46}]O_{1.95}$, and
(j) $Li_{0.03}H_{0.22}Ni_{0.06}[Co_{0.53}Ni_{0.47}]O_{2.01}$. 123

Figure 6.7: Rietveld fitting of the X-ray diffraction data of the chemically delithiated (1-z) $Li[Li_{1/3}Mn_{2/3}]O_2 \cdot$ (z) $Li[Co_{1-y}Ni_y]O_2$ ($y = 0.5$ and $z = 0.7$) sample synthesized at 900 °C. $a = 2.8373(2)$ Å, $c = 4.5028(6)$ Å, $V = 31.393(5)$ Å^3, $R_{wp} = 11.98$ %, $R_p = 9.24$ %, and $s = 2.51$. Squares and lines correspond, respectively, to the observed and calculated intensities. The difference between the observed and calculated patterns and the peak positions corresponding to the O1 type phase are also shown. 124

Figure 6.8: XRD patterns of the chemically delithiated samples obtained from the (1-z) $Li[Li_{1/3}Mn_{2/3}]O_2 \cdot$ (z) $Li[Co_{1-y}Ni_y]O_2$ ($y = 0.5$ and $0 \leq z \leq 1$) series synthesized at 750 °C. The reflections marked with hkl values refer to the layered O3 phase and those marked with o and * refer to the P3 and O1 phases, respectively. (a) $Li_{0.82}H_{0.13}[Li_{0.33}Mn_{0.67}]O_{1.99}$,
(b) $H_{0.48}[Li_{0.27}Mn_{0.53}Co_{0.1}Ni_{0.1}]O_{1.72}$,
(c) $H_{0.27}[H_{0.09}Li_{0.14}Mn_{0.47}Co_{0.15}Ni_{0.15}]O_{1.66}$,
(d) $H_{0.23}[H_{0.11}Li_{0.08}Mn_{0.41}Co_{0.2}Ni_{0.2}]O_{1.61}$,
(e) $H_{0.29}[H_{0.15}Li_{0.07}Mn_{0.35}Co_{0.25}Ni_{0.25}]O_{1.70}$,
(f) $H_{0.42}[H_{0.04}Li_{0.08}Mn_{0.27}Co_{0.31}Ni_{0.31}]O_{1.76}$,
(g) $H_{0.55}[Li_{0.07}Mn_{0.21}Co_{0.36}Ni_{0.36}]O_{1.86}$, and
(h) $Li_{0.07}H_{0.45}[Co_{0.5}Ni_{0.5}]O_{1.96}$ 127

Figure 6.9: XRD patterns of the chemically delithiated samples obtained from the (1-z) $Li[Li_{1/3}Mn_{2/3}]O_2 \cdot$ (z) $Li[Co_{1-y}Ni_y]O_2$ ($y = 0.75$ and $0 \leq z \leq 1$) series synthesized at 900 °C. The reflections marked with hkl values refer to the layered O3 phase and those marked with * refer to the O1 phase.
(a) $Li_{0.98}H_{0.02}[Li_{0.33}Mn_{0.67}]O_{2.01}$,
(b) $Li_{0.07}H_{0.18}[Li_{0.10}Mn_{0.36}Co_{0.13}Ni_{0.41}]O_{1.84}$,
(c) $Li_{0.07}H_{0.2}[Li_{0.04}Mn_{0.29}Co_{0.17}Ni_{0.5}]O_{1.92}$,
(d) $Li_{0.12}H_{0.14}[Li_{0.02}Mn_{0.22}Co_{0.19}Ni_{0.57}]O_{1.96}$, and
(e) $Li_{0.72}Ni_{0.1}[Co_{0.28}Ni_{0.72}]O_{1.99}$. 128

Figure 6.10: XRD patterns of the chemically delithiated samples obtained from the $(1\text{-z})\ \mathrm{Li[Li_{1/3}Mn_{2/3}]O_2} \cdot (z)\ \mathrm{Li[Co_{1-y}Ni_y]O_2}$ ($y = 1.0$ and $0 \leq z \leq 1$) series synthesized at 900 °C. The reflections marked with hkl values refer to the layered O3 phase and those marked with * refer to the P3 phase. (a) $\mathrm{Li_{0.98}H_{0.02}[Li_{0.33}Mn_{0.67}]O_{2.01}}$, (b) $\mathrm{Li_{0.02}H_{0.40}[Li_{0.2}Mn_{0.49}Ni_{0.31}]O_{1.82}}$, (c) $\mathrm{Li_{0.12}H_{0.15}[Li_{0.08}Mn_{0.37}Ni_{0.55}]O_{1.90}}$, (d) $\mathrm{Li_{0.47}Ni_{0.04}[Mn_{0.23}Ni_{0.77}]O_{1.97}}$, and (e) $\mathrm{Li_{0.66}Ni_{0.15}[Ni]O_{1.80}}$. 129

Figure 6.11: Proton content vs. cation disorder in the chemically delithiated $(1\text{-z})\ \mathrm{Li[Li_{1/3}Mn_{2/3}]O_2} \cdot (z)\ \mathrm{Li[Co_{1-y}Ni_y]O_2}$ ($0 \leq y \leq 1$ and $0 \leq z \leq 1$) solid solution samples. The structure of each delithiated phase is shown next to their respective icon. The samples enclosed within the circle have predominantly either the P3 or O1 phases. 130

Figure 6.12: XRD patterns of the electrochemically charged (to 4.8 V at 12.5 mA/g) layered $(1\text{-z})\ \mathrm{Li[Li_{1/3}Mn_{2/3}]O_2} \cdot (z)\ \mathrm{Li[Co_{1-y}Ni_y]O_2}$ solid solution cathodes: (a) $y = 0$ and $z = 0.9$ and (b) $y = 0.5$ and $z = 0.7$. 132

CHAPTER 1

Introduction

1.1 ELECTROCHEMICAL POWER SOURCES

The rapid developments of innovative technologies and growing environmental concerns have created enormous interest in the development of more efficient, pollution-free, and safe power sources. The growing concern over global warming and air pollution has triggered the replacement of internal combustion engines by alternative power sources. In this regard, electrochemical power sources are attractive as they provide clean energy and decrease our dependence on fossil fuels. Electrochemical power sources, allow the direct conversion of free energy of a chemical reaction to electrical energy without any loss of efficiency associated with the Carnot limitations. Electrochemical power sources can be classified into three major types: Batteries, Fuel cells, and Super capacitors.

A battery can be defined as an electrochemical storage device that converts the chemical energy of a reaction directly into electrical energy.[1] Fuel cells operate much like a battery except that the reactants are not stored but continuously fed to the cell. Fuel is fed to the anode (negative electrode) and an oxidant is fed to the cathode (positive electrode) during the cell operation, and electrochemical oxidation and reduction reactions take place at the electrodes to produce electric current.[2] In the case of electrochemical supercapacitors, energy is stored by charge separation within the micropores of a large surface area electrode material. They are primarily charge storage devices, which can be charged and discharged at rapid rates.[3]

1.2 PRINCIPLES OF ELECTROCHEMICAL CELLS

The electrochemical cell converts the chemical energy stored in the active materials into electrical energy or vise versa by electrochemical oxidation-reduction reactions, involving the flow of electrons through an external circuit. An electrochemical cell consists of three major components as shown schematically in Figure 1.1. The anode (negative electrode) undergoes oxidation during the electrochemical reaction and gives up electrons to the external circuit. The cathode (positive electrode) undergoes reduction during the electrochemical reaction and accepts electrons from the external circuit. The electrolyte, on the other hand, acts as a medium for the transfer of electronic charge, as ions, between the anode and the cathode. The electrolyte used should be a good ionic conductor and an electronic insulator, whereas the electrodes used are preferred to be both good ionic and electronic conductors.

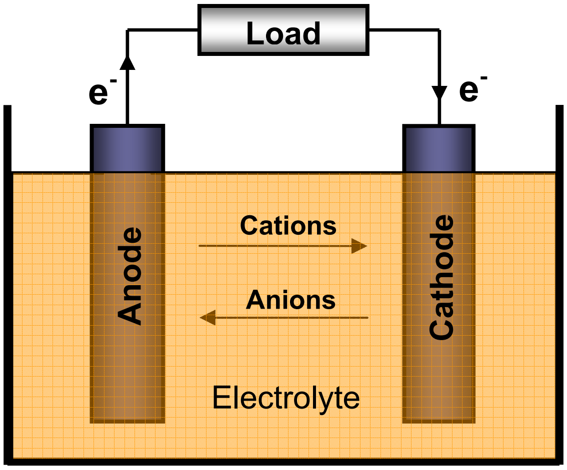

Figure 1.1: Schematic representation of an electrochemical cell.

Electrochemical cells can be broadly classified into two categories according to the reaction mechanisms involved: Electrolytic cell and Galvanic (or Voltaic) cell.[4] In an electrolytic cell, an external voltage drives the electrochemical reactions taking place inside the cell. They include electroplating, electrolytic synthesis, and the charge mode of a secondary battery. In a galvanic cell, the reactions occur spontaneously at the electrodes resulting in a flow of electrons through the external circuit. In essence, they convert chemical energy into electrical energy. Batteries and fuel cells belong to this category. Depending on the desired output voltage and capacity for a specific application, one or more galvanic cells are connected in series or parallel to form the power source.

A battery will deliver a certain cell potential depending on the combination of the electrode materials and the type of chemical reactions involved. To a first approximation, the cell voltage V_{op} of a battery can be given as the difference between the cathode potential and the anode potential.

$$V_{op} = E_c - E_a \qquad [1.1]$$

But, a practical battery may show a lower and varying potential depending on the operating conditions. A part of the energy delivered by the battery is lost as waste heat due to polarization losses in the cell. The battery operation may involve several types of polarizations, which lower the observed or operating potential compared to the ideal cell potential. The polarization losses can be classified into three major types as illustrated in Figure 1.2.

(a) Ohmic polarization (IR drop) is related to the internal impedance of the cell. The ionic resistance of the electrolyte, the electronic resistance of the electrodes/current collectors, and the contact resistance between the electrode and current collector constitute the ohmic polarization of a battery.

(b) Activation polarization (η_a) is related to the kinetics of electrode reactions. It originates from the resistance to charge transfer across the electrode-electrolyte interface and it depends on the ability of the electrode to ionize.

(c) Concentration polarization (η_c) is related to the mass transfer problems that originate from the difference in the concentration of the reactants (and products) between the electrode surface and the bulk.

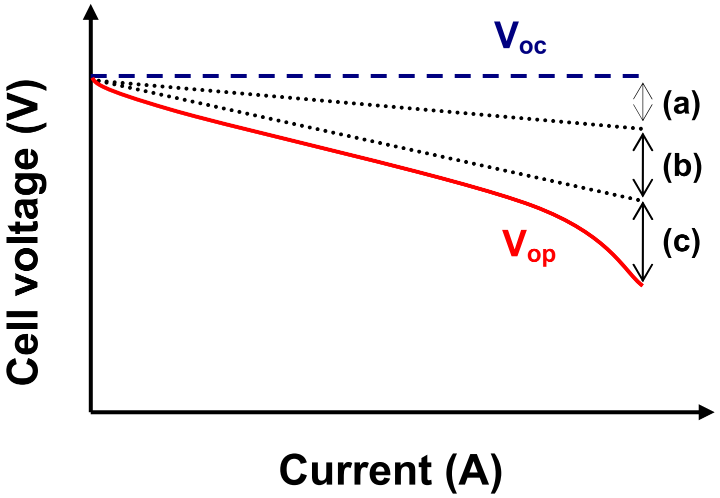

Figure 1.2: Variation of cell voltage with operating current illustrating polarization losses: (a) ohmic polarization, (b) activation polarization, and (c) concentration polarization.

The operating cell voltage V_{op} can then be given by

$$V_{op} = V_{oc} - \eta \qquad [1.2]$$

where V_{oc} is the open-circuit voltage and η is the overvoltage from polarization and is given by

$$\eta = \eta_a + \eta_c + IR \qquad [1.3]$$

If a battery delivers a current of I amperes for t seconds, then the capacity of the battery is given by It coulombs or ampere-seconds as

$$Q = It \qquad [1.4]$$

One gram-equivalent weight of a material will deliver 96487 C or 26.8 Ah, which is the capacity of 1 mol of electrons and is termed as the Faraday constant. It is calculated as

$$1\ F = e * N_A = 96487\ C/mol = 26.8\ Ah \qquad [1.5]$$

where e is the electronic charge (1.602×10^{-19} C) and N_A is the Avogadro's number (6.023×10^{23} atoms/mol).

The specific capacity of the battery Q_{sp} is obtained by dividing the capacity Q of the cell by the mass or the volume of the cell and is given in units of Ah/kg (gravimetric capacity) or Ah/L (volumetric capacity).

The energy density of the battery ε_{sp} is given by the product of the cell capacity Q_{sp} and the average operating voltage V_{op} of the cell and is usually given in terms of Wh/kg (gravimetric energy density) or in Wh/L (volumetric energy density):

$$\varepsilon_{sp} = Q_{sp}V_{op} \qquad [1.6]$$

The power P_{sp} of the cell can be given by the product of the current I_{sp} and the operating voltage V_{op} of the cell and is usually given in terms of W/kg or W/L:

$$P_{sp} = I_{sp}V_{op} \qquad [1.7]$$

The rate at which a battery is charged or discharged is given by the C-rate. A C-rate of τ implies that a nominal capacity Q_n will be delivered in $1/\tau$ hours at a constant discharge current I_d.

The coulometric efficiency q_c of the battery is obtained by dividing the discharge capacity Q_d by the charge capacity Q_c of the cell. A coulometric efficiency $q_c < 1$ implies an unwanted side reaction or electrolyte reaction occurring during the electrochemical charge.

1.3 BATTERIES

A battery is an energy storage device that directly converts the chemical energy stored in the active materials into electrical energy by electrochemical oxidation-reduction reactions. Based on the reversibility of the electrochemical reactions, batteries can be broadly classified into (a) primary or non-rechargeable batteries and (b) secondary or rechargeable batteries. In the primary batteries, the active materials undergo irreversible chemical reaction. On the other hand, they exhibit reversible chemical reactions in secondary batteries. Tables 1.1 and 1.2 list some of the major primary and secondary battery systems that are commercially used.[1,5]

1.4 THE PRIMARY BATTERY SYSTEMS

In 1799, Alessandro Volta invented the first battery which came to be known as the Voltaic pile. It consisted of pairs of zinc and copper plates piled on top of each other, separated by a layer of cloth soaked in brine. This was followed by the invention of various other primary batteries like the Daniel cell (1836), Grove cell (1844), Gravity cell (1860), Leclanche cell (1866), Zinc-carbon cell (1887), Alkaline Zn-MnO_2 cell (1955), and the lithium cell (1970's).[7]

The most commonly available primary cell is the alkaline Zn-MnO_2 dry cell, offering an open circuit voltage of 1.5 V. Recently, the 3 V lithium cells employing a lithium anode and an organic electrolyte coupled to MnO_2 or other transition metal oxide/ sulfide cathodes is becoming increasingly popular due to their higher voltage, higher energy density, and wider operating temperatures (-40^oC to $+60^oC$).[6] Lithium, with an atomic mass of 6.941, is the lightest of all the metals and has a high specific capacity (3860 mAh/g) along with a high negative reduction potential (-3.01 V vs. SHE). It also has a longer shelf life, because the lithium anode reacts with the organic electrolyte, forming a passivating film and thus protecting it from further self discharge.

Table 1.1: The primary battery systems.[1,5]

Battery	Anode	Cathode	Electrolyte/ Cell reaction	Voltage (V)	Capacity (mAh/g)
Leclanche	Zn	MnO_2	NH_4Cl and $ZnCl_2$ (aq) $Zn + 2MnO_2 + 2H_2O \rightarrow Zn(OH)_2 + 2MnOOH$	1.6	220
Alkaline MnO_2	Zn	MnO_2	KOH (aq) $Zn + 2MnO_2 + H_2O \rightarrow ZnO + 2MnOOH$	1.5	220
Zinc-HgO	Zn	HgO	KOH (aq) $Zn + HgO \rightarrow ZnO + Hg$	1.34	190
Zinc-air	Zn	O_2	KOH (aq) $2Zn + O_2 + 2H_2O \rightarrow 2Zn(OH)_2$	1.65	660
Li-SO_2	Li	SO_2	Organic solvent, Li salt $2Li + 2SO_2 \rightarrow Li_2S_2O_4$	3.1	380
Li-MnO_2	Li	MnO_2	Organic solvent, Li salt $Li + MnO_2 \rightarrow LiMnO_2$	3.5	290

1.5 THE SECONDARY BATTERY SYSTEMS

1.5.1 Lead-Acid battery

In 1859, Gaston Plante invented the lead-acid battery by spirally rolling two lead sheets separated by rubber strips and immersing it in sulphuric acid.[7] It is the first battery that could be recharged by passing a reverse current through it. The improved version of the lead-acid battery consists of a lead anode and a lead oxide cathode immersed in sulfuric acid. The low cost coupled with good reversibility makes it a versatile power source for heavy duty applications. Despite its low capacity, it is used in applications where weight is not a big concern. It is widely used in automobiles for starting, lighting, and ignition (SLI) purposes.

Table 1.2: The secondary battery systems.[1,5]

Battery	Anode	Cathode	Electrolyte/Cell reaction	Voltage (V)	Capacity (mAh/g)
Lead-acid	Pb	PbO_2	H_2SO_4 aqueous solution $Pb + PbO_2 + 2H_2SO_4 \leftrightarrow 2PbSO_4 + 2\,H_2O$	2.1	120
Ni-Cd	Cd	NiOOH	KOH aqueous solution $Cd + 2NiOOH + 2H_2O \leftrightarrow 2Ni(OH)_2 + Cd(OH)_2$	1.35	180
Ni-MH	MH	NiOOH	KOH aqueous solution $MH + NiOOH \leftrightarrow M + Ni(OH)_2$	1.35	210
Lithium ion	C + Li	$Li_{0.5}CoO_2$	Organic solvent, Li salt $0.5Li + Li_{0.5}CoO_2 \leftrightarrow LiCoO_2$	3.7	140

1.5.2 Nickel-Cadmium battery

In 1899, Waldmar Jungner invented the nickel-cadmium battery by using nickel oxyhydroxide (NiOOH) cathode, cadmium anode, and an aqueous potassium hydroxide electrolyte. It was the first rechargeable battery to use an alkaline electrolyte.[7] Compared to the lead-acid battery, this has several advantages such as lighter weight, higher energy density, longer life, a constant discharge voltage, high rate capability, and it can be operated at low temperatures. The KOH electrolyte used in this battery is safer than the sulfuric acid used in lead-acid battery. But the cadmium used is more expensive and toxic than lead, resulting in health and disposal problems. It also has an additional intrinsic problem called the memory effect, which results in a diminished capacity following an incomplete charge/discharge cycle. Though it is more expensive than the lead-acid battery, it has found applications in small electronic devices where weight is a major concern. In recent years, it is being increasingly replaced by other advanced battery systems.

1.5.3 Nickel-Metal hydride battery

In the late 1980's, Stanford Ovshinsky invented the nickel-metal hydride battery by replacing the cadmium anode in the nickel-cadmium battery with a metal alloy that reversibly absorbs and releases hydrogen during the charge/discharge process.[7] It is attractive because of its higher energy density and non-toxic nature compared to the Ni-Cd battery. But the rate capability is lower than that of the Ni-Cd battery.

1.5.4 Lithium Ion batteries

Lithium ion batteries were commercialized by Sony Corporation in 1990 and since then they have become increasingly popular for small portable electronic devices such as cellular phones and laptops.[8,9] They involve a reversible intercalation of lithium ions into the anode and cathode materials during the charge/discharge process. Lithium ion batteries are preferred for portable devices compared to other battery systems due to their higher volumetric and gravimetric energy densities (Figure 1.3). In other words, lithium ion batteries are smaller and lighter compared to other battery systems.[10] They are also being intensively pursued for electric-vehicle applications because of the high voltage, high energy density, and wide operating temperatures, arising from the use of non-aqueous electrolytes.

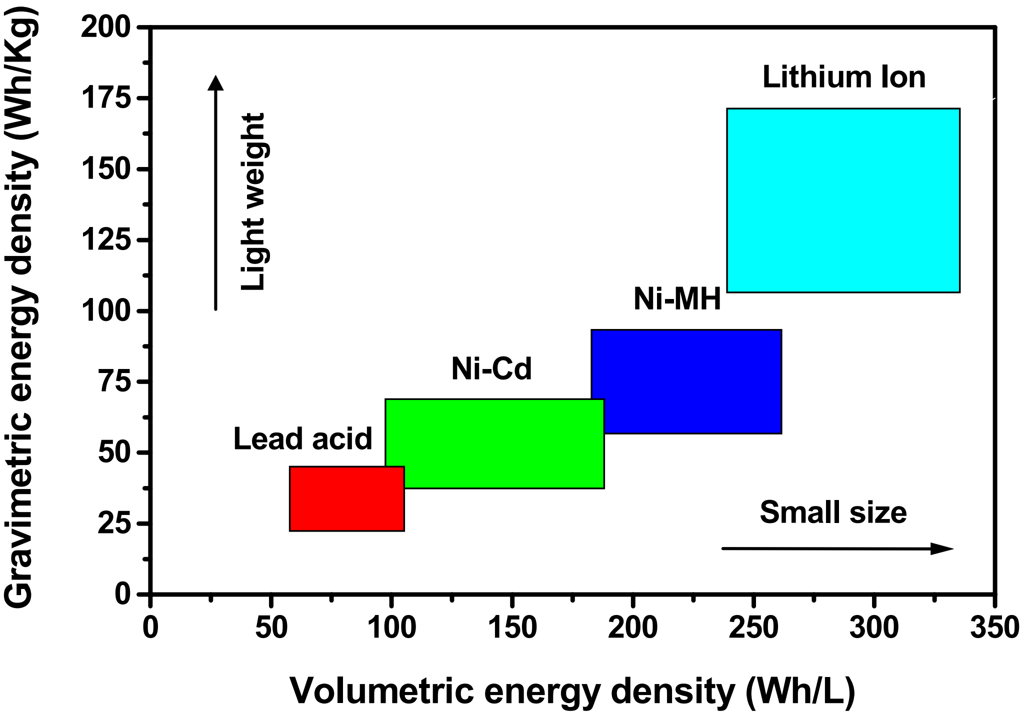

Figure 1.3: Comparison of the gravimetric and volumetric energy densities of popular rechargeable battery systems.[1,10]

1.6 LITHIUM ION BATTERIES

1.6.1 Design considerations

The open circuit voltage V_{oc} of a lithium cell is given by the difference in the lithium chemical potential between the cathode ($\mu_{Li(c)}$) and the anode ($\mu_{Li(a)}$) as,

$$V_{oc} = \mu_{Li(c)} - \mu_{Li(a)} / F \qquad [1.8]$$

where F is the Faraday constant. The schematic energy diagram of a lithium cell at open circuit is shown in Figure 1.4. The cell voltage V_{oc} is determined by the energies involved in both Li^+ ion transfer and electron transfer that take place during discharge. The electron transfer energy is related to the work functions of the cathode (Φ_C) and the anode

(Φ_A). The Li^+ ion transfer energy is determined by the crystal structure and coordination geometry of the site into which the Li^+ ions are inserted. It follows that the difference between the cathode work function and the anode work function should be as large as possible in order to maximize the cell voltage. However, for the electrolyte to be stable, the Fermi energy of the cathode and the anode should lie within the band gap E_g constituted by the highest occupied molecular orbital (HOMO) and lowest unoccupied molecular orbital (LUMO) of the electrolyte. If the Fermi level of the cathode or the anode lies outside the band gap of the electrolyte, then the electrons will be transferred to/from the electrolyte during the charge/discharge process, resulting in electrolyte decomposition.[11]

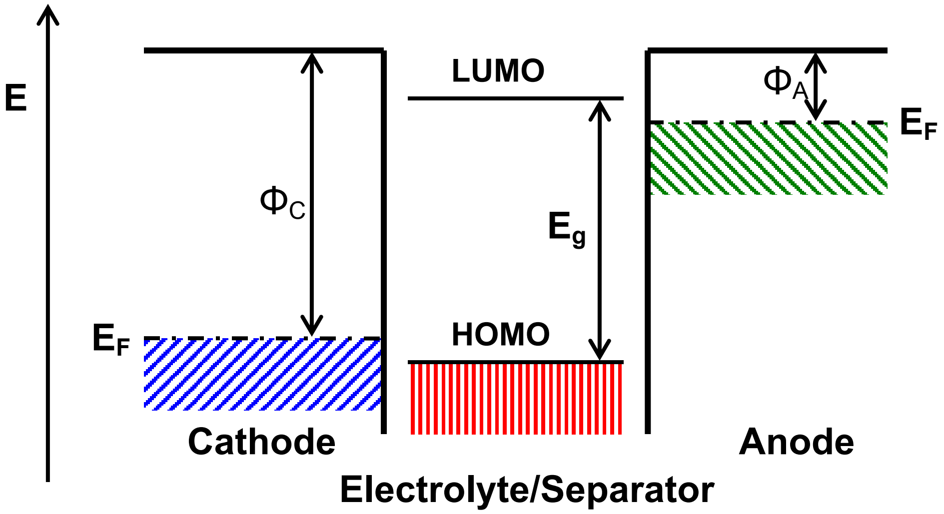

Figure 1.4: Relative energy diagram of a lithium cell at open circuit.[12]

A typical lithium-ion battery is schematically illustrated in Figure 1.5. The anode and the cathode are made of lithium intercalation compounds into/from which the Li^+ ions are reversibly inserted/extracted. The cell in Figure 1.5 uses the layered $LiCoO_2$ and graphite as cathode and anode respectively. The non-aqueous electrolytes used in lithium-ion batteries are based on organic solvents like ethylene carbonate (EC) in which a lithium salt such as $LiClO_4$ is dissolved. Organic electrolytes are preferred over aqueous electrolytes since a wider electrolyte window (E_g) helps to attain higher cell voltages. It is difficult to attain a high cell voltage with an aqueous electrolyte, as the water in it tends to undergo reduction/oxidation at high voltages.

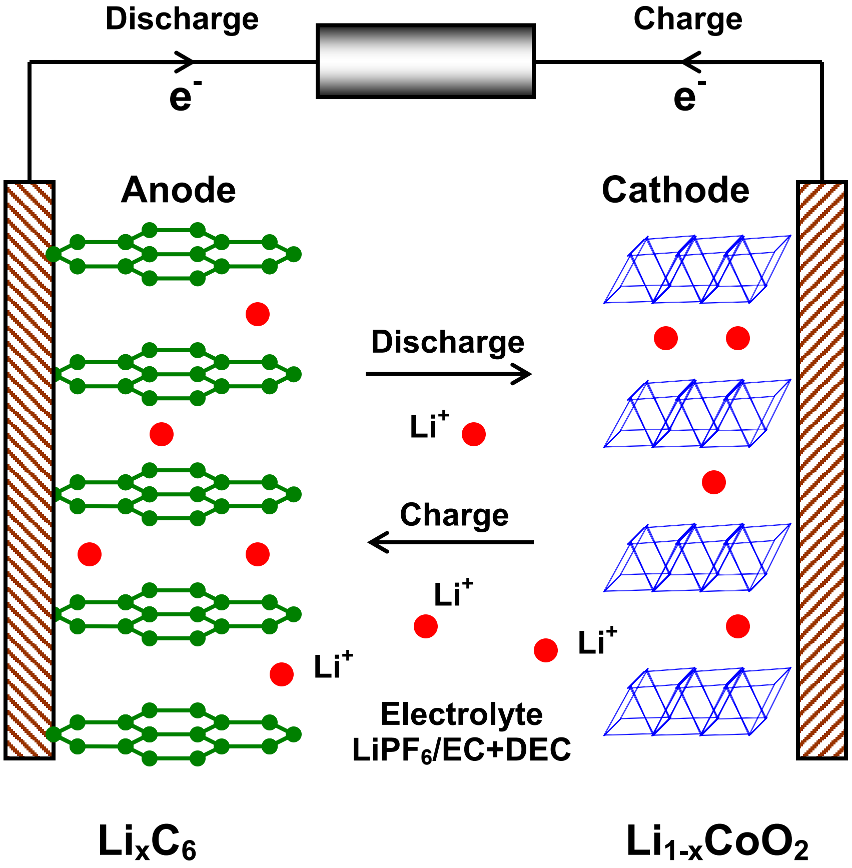

Figure 1.5: Schematic illustration of the charge/discharge process in a rechargeable lithium ion battery.[12]

The lithium insertion compounds that are used as active materials in the cathode or the anode should satisfy several design criteria to be a successful electrode in a lithium ion battery.[12]

(a) To maximize the cell voltage, the cathode work function (Φ_C) should be as large as possible and the anode work function (Φ_A) should be as low as possible, within the limits of the band gap separation (E_g) of the electrolyte. Φ_C increases as the oxidation state of the cathode increases and Φ_A decreases as the oxidation state of the anode decreases. This implies that the M^{n+} transition metal ion in the insertion compound $Li_xM_yO_z$ should have a high oxidation state to be used as a cathode and a low oxidation state to be used as an anode

(b) To maximize the cell capacity, the insertion compound should allow insertion/extraction of a large amount of lithium (x in $Li_xM_yO_z$ should be large). It depends on the number of available sites the lithium ions have access to and also the number of valence states of the transistion metal ion (M^{n+}) that are accessible.

(c) To maximize the life cycles, the change in the structure of the insertion compound during charge and discharge should be minimal.

(d) To minimize polarization losses and to get a high rate of discharge, the insertion compound should have good electronic and Li^+ ion conductivities.

(e) To be commercialized, the insertion compound should be inexpensive, environmentally benign, and lightweight.

The lithium metal anode which is normally used in the primary lithium batteries cause safety problems when used in rechargeable batteries. Under repeated cycling, the lithium metal is prone to dendrite formation that could cause short-circuiting of the battery.[11,13] This led to the development of lithium ion batteries, in which the lithium metal anode is replaced by the carbon anode into which the lithium ions intercalate.[14] The concept of secondary lithium battery was initially demonstrated using a layered metal sulfide TiS_2 as the cathode.[15] During the discharge of this cell, the Li^+ ions from the anode migrate through the electrolyte and intercalate into the van der Walls gap between the sulphide layers and simultaneously the electrons flow through the external circuit from the anode to cathode forming Li_xTiS_2 in the cathode. Though the concept of secondary lithium battery was initially demonstrated using a sulfide cathode, it is difficult to achieve high cell voltage using sulfide cathodes. This is because of the inability to stabilize higher oxidation states of the transition metal ions in sulfides, due to the overlap of the higher valent M^{n+}:3d energy band with the top of the S^{2-}:3p energy band leading to the formation of S_2^{2-} ions. Fortunately, the location of the O^{2-}:2p energy band much below the S^{2-}:3p energy band and the higher Madelung energy of the oxides make the higher valent states accessible in oxides.[16-19] As a result, oxides such as layered $LiCoO_2$, $LiNiO_2$, and spinel $LiMn_2O_4$ are sought as cathodes for lithium ion batteries. The performances of these cathode materials are briefly reviewed below.

1.6.2 Cathode materials

1.6.2.1 Lithium cobalt oxide ($LiCoO_2$) cathode

$LiCoO_2$ has the layered structure in which the O^{2-} ions form a FCC array and the Li^+ and Co^{3+} ions occupy alternate (111) planes of the rock salt structure. A unit cell of $LiCoO_2$ consists of three CoO_2 layers and the Li^+ ions occupy the octahedral interstitial sites between them (Figure 1.6). Therefore, it is designated appropriately as an O3 type layered structure.[20] The edge shared CoO_6 actahedra provides direct Co-Co interaction with the partially filled t_{2g}^{6-x} band that in turn gives good electronic conductivity during discharge.[21] The high electronic conductivity along with the fast lithium ion diffusion between the strongly bonded CoO_2 layers offers a high rate of discharge. The highly oxidized $Co^{3+/4+}$ redox couple provides cell voltage of around 4 V vs. lithium anode.

Unlike some of the 3d transition metal ions, the low spin Co^{3+}/Co^{4+} ions do not migrate to the Li^+ plane during charge-discharge due to their high octahedral site stabilization energy.[22] These distinct features make $LiCoO_2$ an attractive cathode material for lithium ion batteries. In fact, most of the commercial lithium ion batteries are currently made with $LiCoO_2$ cathodes.

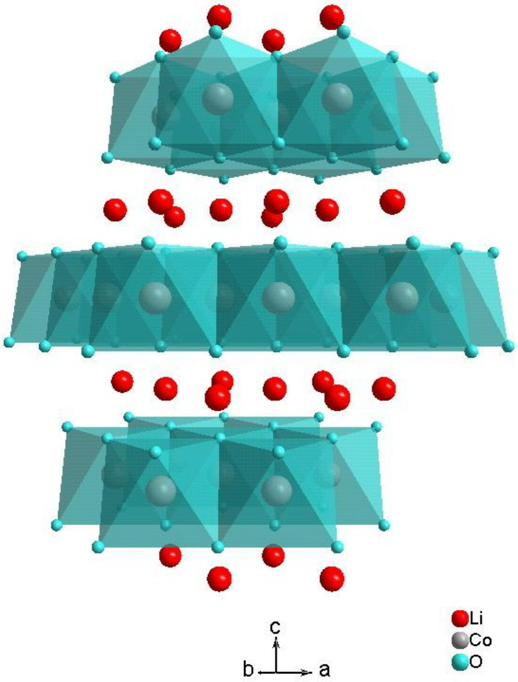

Figure 1.6: Crystal structure of $LiCoO_2$ having the O3 type layered structure. The Li^+ ions occupy the octahedral interstitial sites between the CoO_2 layers.

However, the practical capacity of the $LiCoO_2$ cathode is limited to 140 mAh/g (~50%), which corresponds to a reversible extraction of 0.5 lithium per Co ion. This has been attributed to the chemical and structural instabilities of $LiCoO_2$ at deep charge ($1-x < 0.5$ in $Li_{1-x}CoO_2$).[23,24] This can be explained with the energy band diagram of $Li_{1-x}CoO_2$ (Figure 1.7). $LiCoO_2$ has a low spin $Co^{3+}:3d^6$ configuration, in which the t_{2g} band is completely filled and the e_g band is empty. During charge, lithium is extracted from $LiCoO_2$, which is accompanied by the oxidation of the Co^{3+} ions to Co^{4+} ions by the removal of electrons from the t_{2g} band. Since the t_{2g} band overlaps with the top of the O^{2-}:2p band, deeper lithium extraction ($1-x < 0.5$ in $Li_{1-x}CoO_2$) results in the removal of electrons from the O^{2-}:2p band as well, which results in chemical instability. Also, the CoO_2 layers tend to glide relative to one another under deep charging, resulting in the formation of P3 and O1 type structures from the initial O3 type structure of $LiCoO_2$.[25-29] In addition, cobalt is relatively toxic and expensive. These disadvantages have initiated a search for other lithium intercalation compounds that could possibly substitute for $LiCoO_2$ as a cathode active material in commercial lithium ion batteries.

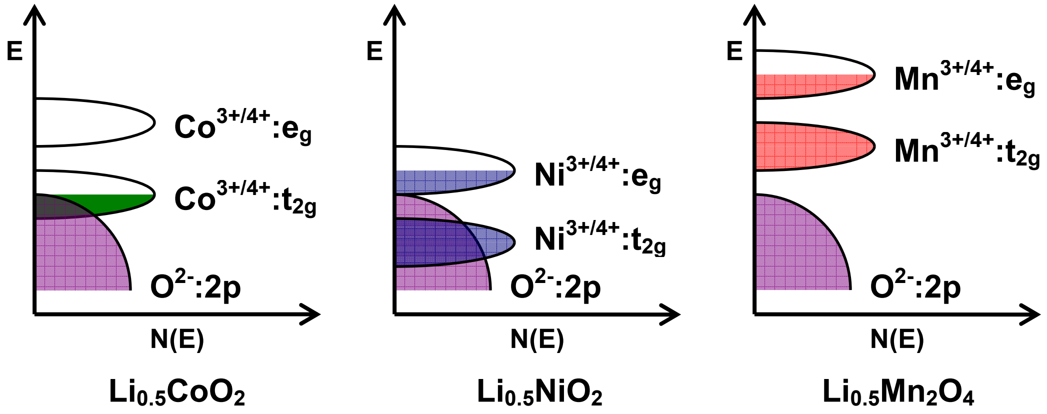

Figure 1.7: Comparison of the qualitative energy diagrams of $Li_{0.5}CoO_2$, $Li_{0.5}NiO_2$, and $Li_{0.5}Mn_2O_4$.[23]

1.6.2.2 Lithium nickel oxide ($LiNiO_2$) cathode

$LiNiO_2$ crystallizes in the same O3 type layered structure as $LiCoO_2$. The $Ni^{3+/4+}$ redox couple provides a cell voltage of around 4 V corresponding to the reversible extraction of lithium ions from the octahedral sites between the NiO_2 layers. Compared to cobalt, nickel is less toxic and less expensive, which makes $LiNiO_2$ appealing for commercial applications. However, the $LiNiO_2$ cathode suffers from a few inherent problems. First, the nickel present in $LiNiO_2$ is in the low spin Ni^{3+}:$t_{2g}^6e_g^1$ configuration that leads to Jahn-Teller distortion (cubic to tetragonal distortion) during the charge/discharge processes.[30] Unlike $LiCoO_2$, the electronic conductivity of $LiNiO_2$ is low because of the completely filled t_{2g} band. Further, it is difficult to synthesize $LiNiO_2$ with all Ni^{3+} ions because some Ni^{3+} ions get reduced to Ni^{2+} during synthesis at high temperatures and that results in a cation mixing of $Ni^{2+/3+}$ ions in the Li^+ plane.[31-33] In addition, the octahedral site stabilization energy of Ni^{3+} is lower than that of Co^{3+} and the Ni^{3+} ions tend to migrate to Li^+ planes on deep charging at elevated temperatures.[34] The presence of $Ni^{3+/4+}$ ions in the Li^+ plane decreases the Li^+ ion conductivity that in turn decreases the rate capability and cyclability of the battery. These disadvantages make $LiNiO_2$ unsuitable for commercial battery applications.

Some of the disadvantages like cation disorder and Jahn-Teller distortion could be overcome by partial substitution of Ni by Co. For example, the compound $LiNi_{0.85}Co_{0.15}O_2$ exhibits a higher reversible capacity (180 mAh/g) and good cyclability compared to $LiCoO_2$.[35-38] Moreover, this compound does not show any significant chemical instability on deep charging unlike $LiCoO_2$. This could be due to the removal of electrons from the $Ni^{3+/4+}$:e_g band, which barely touches the top of the O^{2-}:2p band (Figure 1.7), whereas in $LiCoO_2$, the electrons are removed from the $Co^{3+/4+}$:t_{2g} band, which overlaps with the top of the O^{2-}:2p band. However, $LiNi_{0.85}Co_{0.15}O_2$ suffers from the development of impedance during cycling, particularly at elevated temperatures.

1.6.2.3 Lithium manganese oxide ($LiMn_2O_4$) cathode

Compared to cobalt and nickel, manganese is inexpensive and environmentally benign, which make the $LiMn_2O_4$ cathodes attractive for commercial battery applications.[39,40] $LiMn_2O_4$ crystallizes in the normal spinel structure in which the oxide ions form a cubic closed-packed array and the Li^+ and $Mn^{3+/4+}$ ions occupy the 8a tetrahedral and 16d octahedral sites respectively (Figure 1.8). The edge shared MnO_6

octahedral framework provides direct Mn-Mn interaction that leads to good electrical conductivity (small polaron $Mn^{3+/4+}$). The stable spinel framework provides a good three dimensional Li^+ ion diffusion through the interconnected interstitial sites.

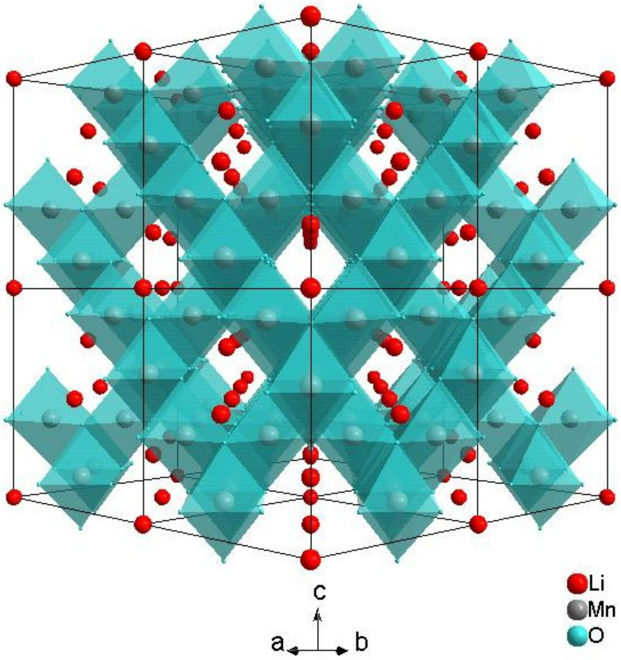

Figure 1.8: Crystal structure of $LiMn_2O_4$ spinel. The Li^+ ions occupy the tetrahedral interstitial sites of the MnO_6 octahedra framework.

An additional lithium ion can also be inserted into the empty 16c sites of the spinel framework, but the electrostatic repulsion between the Li^+ ions in the 16c octahedral site and 8a tetrahedral site causes the displacement of the Li^+ ions from the 8a site to the neighboring empty 16c site to form a rock salt $\{Li_2\}_{16c}[Mn_2]_{16d}O_4$ structure.[41,42] $LiMn_2O_4$ provides a cell voltage of 4 V vs. lithium anode, corresponding to the reversible extraction of Li^+ ion from the 8a tetrahedral site while maintaining the initial cubic structure. The insertion of the additional lithium into the 16c sites occurs at around 3 V by a two phase process involving the cubic $(Li)_{8a}[Mn_2]_{16d}O_4$ spinel and the tetragonal

$\{Li_2\}_{16c}[Mn_2]_{16d}O_4$ rock salt phase. In spite of the fact that both the Li insertion processes involve the same $Mn^{3+/4+}$ redox couple, the difference of 1 V between them is due to the different Li^+ site energies involved.[43] The anisotropic Jahn-Teller distortion associated with the single electron in the e_g orbital of the high spin Mn^{3+}:$3d^4(t_{2g}{}^3e_g{}^1)$ ions is responsible for the tetragonal distortion of $\{Li_2\}_{16c}[Mn_2]_{16d}O_4$ (Figure 1.9). This distortion is accompanied by an increase in the unit-cell volume, which is detrimental to the structural integrity and interparticle contact during repeated charge-discharge cycles. This limits the usage of $LiMn_2O_4$ cathode only to the 4 V region corresponding to the extraction/insertion of Li^+ ion from/into the 8a tetrahedral site.

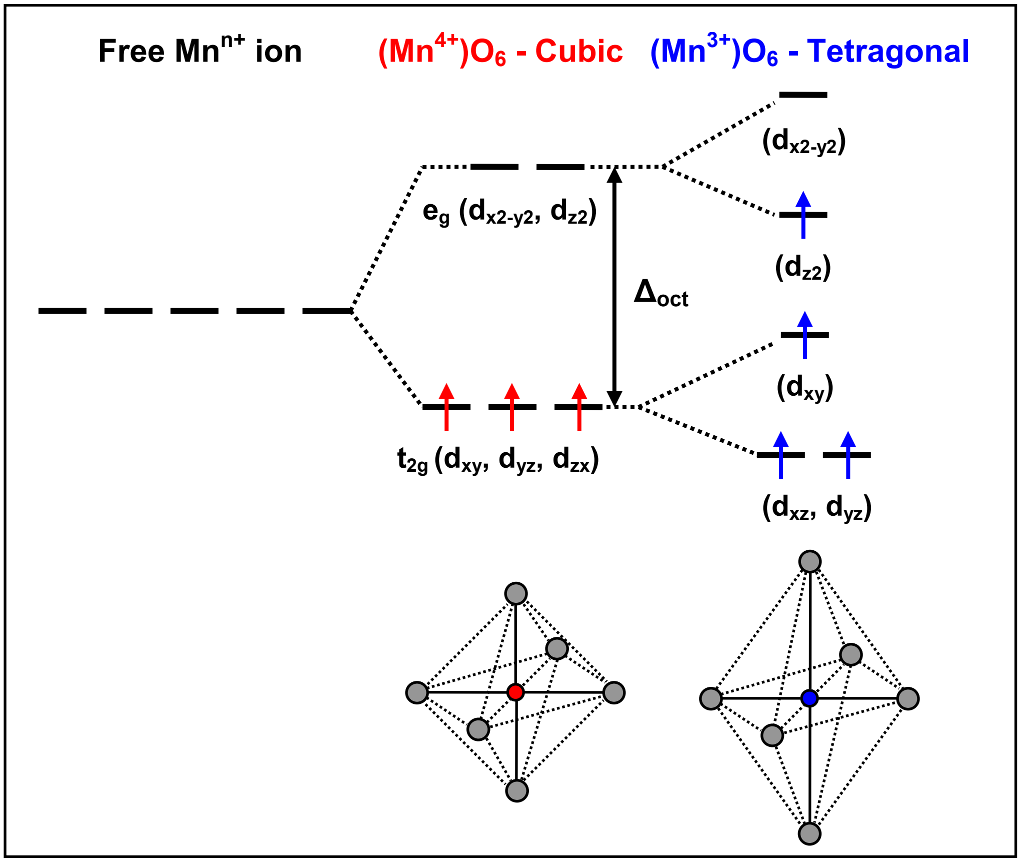

Figure 1.9: Cubic to tetragonal (Jahn-Teller) distortion arising from Mn^{3+}:$3d^4$ due to the single electron present in the e_g orbital.[12]

Nevertheless, $LiMn_2O_4$ exhibits capacity fade even in the 4 V region due to factors like manganese dissolution[44-46] that arises from the disproportionation of Mn^{3+} ions into Mn^{4+} and Mn^{2+}, Jahn-Teller distortion that could occur at the particle surface under high rate of discharge,[47] and the development of microstrain due to the large lattice parameter difference Δa between the two cubic phases formed during cycling.[48-52] However, $LiMn_2O_4$ is quite stable without losing any oxygen from the lattice during the charge-discharge process since the electrons are removed from the $Mn^{3+/4+}$:e_g band, which lies well above the O^{2-}:2p band as seen in Figure 1.7.[23]

The capacity fade of $LiMn_2O_4$ could be overcome by increasing the oxidation state of Mn since Mn^{4+}:$3d^3(t_{2g}^3e_g^0)$ does not undergo Jahn-Teller distortion. The oxidation state can be increased either by increasing the oxygen content or by cationic substitutions. Soft chemistry synthesis methods result in the formation of excess oxygen (or cation deficient) $LiMn_2O_{4+\delta}$ spinel oxides. Lithium ion substitution for manganese to give $LiMn_{2-y}Li_yO_4$ could also increase the oxidation state of manganese. But the above said two strategies lead to a decrease in the 4 V capacity of the spinel compound.[53-56] For example, the end members $Li_2Mn_4O_9$ (excess oxygen) and $Li_4Mn_5O_{12}$ (excess lithium) do not show any 4 V capacity, corresponding to the reversible extraction of lithium from the 8a tetrahedral sites.

1.6.2.4 High voltage spinel ($LiMn_{2-x}M_xO_4$) cathodes

Substitutions of other transition metal ions for manganese have also been pursued to improve the electrochemical performance of the spinel $LiMn_2O_4$ oxide. However, the transition metal ion substituted $LiMn_{2-x}M_xO_4$ (M= Cr, Co, Ni, Fe, and Cu)[57-80] spinel oxides exhibit two plateaus for the reversible extraction of lithium from the 8a tetrahedral sites, one around 4 V corresponding to the $Mn^{3+/4+}$ redox couple and the other around 5 V corresponding to the substituted cationic redox couples like $Ni^{3+/4+}$, $Co^{3+/4+}$ etc. Although cathodes with 5 V capacity are attractive for high power density applications, they are prone to chemical instability due to the overlap of the 3d energy band of the substituted transition metal ions with the O^{2-}:2p band. However, the chemical instability can be minimized if Ni is the substituted element since the $Ni^{2+/4+}$:e_g band barely touches the top of the O^{2-}:2p band as seen in Figure 1.7.[23] Figure 1.10 shows the first discharge curves of various high voltage spinel oxides. Of all the cation substituted $LiMn_{2-x}M_xO_4$ (M= Cr, Co, Ni, Fe, and Cu) spinel oxides, the compound $LiMn_{1.5}Ni_{0.5}O_4$ shows the highest 5 V capacity and the least 4 V capacity.[57-64]

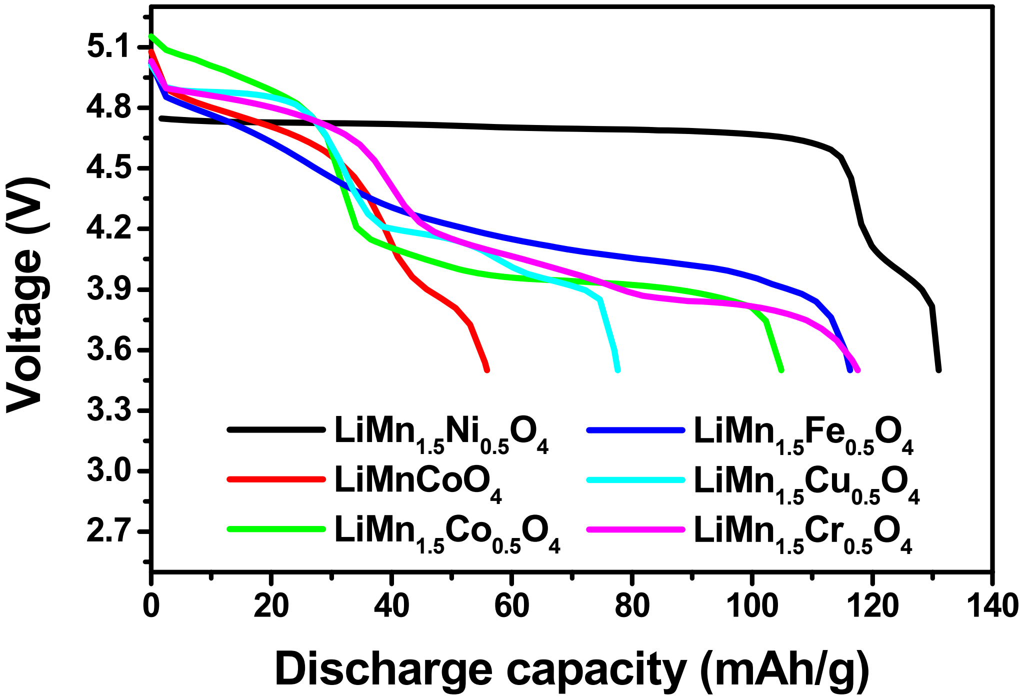

Figure 1.10: The first discharge curves of the 5 V cation substituted $LiMn_{2-x}M_xO_4$ (M= Cr, Co, Ni, Fe, and Cu) spinel oxides.

1.6.2.5 Other cathode materials

Lithium iron sulfates and phosphates including $Fe_2(SO_4)_3$ and $LiFePO_4$ were attractive as cathode materials for lithium batteries, as they are inexpensive, non-toxic and environmentally benign. $Fe_2(SO_4)_3$ has an open NASICON structure where the FeO_6 octahedra share corners with the SO_4 tetrahedra, generating 3-D voids for Li^+ ion insertion.[81] It shows a flat discharge curve around 3.6 V and a capacity of 160 mAh/g. $LiFePO_4$ has an olivine structure where the FeO_6 octahedra share corners with the PO_4 tetrahedra (Figure 1.11).[82-84] With a theoretical capacity of 170 mAh/g and a flat discharge curve around 3.4 V, it was intensively pursued for commercial purposes. However, both $Fe_2(SO_4)_3$ and $LiFePO_4$ suffer from low electronic and lithium ion conductivity.

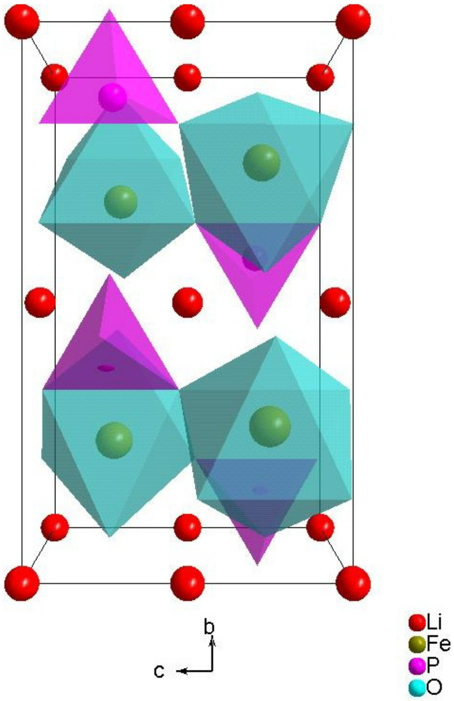

Figure 1.11: Crystal structure of olivine $LiFePO_4$.

Most of the high-voltage (> 4.5 V) cathode materials are based on the spinel structure, which can be expressed as $LiM_{2-x}M'_xO_4$ (M = Mn or V and M' = Cr, Fe, Co, Ni and Cu)[57-80,85,86] excepting $LiCoPO_4$ that has the olivine structure. However, similar to $LiFePO_4$, $LiCoPO_4$ is also plagued with low electronic and lithium ion conductivity and thus exhibits a poor rate capability (Figure 1.12).[87] Other oxides such as vanadium oxides (VO_2, V_6O_{13}, V_2O_5, etc.,),[88,89] chromium oxides (Cr_2O_3, CrO_2, Cr_2O_5, etc.,),[90,91] and molybdenum oxides (MoO_3)[92] were also being explored as cathode materials for lithium batteries. But their overall performance is still inferior compared to the mainstream layered and spinel cathode materials.

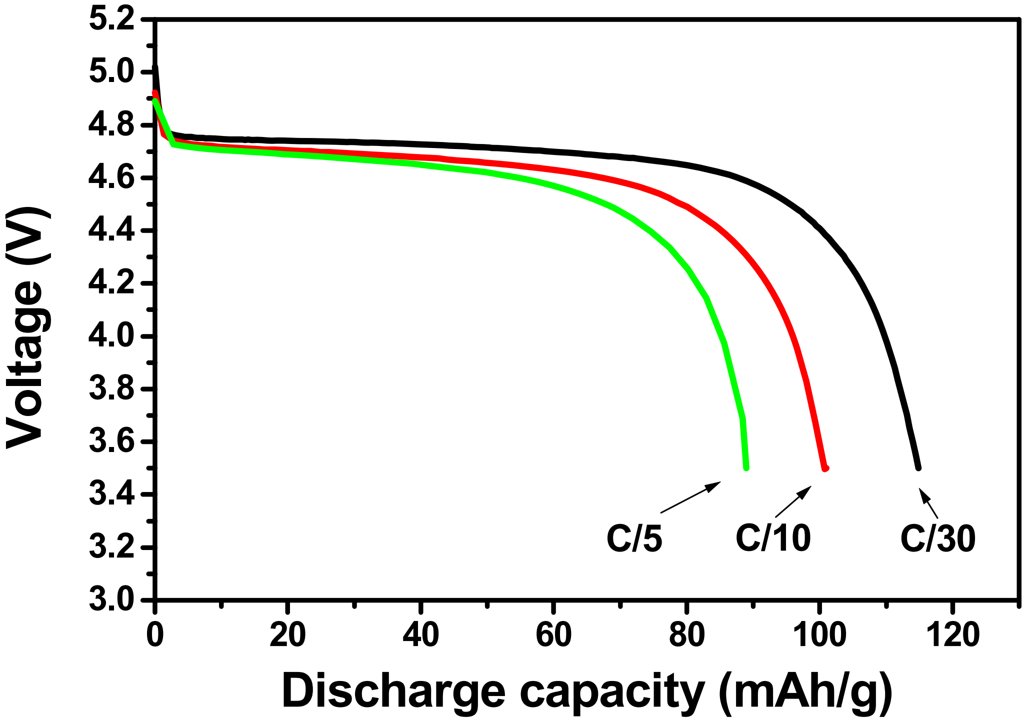

Figure 1.12: Rate capability of the 5 V olivine $LiCoPO_4$.

1.6.3 Anode materials

Metallic lithium, with a specific capacity of 3860 mAh/g, is the ideal anode material for primary lithium batteries. However, it cannot be used in secondary lithium batteries due to a lower cycling efficiency and inherent safety issues such as reactivity and dendrite formation during cycling. In this regard, several lithium insertion materials were pursued as anode materials. Since both the anode and the cathode were insertion materials, the lithium ion battery is also referred to as a “shuttle” battery or a “rocking chair” battery. However, to be a good anode insertion material, it should exhibit a lower discharge voltage vs. Li/Li^+ and it should also be able to store a reasonably large quantity of lithium ions in its structure. At present, graphitic carbon is mostly used as the anode material in most commercial lithium ion batteries as it exhibits a discharge voltage less than 0.5 V vs. Li/Li^+ and a specific capacity around 300 mAh/g. In addition, graphitic carbon is light weight, abundant, safe, and dimensionally stable compared to the other insertion anode materials. At ambient pressure, a maximum of one Li atom per six carbon atoms can be inserted for highly crystalline graphitic carbon ($x \leq 1$ in Li_xC_6).[93] However, it shows a significant irreversible capacity loss in the initial few cycles. This irreversible capacity loss in the initial few cycles is generally attributed to the formation of a protective solid electrolyte interfacial (SEI) layer on the surface of the carbon. Other insertion materials such as $Li_4Ti_5O_{12}$,[94.95] tin oxides,[96] and metal alloys[97,98] were pursued as anode materials for lithium ion batteries, but they could not replace the carbon anode due to, respectively, a higher potential vs. Li/Li^+, significant irreversible loss, and a larger volume change leading to a poor cyclability.

1.6.4 Electrolytes

Since water is not stable at the working voltage of the lithium battery, non-aqueous organic electrolytes with a wider electrochemical stability widow have to be used, albeit with lower ionic conductivities than the aqueous electrolytes. The critical factors in selecting an electrolyte are its compatibility with the electrodes, good solubility for lithium salts, low vapor pressure, and thermal stability. Propylene carbonate (PC) based electrolytes were widely used in lithium primary batteries. However, in the case of lithium ion cells with graphitic carbon anodes, the choice of the electrolyte is restricted primarily to systems based on ethylene carbonate (EC) since those based on other solvents tend to cause exfoliation of the graphite.[99,100] Since EC is a solid at room temperature, it is usually mixed with low viscous solvents like dimethyl carbonate (DMC) or diethyl carbonate (DEC).

The most preferred lithium salt is lithium hexafluorophosphate ($LiPF_6$), although other lithium salts such as lithium perchlorate ($LiClO_4$), lithuim hexafluroarsenate ($LiAsF_6$), and lithium hexafluoroantimonate ($LiSbF_6$) could be also used. In fact, EC based electrolytes with $LiPF_6$ salt are stable over 5 V and are being used in most commercial lithium ion batteries. However, these organic electrolytes are flammable and may undergo decomposition due to the high oxidizing potential of the transition-metal oxide cathodes. To overcome these disadvantages, thin 'solid polymer electrolyte' membranes (SPE) comprising lithium salts dissolved in a suitable polymer matrix (e.g. polypropylene oxide) are being intensively pursued for next generation lithium ion batteries.[101]

1.6.5 Separators

The separator is used in a battery to prevent direct electronic contact between the anode and the cathode, while allowing ionic transfer between them. Owing to a poor ionic conductivity of the organic electrolytes, the separator used in the lithium ion battery should be thinner and mechanically stronger, apart from being chemically and electrochemically stable at the operating voltage of the battery. In addition, the separator used in a lithium ion battery should also act as a safety shutdown device by melting down and ceasing the current flow through the battery, in case of an overcharge, overdischarge, or an electrical short circuit. For these reasons, most commercial lithium ion batteries employ a polyethylene (PE) or a polypropylene (PP) film separator.[102]

1.6.6 Safety devices

In addition to the shutdown membrane, the commercial lithium ion batteries are equipped with other safety devices such as a safety vent, a positive thermal coefficient (PTC) element, and external control circuits. The safety vent is designed to release any unexpected high pressure build-up inside the battery during abnormal conditions by permanently detaching the tab from the positive terminal and thus averting further current flow through the battery.[103] PTC is a temperature controlled device that operates by ceasing the current flow, in the event of a battery temperature increase above a critical value. External control circuits are designed to keep the battery voltage under normal operating conditions without any overcharge or overdischarge arising from a faulty battery charger or devices.

1.7 OBJECTIVES

Lithium ion batteries are becoming the leading power sources for portable electronic devices such as cellular phones and lap tops. They are also a potential candidate to power electric and the hybrid electric vehicles. Most commercial lithium ion batteries currently employ the $LiCoO_2$ cathode. But, Co is toxic and expensive. In this regard, the spinel $LiMn_2O_4$ cathode is being investigated extensively as Mn is inexpensive and environmentally benign, but it suffers from capacity fade arising from manganese dissolution and Jahn-Teller distortion, due to the presence of high Mn^{3+} content. However, the $LiMn_{1.5}Ni_{0.5}O_4$ spinel is appealing as the capacity-fading problem can be minimized since Mn in this compound is in the 4+ oxidation state. $LiMn_{1.5}Ni_{0.5}O_4$ spinel oxide is also attractive for high power applications since it offers a higher cell voltage (~5 V), as the entire capacity is due to the $Ni^{2+/4+}$ redox couple. However, the capacity retention of $LiMn_{1.5}Ni_{0.5}O_4$ has to be still improved to match the performance of the $LiCoO_2$ cathode.

The objective of this study is to improve the 5 V capacity and cyclability of the $LiMn_{1.5}Ni_{0.5}O_4$ spinel system by substitution of various transition and non-transition metal ions for Mn and Ni. Further, in order to identify the origin of the improved electrochemical performance, I focus on the phase transitions occurring during the charge-discharge process to correlate the electrochemical performance of the cation substituted spinel $LiMn_{1.5-y}Ni_{0.5-z}M_{y+z}O_4$ (M = Li, Mg, Fe, Co, and Zn) cathodes to the lattice parameter differences among the cubic phases formed during charge-discharge process.

In addition, to investigate the chemical instability, a quantitative determination of the oxygen and proton contents in the chemically delithiated spinel oxides ($Li_{1-x}Mn_{1.58}Ni_{0.42}O_4$ and $Li_{1-x}Co_2O_4$) has been carried out with Prompt Gamma-ray Activation Analysis (PGAA) and the results are complemented with the redox titrations and thermogravimetric analysis (TGA) data. Encouraged by these findings, I also focus on the possibility of oxygen loss from and proton insertion into the high capacity layered oxide cathodes formed by the solid solutions among $Li[Li_{1/3}Mn_{2/3}]O_2$, $LiCoO_2$, and $LiNiO_2$. Some members of such solid solutions are known to exhibit a high capacity of around 250 mAh/g, which is two times higher than that realized with the currently used $LiCoO_2$ cathode, and an investigation of their chemical and structural stabilities will enhance our understanding of the factors controlling the capacity and energy densities of these complex layered oxide cathodes.

CHAPTER 2

Experimental Procedures

2.1 MATERIALS SYNTHESIS

All the spinel and layered oxide samples investigated in this work were synthesized by a hydroxide precursor method. The procedure involves the precipitation of the hydroxide precursors first from a solution containing required quantities of manganese, nickel, and cobalt acetates and either acetate, nitrate or sulfate of the substituted element by adding KOH, followed by mixing the oven-dried hydroxide precursor with a required amount of $LiOH \cdot H_2O$ and firing at 900 °C in either air or flowing oxygen atmosphere for 12 h with a heating/cooling rate of 1 °C/min. Additional details on materials synthesis are given in the individual chapters.

2.2 CHEMICAL DELITHIATION

Chemical extraction of lithium was carried out by stirring the spinel or layered $Li[M_y]O_z$ oxide powder with an acetonitrile solution of the oxidizer NO_2BF_4 for 2 days under argon atmosphere using a Schlenk line.[24] In general, the reaction is given by,

$$Li[M_y]O_z + x\ NO_2BF_4 \rightarrow Li_{1-x}[M_y]O_z + x\ NO_2 + x\ LiBF_4 \qquad [2.1]$$

The NO_2^+/NO_2 redox couple in the NO_2BF_4 oxidizer shows an oxidizing power of 2.1 V vs. NHE,[104] which corresponds to 5.1 V vs. Li^+/Li, and thus extracts most of the lithium from the spinel and layered oxide cathodes investigated in this work. By controlling the molar ratio of the oxide samples to the NO_2BF_4 oxidizer in the initial reaction mixture, $Li_{1-x}[M_y]O_z$ powders with various lithium contents (1-x) could be obtained. After the completion of the reaction, the products were washed several times with acetonitrile under argon atmosphere to remove $LiBF_4$ and dried under vacuum at ambient temperature. The delithiated samples were then collected inside an argon-filled glove box and characterized instantly to avoid contamination from moisture in air.

2.3 MANGANESE DISSOLUTION

The degree of manganese dissolution was assessed by soaking the oxide samples for 7 days at 55 ^{o}C in an electrolyte consisting of 1 M $LiPF_6$ in 1:1 ethylene carbonate (EC) /diethyl carbonate (DEC) enclosed in a Teflon vessel. The electrolyte was then collected by filtration with a glass filter and diluted with deionized water and nitric acid.[105,106] The amount of manganese in the electrolyte was then determined by atomic absorption spectroscopy (AAS).

2.4 MATERIALS CHARACTERIZATION

The as-synthesized and the delithiated samples were characterized by the following techniques. More specific procedures will be presented in the respective chapters.

2.4.1 X-ray powder diffraction (XRD)

X-ray powder diffraction data were collected with a Philips X-ray diffractometer with Cu Kα radiation to identify the phases in the samples. The X-ray specimen was prepared by spreading the finely ground powder onto a glass slide using a few drops of amyl acetate. Diffraction patterns were recorded at a slow scan rate of 0.02^{o} per 5 seconds between 10 and 80^{o}. The collected data were compared with the JCPDS files for phase identification using the JADE software. The crystal structure of the phases and their lattice parameters were determined by Rietveld refinement of the X-ray diffraction data using the DBWS-9411 program.[107,108]

2.4.2 Atomic absorption spectroscopy (AAS)

A Perkin-Elmer 1100 atomic adsorption spectrometer (AAS) was used to determine the lithium content in the as-synthesized and delithiated oxide samples. The sample solution was prepared by dissolving about 40 mg of the sample in concentrated HCl and then heating around 60 ^{o}C for 30 minutes to completely dissolve the samples, followed by diluting to the required concentration with deionized water. The instrument was calibrated with a standard solution containing a known amount of the element being analyzed. For this work, the lithium standard solution of concentration 2.00 mg/L was prepared by dissolving Li_2CO_3 and the manganese standard solution of concentration 2.00 mg/L was prepared by dissolving MnO_2.

2.4.3 Redox titration

A redox titration was used to determine the average oxidation state of the transistion metal ions and the oxygen content of the samples.[109] About 30 mg of the sample was dissolved in a mixture of 20 ml of 4 N H_2SO_4 and 20 ml of 0.05 N $Na_2C_2O_4$ (sodium oxalate) at around 70 ^{o}C. During this process, all $M^{(2+x)+}$ is reduced to M^{2+} (e.g., Mn^{2+}, Co^{2+}, Ni^{2+}) as per the reaction shown below.

$$x\, C_2O_4^{2-} + 2M^{(2+x)+} \rightarrow 2M^{2+} + 2x\, CO_2 \qquad [2.2]$$

The unreacted $C_2O_4^{2-}$ in the solution was then determined by titrating the warm solution with a 0.05 N $KMnO_4$ solution. During this process, the following reaction occurs:

$$5(C_2O_4)^{2-} + 2Mn^{7+} \rightarrow 2Mn^{2+} + 10CO_2 \qquad [2.3]$$

At the end point, the solution turns from colorless to pink. From the volume of $KMnO_4$ consumed, we can get the value of x (the extent of oxidation above M^{2+}) as shown below:

$$x = [(\text{Normality of } KMnO_4)*(V_1-V_2)*FW]/ \text{Sample weight (mg)} \qquad [2.4]$$

where

V_1 = volume of $KMnO_4$ solution (ml) consumed by 20 ml of 0.05 N $Na_2C_2O_4$.

V_2 = volume of $KMnO_4$ solution (ml) consumed in the titration with the sample and 20 ml of 0.05 N $Na_2C_2O_4$.

FW = formula weight of the sample (g/mol).

From the value of x, the average oxidation state of the transistion metal ions and hence the oxygen content of the sample were determined using the charge neutrality principle.

2.4.4 Thermogravimetric analysis (TGA)

A Perkin-Elmer series 7 thermogravimetric analyzer (TGA) was used to study the change in the mass of the samples with increasing temperature.

2.4.5 Scanning electron microscopy (SEM)

A JEOL JSM-5610 scanning electron microscope (SEM) coupled with an energy dispersive spectrometer (EDS) was used to study the morphology and the elemental distribution of the powder samples.

2.4.6 Prompt gamma-ray activation analysis (PGAA)

Since there is a possibility of ion exchange of Li^+ ions by H^+ ions that could be produced by an oxidation of acetonitrile by the powerful oxidizer NO_2BF_4 during chemical delithiation, direct quantitative measurements of hydrogen contents in the chemically delithiated samples were carried out with prompt gamma-ray activation analysis (PGAA) by irradiating the samples for 2 h at a reactor power of 950 kW.[110] The PGAA technique is based on the detection of gamma rays emitted by a target material while it is being irradiated with thermal neutrons. It is a nondestructive technique employed for measuring trace concentrations of short lived, light elements such as hydrogen and boron, which are difficult to be determined with other traditional techniques. During sample irradiation, the elemental nuclei undergo neutron capture and emit prompt gamma-rays upon de-excitation, which are then measured using a high purity germanium detector.[111] Hydrogen emits a single prompt gamma-ray peak at 2223.25 keV on de-excitation and it is straightforward to detect it with PGAA as shown by the following reaction.

$$ {}_{1}^{1}H + {}_{0}^{1}n \rightarrow {}_{1}^{2}H^{*} \rightarrow {}_{1}^{2}H + {}_{0}^{0}\gamma \qquad [2.5] $$

2.5 ELECTROCHEMICAL CHARACTERIZATION

Electrochemical performances of the layered and spinel oxide samples were evaluated with CR2032 coin cells. The cathodes were prepared by mixing 75 wt % active material with 20 wt % conductive carbon and 5 wt % polytetrafluoroethylene (PTFE) binder, rolling the mixture into thin sheets, and cutting into circular electrodes of 0.64 cm^2 area. The electrodes typically had an active material content of ~ 7 mg. The coin cells were fabricated with the cathodes, metallic lithium anode, 1 M $LiPF_6$ in 1:1 diethyl carbonate/ethylene carbonate electrolyte, and Celgard polypropylene separator. Cycle performance testing of the thus assembled coin cells was evaluated using an Arbin battery tester at various C-rates and cut-off voltages.

CHAPTER 3

Influence of Lattice Parameter Differences on the Electrochemical Performance of the 5 V Spinel $LiMn_{1.5-y}Ni_{0.5-z}M_{y+z}O_4$ (M = Li, Mg, Fe, Co, and Zn) Cathodes

3.1 INTRODUCTION

Most commercial lithium ion cells are presently made with the layered $LiCoO_2$ cathode, but only 50% of its theoretical capacity could be utilized in practical cells. Also, Co is expensive and toxic. These drawbacks have created enormous interest in alternative cathodes like spinel $LiMn_2O_4$ as Mn is inexpensive and environmentally benign. However, $LiMn_2O_4$ suffers from severe capacity fade at elevated temperatures, and several mechanisms such as Jahn-Teller distortion,[47] manganese dissolution into the electrolyte,[46] formation of two cubic phases,[48] and development of microstrain due to the large lattice parameter difference Δa between the two cubic phases formed during cycling[49-52] have been suggested to be the source of capacity fade. Minimization of the Δa by multiple cationic substitutions has been found to improve the cyclability, rate capability, and storage characteristics.[50-52]

Recently, several groups[57-64] have investigated the spinel $LiMn_{1.5}Ni_{0.5}O_4$ cathodes, which exhibits high discharge capacity ~ 130 mAh/g (theoretical capacity: 147 mAh/g) at around 4.7 V involving the $Ni^{2+/3+}$ and $Ni^{3+/4+}$ redox couples. The higher voltage is particularly attractive to enhance both the energy and power densities. Additionally, the substitution of only ~ 25% of the Mn by Ni still keeps the cost and toxicity much lower compared to those with the currently used $LiCoO_2$ cathodes. More recently, some studies have shown an improvement in the capacity retention of $LiMn_{1.5}Ni_{0.5}O_4$ by cation doping. For example, substitutions of other cations for Mn and Ni in $LiMn_{1.5-y}Ni_{0.5-z}M_{y+z}O_4$ (M =

Mg, Cr, and Co) have been found to improve the cyclability.[57-60] However, a basic understanding of the reasons for the improvement in capacity retention is not clear in the literature.

In this chapter, a systematic investigation of a number of cation substituted 5 V spinel $LiMn_{1.5-y}Ni_{0.5-z}M_{y+z}O_4$ (M = Li, Mg, Fe, Co, and Zn) cathodes is performed to correlate its electrochemical performance to the lattice parameter differences among the cubic phases formed during the charge-discharge process. In addition, the influence of manganese ion dissolution on the electrochemical performance of the cation substituted 5 V spinel oxides is investigated.

3.2 EXPERIMENTAL

The $LiMn_{1.5-y}Ni_{0.5-z}M_{y+z}O_4$ (M = Li, Mg, Fe, Co, and Zn) samples were synthesized by a hydroxide precursor method, as described in chapter 2 and fired at 900 ^{o}C in a flowing oxygen atmosphere for 12 h with a heating/cooling rate of $1^{o}C$/min.

The cathodes for evaluating the electrochemical performances were prepared as described in chapter 2, and the electrochemical performance evaluations were carried out with CR2032 coin cells at a current density of 0.2 mA/cm^2 between 5 and 3.5 V. Chemical extraction of lithium was carried out by stirring the $LiMn_{1.5-y}Ni_{0.5-z}M_{y+z}O_4$ powder with an acetonitrile solution of the oxidizer NO_2BF_4, as described in chapter 2. The products obtained were used for monitoring the lattice parameter variation with lithium content. The lithium contents were determined by atomic absorption spectroscopy and the lattice parameters were calculated with Rietveld analysis of the X-ray diffraction data.[107] The degree of manganese dissolution was assessed by soaking the $LiMn_{1.5-y}Ni_{0.5-z}M_{y+z}O_4$ samples for 7 days at 55 ^{o}C in an electrolyte consisting of 1 M $LiPF_6$ in 1:1 ethylene carbonate/diethyl carbonate and determining the amount of manganese in the electrolyte with atomic absorption spectroscopy.

3.3 RESULTS AND DISCUSSION

3.3.1 Electrochemical performance of the cation substituted 5 V spinel cathodes

Figure 3.1a shows the X-ray diffraction (XRD) pattern of $LiMn_{1.5}Ni_{0.5}O_4$ synthesized by the hydroxide precursor method. In addition to the spinel reflections, the pattern shows a few weak reflections corresponding to the impurity phase $Li_xNi_{1-x}O$ having the rock salt structure, which is in agreement with the previous reports involving solid state or sol-gel synthesis.[61] The formation of the $Li_xNi_{1-x}O$ impurity phase results in a decrease in the Ni content of the spinel phase as shown by the generalized reaction:

$$LiMn_{1.5}Ni_{0.5}O_4 \leftrightarrow \alpha\, Li_xNi_{1-x}O + \beta\, LiMn_{1.5+y}Ni_{0.5-y}O_4 + \gamma\, O_2 \qquad [3.1]$$

in which α, β and γ define the relative amounts of the $Li_xNi_{1-x}O$, $LiMn_{1.5+y}Ni_{0.5-y}O_4$ and O_2 phases, respectively. From XPS studies, nickel has been found to be present as Ni^{2+} in $LiMn_{1.5}Ni_{0.5}O_4$.[76] This would suggest the absence of Mn^{3+} and one would expect the entire capacity to occur in the 5 V region due to the $Ni^{2+/4+}$ redox couple. However, the formation of a small amount of the impurity phase $Li_xNi_{1-x}O$, leads to a decrease in the nickel content in the spinel phase and a consequent introduction of some Mn^{3+}.[61] The presence of Mn^{3+} in $LiMn_{1.5}Ni_{0.5}O_4$ causes the development of the 4 V plateau and a decrease in the 5 V capacity as shown in Figure 3.2. Attempts to eliminate the impurity phase by increasing the firing duration or changing the firing atmosphere were unsuccessful. A firing temperature of above 750 °C invariably resulted in the formation of the impurity phase as has been found before.[61] This observation suggests that the solubility limit of Ni in the $LiMn_{2-y}Ni_yO_4$ spinel phase could be $y < 0.5$.

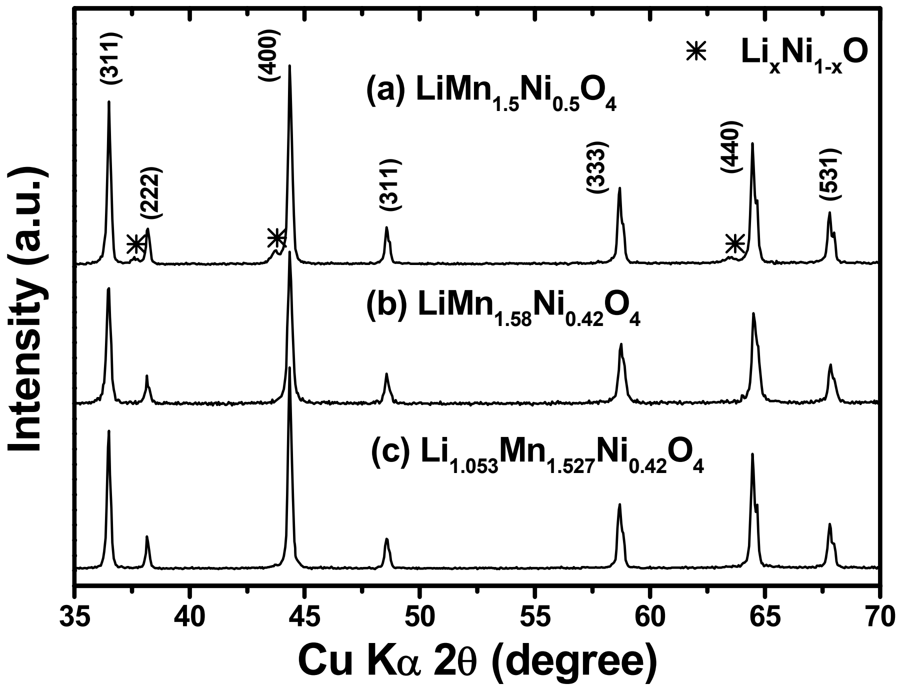

Figure 3.1: X-ray diffraction patterns of (a) $LiMn_{1.5}Ni_{0.5}O_4$, (b) $LiMn_{1.58}Ni_{0.42}O_4$ and (c) $Li_{1.053}Mn_{1.527}Ni_{0.42}O_2$ synthesized by the hydroxide precursor method. The reflections marked with (hkl) values refer to spinel and those marked with * refer to the impurity phase $Li_xNi_{1-x}O$.

By a systematic analysis, we found that the $Li_xNi_{1-x}O$ impurity phase could be suppressed for $y \leq 0.42$ as seen in Figure 3.1b, for the sample $LiMn_{1.58}Ni_{0.42}O_4$. Based on this finding, we kept the Ni content y at or below 0.42 in all our succeeding compositions. However, while we suppressed the formation of $Li_xNi_{1-x}O$ impurity phase in $LiMn_{1.58}Ni_{0.42}O_4$, the reduction of Ni content results in a consequent introduction of some Mn^{3+} ion in the compound and thus it exhibits a small 4 V plateau (Figure 3.2), similar to the parent $LiMn_{1.5}Ni_{0.5}O_4$ cathode. One way to overcome this is to substitute a small amount of Li for Mn in $LiMn_{1.58}Ni_{0.42}O_4$, forming the single phase

$Li_{1.053}Mn_{1.527}Ni_{0.42}O_2$, which theoretically does not have any Mn^{3+} ion content in its composition. As expected, the compound $Li_{1.053}Mn_{1.527}Ni_{0.42}O_2$ shows a much reduced 4 V plateau and a relatively higher 5 V plateau than the $LiMn_{1.5}Ni_{0.5}O_4$ and $LiMn_{1.58}Ni_{0.42}O_4$ cathode.

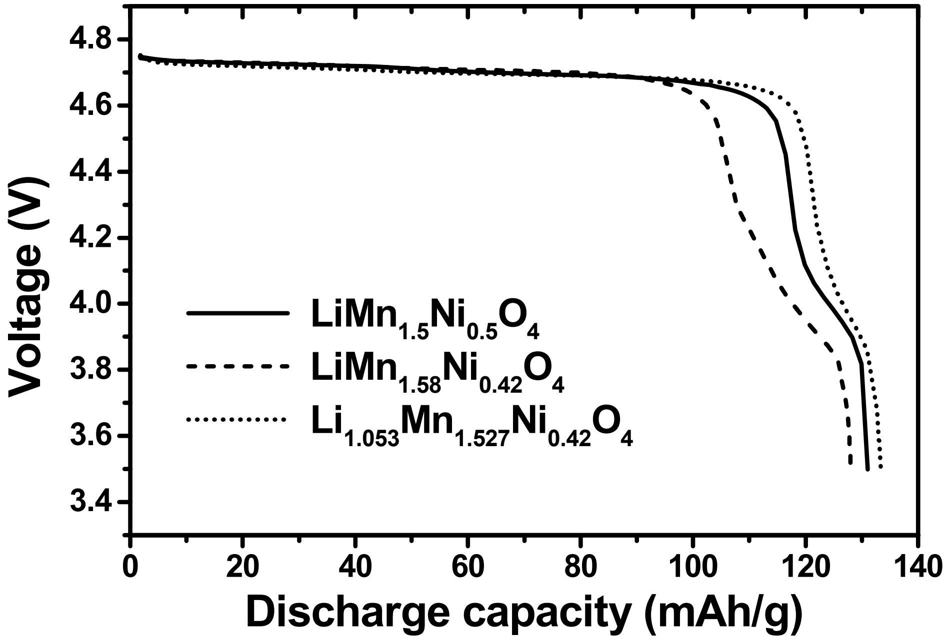

Figure 3.2: First discharge profiles of $LiMn_{1.5}Ni_{0.5}O_4$, $LiMn_{1.58}Ni_{0.42}O_4$ and $Li_{1.053}Mn_{1.527}Ni_{0.42}O_2$, recorded at a current density of 0.2 mA/cm^2 between 5 and 3.5 V.

Figure 3.3 shows the electrochemical cycling performance of the cathodes. Although the impurity phase formation is suppressed in $LiMn_{1.58}Ni_{0.42}O_4$ and $Li_{1.053}Mn_{1.527}Ni_{0.42}O_2$ cathodes, the cycling performance does not improve much compared to the parent $LiMn_{1.5}Ni_{0.5}O_4$ cathode. Therefore, to improve the cycling performance of the 5 V spinel system, we tried substituting small amount of various transition and non-transition metal ions such as Co^{3+}, Fe^{3+}, Mg^{2+}, and Zn^{2+} for Mn and Ni in the composition.

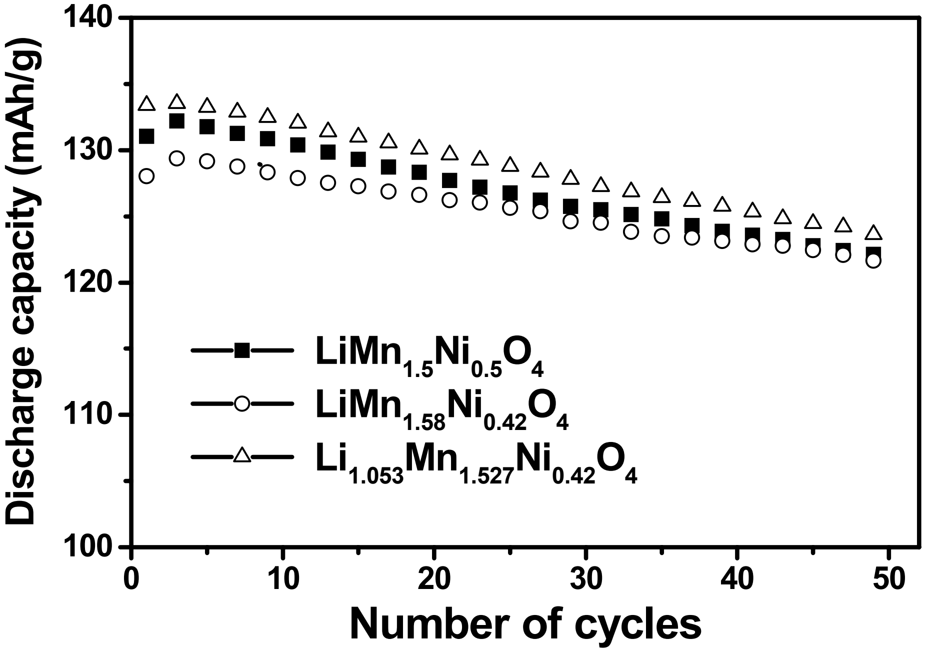

Figure 3.3: Comparison of the cycling performances of the $LiMn_{1.58}Ni_{0.42}O_4$ and $Li_{1.053}Mn_{1.527}Ni_{0.42}O_2$ cathodes with that of $LiMn_{1.5}Ni_{0.5}O_4$. The data were collected at a current density of 0.2 mA/cm^2 between 5.0 and 3.5 V.

Figure 3.4 compares the cycling performances of the $LiMn_{1.5-y}Ni_{0.5-z}M_{y+z}O_4$ (M = Li, Fe, Co, and Zn) samples with that of $LiMn_{1.5}Ni_{0.5}O_4$. The Ni content (0.5-z) in the $LiMn_{1.5-y}Ni_{0.5-z}M_{y+z}O_4$ samples is maintained at 0.42 to eliminate the NiO impurity. Moreover, the $LiMn_{1.5-y}Ni_{0.5-z}M_{y+z}O_4$ compositions were designed in such a way to maintain charge neutrality without introducing Mn^{3+} ions. All the cation substituted samples show better capacity retention than the unsubstituted $LiMn_{1.5}Ni_{0.5}O_4$ although some of them exhibit lower capacities, as has been found before by other groups.[57-60] For example, $LiMn_{1.42}Ni_{0.42}Co_{0.16}O_4$ and $LiMn_{1.5}Ni_{0.42}Zn_{0.08}O_4$ exhibit capacity retentions of > 97 % in 50 cycles compared to 92 % for $LiMn_{1.5}Ni_{0.5}O_4$.

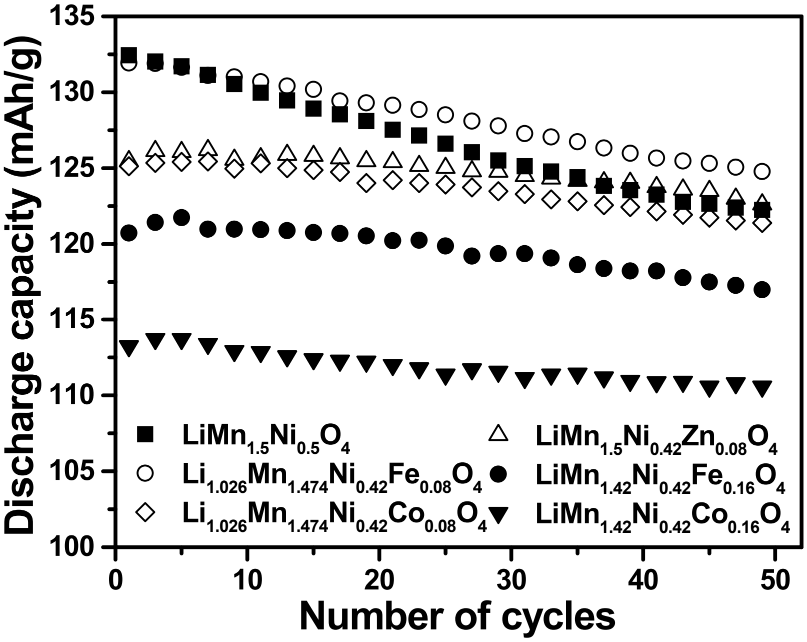

Figure 3.4: Comparison of the cycling performances of the cation substituted spinel $LiMn_{1.5-y}Ni_{0.5-z}M_{y+z}O_4$ (M = Li, Fe, Co, and Zn) cathodes with that of $LiMn_{1.5}Ni_{0.5}O_4$. The data were collected at a current density of 0.2 mA/cm^2 between 5.0 and 3.5 V at room temperature.

Rate capabilities of the $LiMn_{1.5-y}Ni_{0.5-z}M_{y+z}O_4$ cathodes were investigated by charging at the same rate of C/5 and discharging at C/10, C/5, C/2, 1C, 2C, and 4C between 5.0 and 3.5 V. The discharge profiles collected at various rates of $LiMn_{1.5}Ni_{0.5}O_4$ and $LiMn_{1.42}Ni_{0.42}Co_{0.16}O_4$ in Figure 3.5, for example, reveal that the cation substituted $LiMn_{1.42}Ni_{0.42}Co_{0.16}O_4$ exhibits better rate capability (retaining > 92 % of the capacity on going from C/10 to 4C rate) than $LiMn_{1.5}Ni_{0.5}O_4$ (82 %). The high rate capability is particularly attractive for electric vehicle applications.

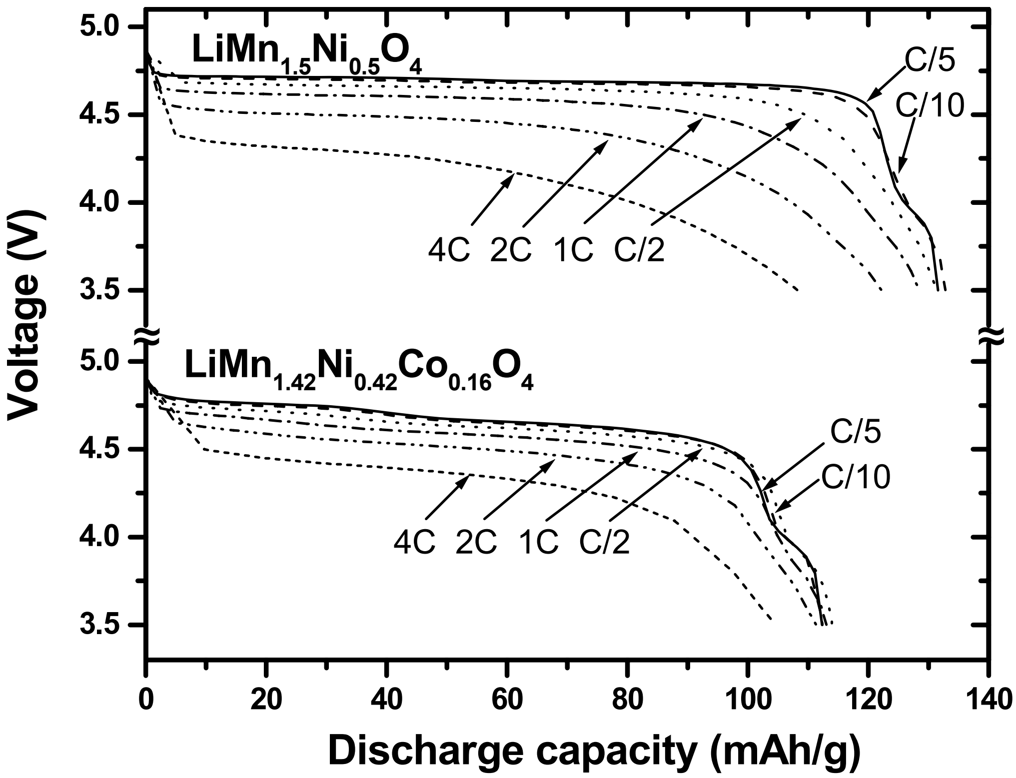

Figure 3.5: Comparison of the discharge profiles of $LiMn_{1.5}Ni_{0.5}O_4$ and $LiMn_{1.42}Ni_{0.42}Co_{0.16}O_4$ at various rates, illustrating the rate capability.

3.3.2 Phase transitions occurring in the 5 V $LiMn_{1.5-y}Ni_{0.5-z}M_{y+z}O_4$ cathodes during the charge-discharge process

In order to identify the origin of the improved electrochemical performance of the cation substituted 5 V $LiMn_{1.5-y}Ni_{0.5-z}M_{y+z}O_4$ cathodes, we focused on the phase transitions occurring during the charge-discharge process. The 4 V $LiMn_2O_4$ spinel was known to exhibit the formation of two cubic phases during the charge-discharge process (Figure 3.6 and 3.7).[48-52] In comparison, the 5 V spinel $LiMn_{1.5}Ni_{0.5}O_4$ was found to exhibit three cubic phases during the charge-discharge process.[62]

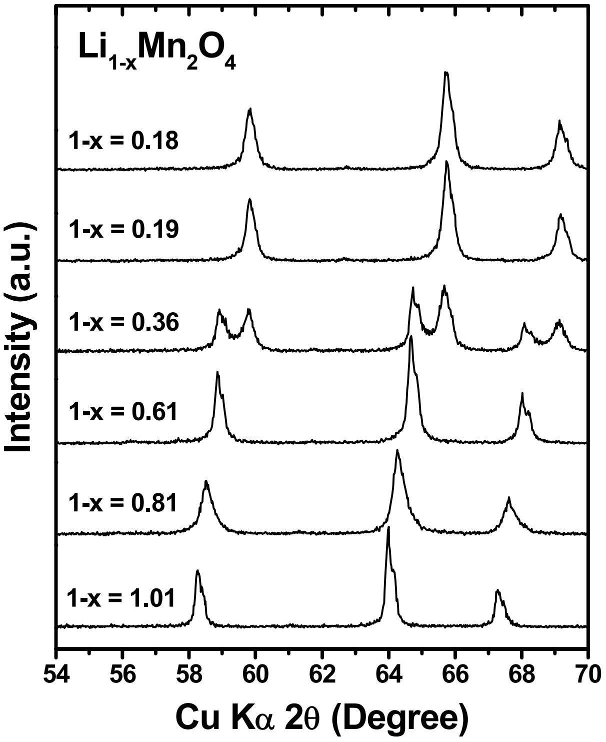

Figure 3.6: X-ray diffraction patterns of the 4 V spinel $Li_{1-x}Mn_2O_4$ samples that were obtained by chemically extracting lithium with NO_2BF_4.

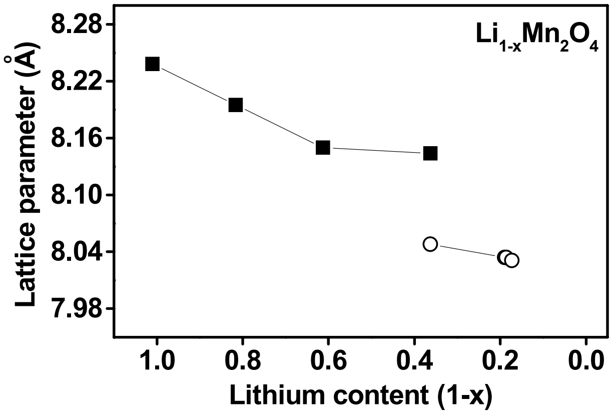

Figure 3.7: Variations of the lattice parameters with lithium content (1-x) in $Li_{1-x}Mn_2O_4$: first cubic phase (■) and second cubic phase (○).

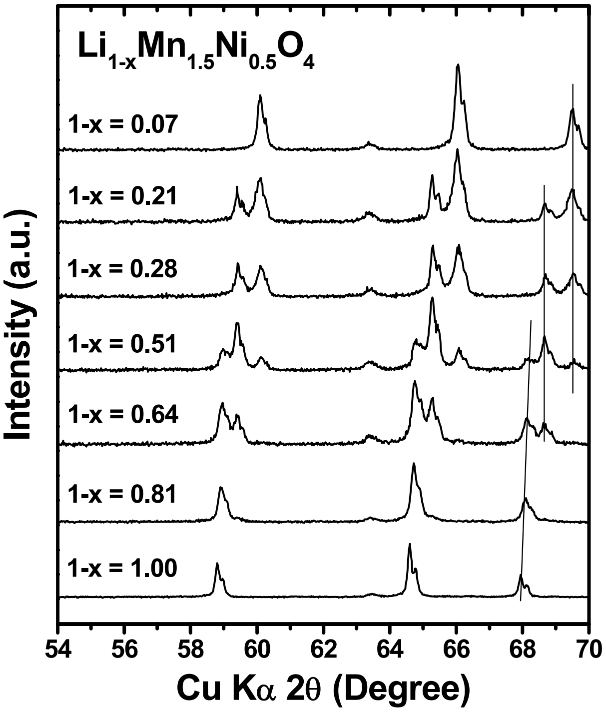

Figure 3.8: X-ray diffraction patterns of the 5 V spinel $Li_{1-x}Mn_{1.5}Ni_{0.5}O_4$ samples that were obtained by chemically extracting lithium with NO_2BF_4.

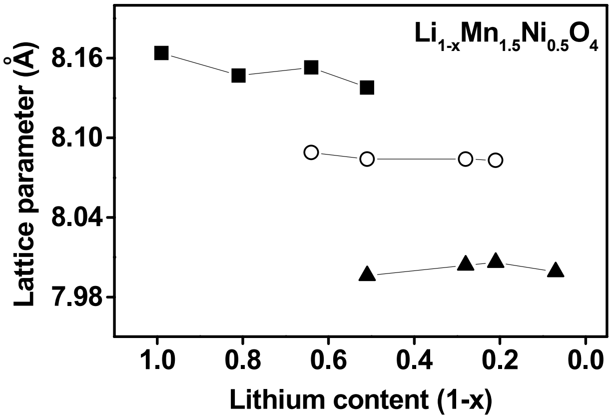

Figure 3.9: Variations of the lattice parameters with lithium content (1-x) in $Li_{1-x}Mn_{1.5}Ni_{0.5}O_4$: first cubic phase (■); second cubic phase (○); and third cubic phase (▲).

Figure 3.8 shows the evolution of the XRD patterns of the $Li_{1-x}Mn_{1.5}Ni_{0.5}O_4$ samples that were obtained by chemically extracting lithium with NO_2BF_4. Using Rietveld analysis, the lattice parameter values of these three cubic phases can be calculated individually (Figure 3.9). The formation of three cubic phases in the 5 V spinel $LiMn_{1.5}Ni_{0.5}O_4$ cathode was further confirmed by electrochemical extraction of lithium from the cathode using an CR2032 coin cell and collecting the XRD patterns of the cathode at different depths of charge (Figure 3.10). Although we are able to observe the formation of three cubic phases by electrochemical delithiation, chemical delithiation using the NO_2BF_4 oxidizer yields bulk samples free from carbon and binder making any further structural and chemical analysis of the delithiated samples possible. Figures 3.11 to 3.26, show the evolution of the XRD patterns and the variations in the lattice parameter values of the three cubic phases that were formed on chemically extracting lithium from various cation substituted 5 V $LiMn_{1.5-y}Ni_{0.5-z}M_{y+z}O_4$ cathodes.

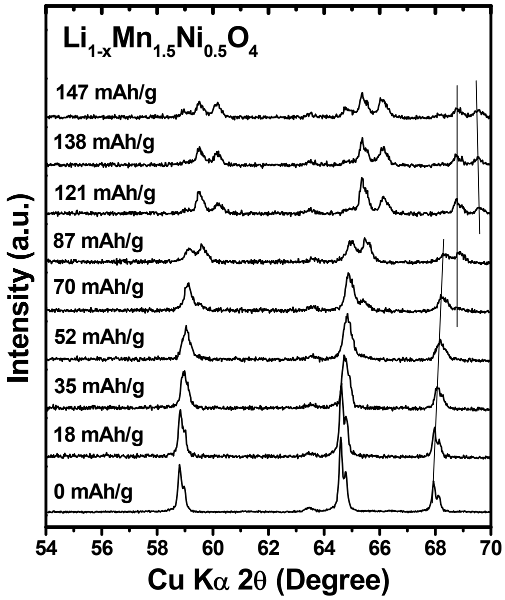

Figure 3.10: X-ray diffraction patterns of the 5 V spinel $Li_{1-x}Mn_{1.5}Ni_{0.5}O_4$ samples that were obtained by electrochemically extracting lithium.

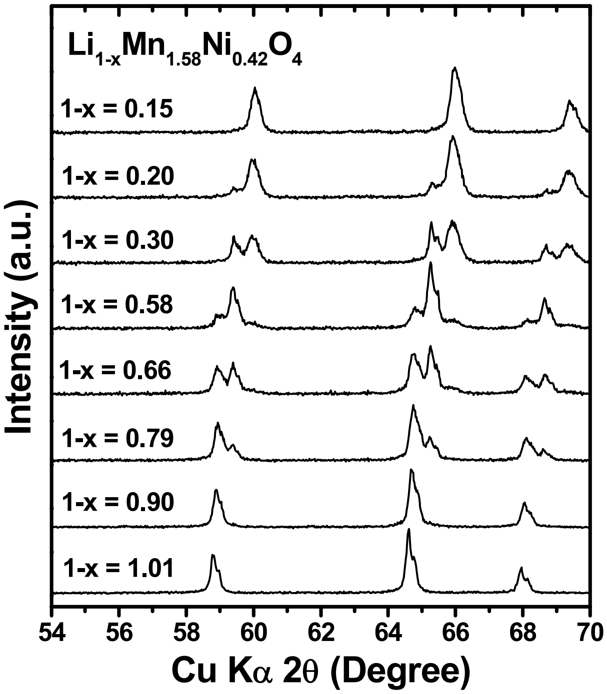

Figure 3.11: X-ray diffraction patterns of the 5 V spinel $Li_{1-x}Mn_{1.58}Ni_{0.42}O_4$ samples that were obtained by chemically extracting lithium with NO_2BF_4.

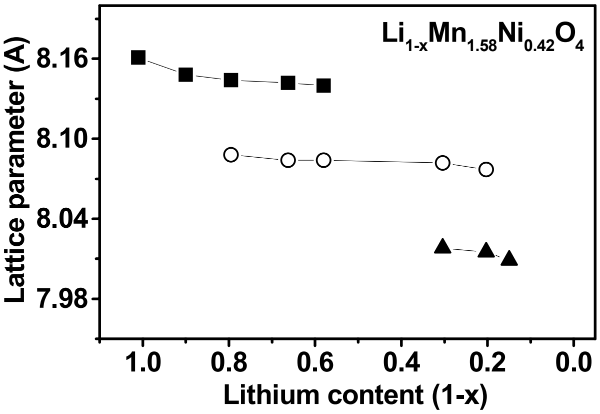

Figure 3.12: Variations of the lattice parameters with lithium content (1-x) in $Li_{1-x}Mn_{1.58}Ni_{0.42}O_4$: first cubic phase (■); second cubic phase (○); and third cubic phase (▲).

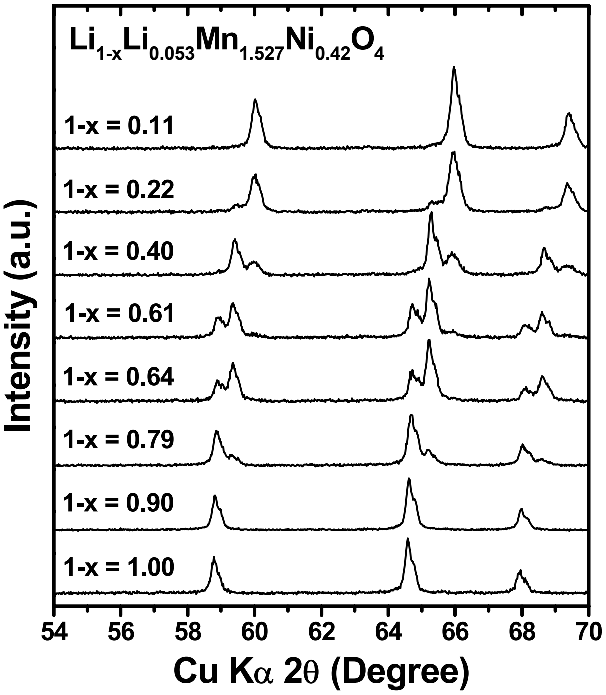

Figure 3.13: X-ray diffraction patterns of the 5 V spinel $Li_{1-x}Li_{0.053}Mn_{1.527}Ni_{0.42}O_4$ samples that were obtained by chemically extracting lithium with NO_2BF_4.

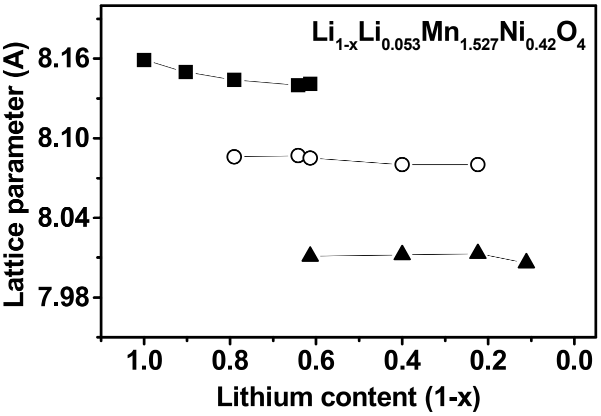

Figure 3.14: Variations of the lattice parameters with lithium content (1-x) in $Li_{1-x}Li_{0.053}Mn_{1.527}Ni_{0.42}O_4$: first cubic phase (■); second cubic phase (○); and third cubic phase (▲).

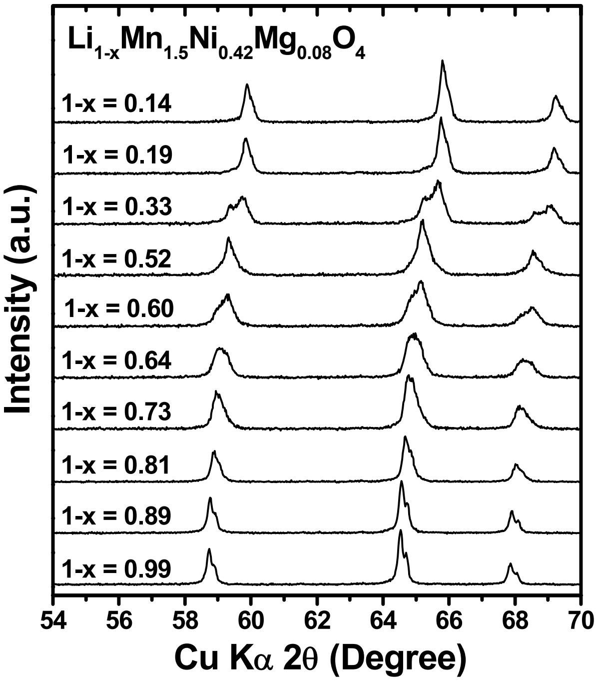

Figure 3.15: X-ray diffraction patterns of the 5 V spinel $Li_{1-x}Mn_{1.5}Ni_{0.42}Mg_{0.08}O_4$ samples that were obtained by chemically extracting lithium with NO_2BF_4.

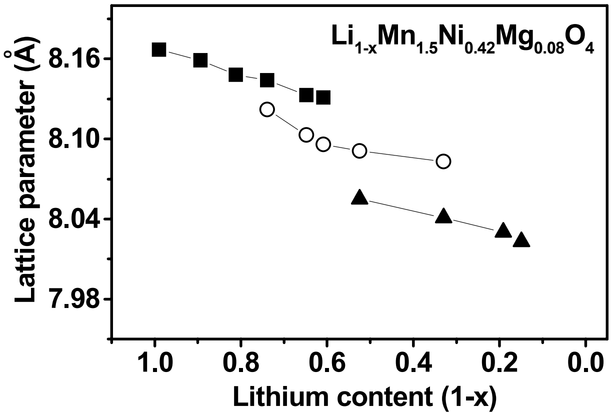

Figure 3.16: Variations of the lattice parameters with lithium content (1-x) in $Li_{1-x}Mn_{1.5}Ni_{0.42}Mg_{0.08}O_4$: first cubic phase (■); second cubic phase (○); and third cubic phase (▲).

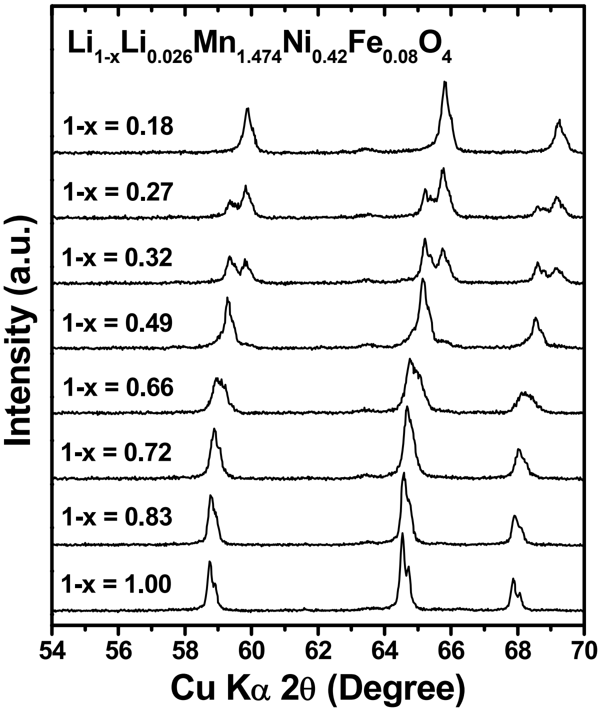

Figure 3.17: X-ray diffraction patterns of the 5 V spinel $Li_{1-x}Li_{0.026}Mn_{1.474}Ni_{0.42}Fe_{0.08}O_4$ samples that were obtained by chemically extracting lithium with NO_2BF_4.

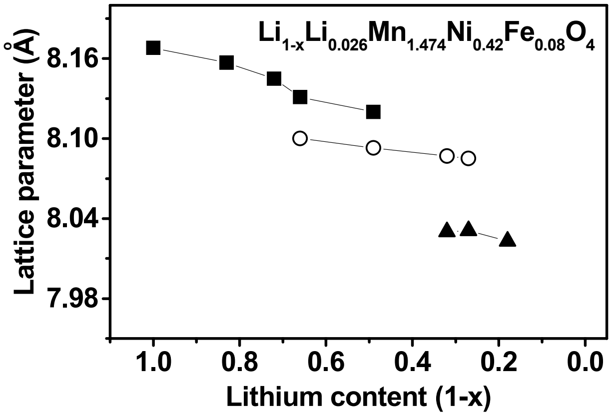

Figure 3.18: Variations of the lattice parameters with lithium content (1-x) in $Li_{1-x}Li_{0.026}Mn_{1.474}Ni_{0.42}Fe_{0.08}O_4$: first cubic phase (■); second cubic phase (○); and third cubic phase (▲).

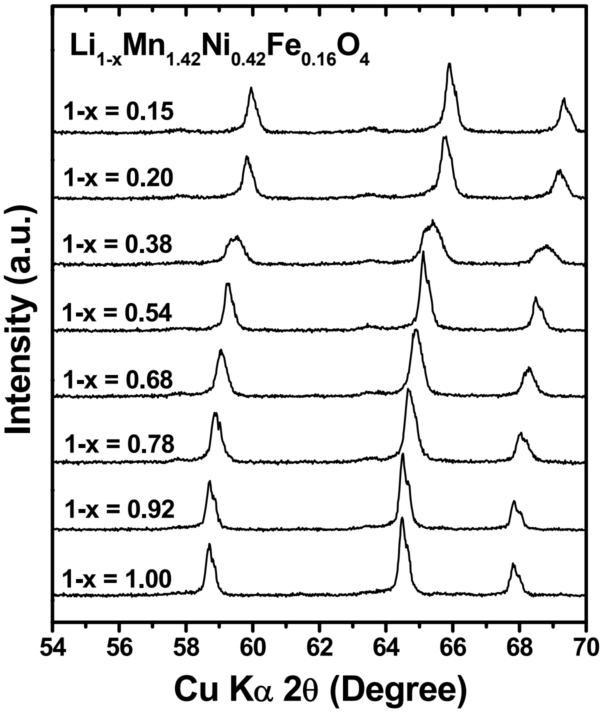

Figure 3.19: X-ray diffraction patterns of the 5 V spinel $Li_{1-x}Mn_{1.42}Ni_{0.42}Fe_{0.16}O_4$ samples that were obtained by chemically extracting lithium with NO_2BF_4.

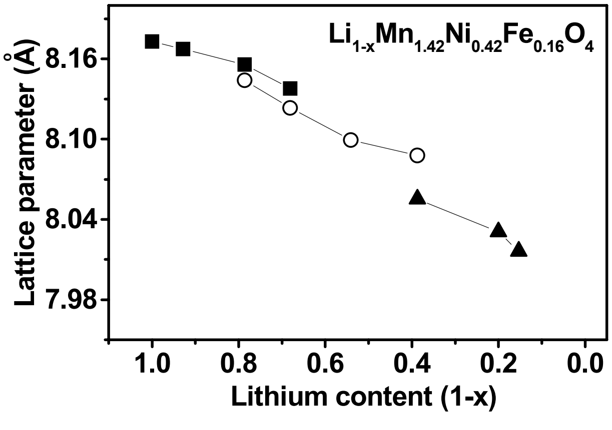

Figure 3.20: Variations of the lattice parameters with lithium content (1-x) in $Li_{1-x}Mn_{1.42}Ni_{0.42}Fe_{0.16}O_4$: first cubic phase (■); second cubic phase (○); and third cubic phase (▲).

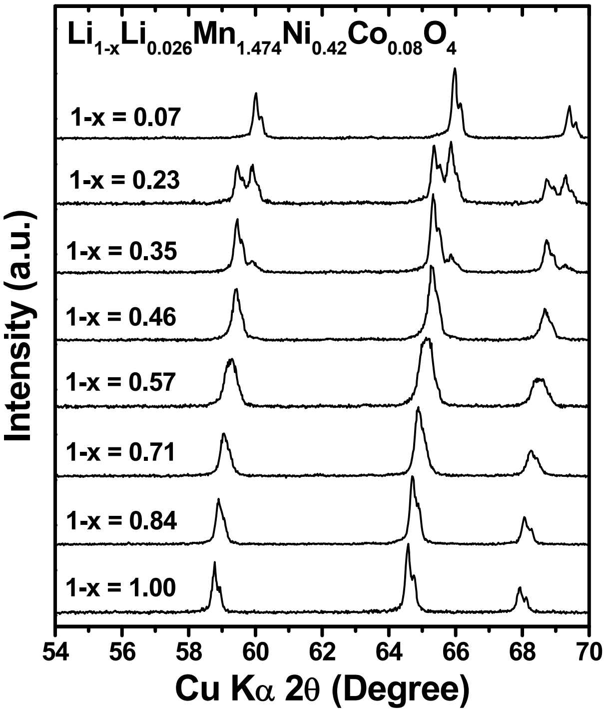

Figure 3.21: X-ray diffraction patterns of the 5 V spinel $Li_{1-x}Li_{0.026}Mn_{1.474}Ni_{0.42}Co_{0.08}O_4$ samples that were obtained by chemically extracting lithium with NO_2BF_4.

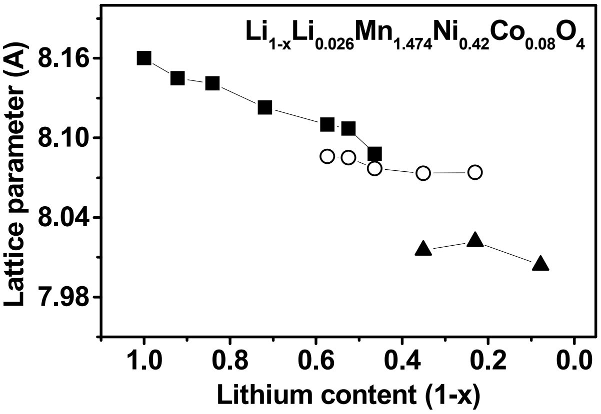

Figure 3.22: Variations of the lattice parameters with lithium content (1-x) in $Li_{1-x}Li_{0.026}Mn_{1.474}Ni_{0.42}Co_{0.08}O_4$: first cubic phase (■); second cubic phase (○); and third cubic phase (▲).

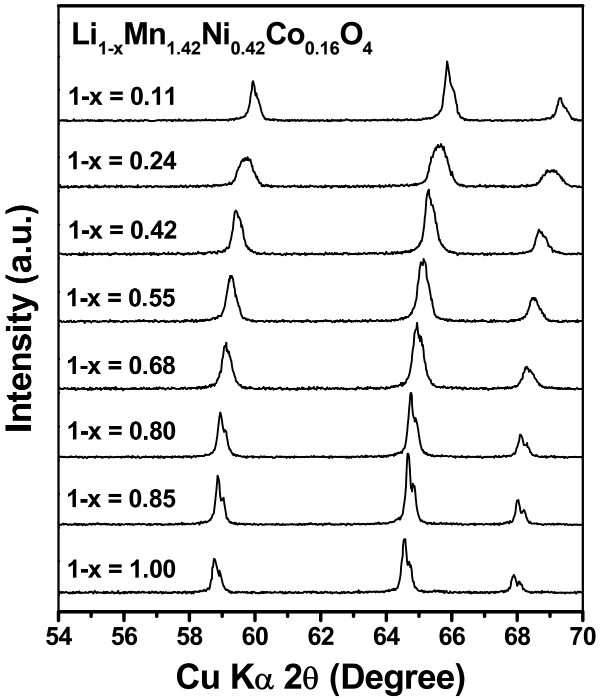

Figure 3.23: X-ray diffraction patterns of the 5 V spinel $Li_{1-x}Mn_{1.42}Ni_{0.42}Co_{0.16}O_4$ samples that were obtained by chemically extracting lithium with NO_2BF_4.

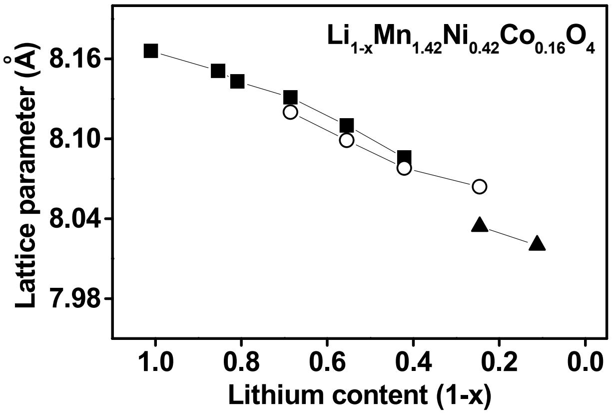

Figure 3.24: Variations of the lattice parameters with lithium content (1-x) in $Li_{1-x}Mn_{1.42}Ni_{0.42}Co_{0.16}O_4$: first cubic phase (■); second cubic phase (○); and third cubic phase (▲).

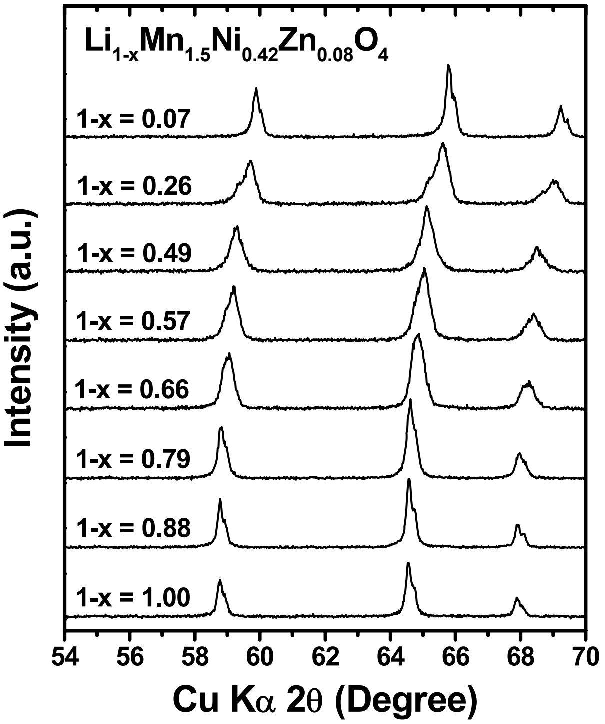

Figure 3.25: X-ray diffraction patterns of the 5 V spinel $Li_{1-x}Mn_{1.5}Ni_{0.42}Zn_{0.08}O_4$ samples that were obtained by chemically extracting lithium with NO_2BF_4.

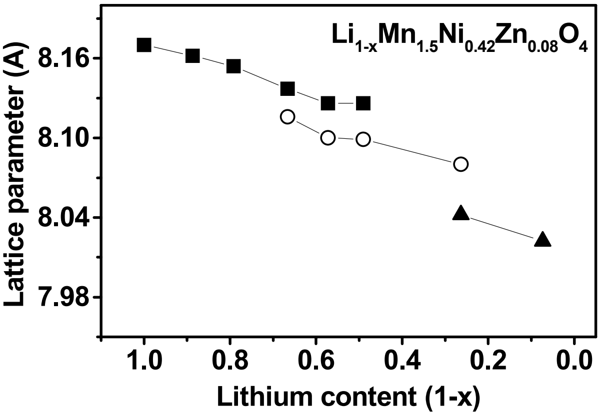

Figure 3.26: Variations of the lattice parameters with lithium content (1-x) in $Li_{1-x}Mn_{1.5}Ni_{0.42}Zn_{0.08}O_4$: first cubic phase (■); second cubic phase (○); and third cubic phase (▲).

Although the formation of three cubic phases is clearly evident from the distinct and well separated XRD reflections in a few systems such as $Li_{1-x}Mn_{1.5}Ni_{0.5}O_4$, $Li_{1-x}Mn_{1.58}Ni_{0.42}O_4$, and $Li_{1-x}Li_{0.053}Mn_{1.527}Ni_{0.42}O_4$, such a clear separation of reflections is not seen in systems such as $Li_{1-x}Mn_{1.42}Ni_{0.42}Fe_{0.16}O_4$, and $LiMn_{1.42}Ni_{0.42}Co_{0.16}O_4$; instead, the latter exhibits only broad peaks due to very close lattice parameter values between the cubic phases. For example, the $Li_{1-x}Mn_{1.42}Ni_{0.42}Co_{0.16}O_4$ sample exhibits broad reflections at (1-x) = 0.24 (two phase region) while the reflections are sharp enough to show the separation between the $K\alpha_1$ and $K\alpha_2$ peaks for (1-x) = 0.85 (single phase region). However, the broad peaks in the two-phase regions of the $Li_{1-x}Mn_{1.42}Ni_{0.42}Co_{0.16}O_4$ samples could be resolved into two cubic phases by Rietveld analysis and the lattice parameter values of the cubic phases are plotted in Figure 3.24.

3.3.3 Influence of lattice parameter differences between the cubic phases on the capacity fade of the 5 V spinel cathodes

Figure 3.27 compares the variations of the lattice parameter values of the cubic phases with lithium content (1-x) in $Li_{1-x}Mn_{1.5}Ni_{0.5}O_4$ and $Li_{1-x}Mn_{1.42}Ni_{0.42}Co_{0.16}O_4$ that were obtained by chemically extracting lithium with NO_2BF_4. While the three cubic phases formed with the $Li_{1-x}Mn_{1.5}Ni_{0.5}O_4$ system have a larger difference in the lattice parameter values, the difference is much smaller in the case of $Li_{1-x}Mn_{1.42}Ni_{0.42}Co_{0.16}O_4$. A superlattice structure with an ordered arrangement of manganese and nickel ions (space group: $P4_332$) as suggested by recent TEM and neutron diffraction studies has been proposed to be the reason for the formation of three cubic phases in the system $Li_{1-x}Mn_{1.5}Ni_{0.5}O_4$.[57,62-64] For each system, we measured the lattice parameter difference Δa_1 between the first and second cubic phases, and the lattice parameter difference Δa_2 between the second and third cubic phases, as shown in Figure 3.27.

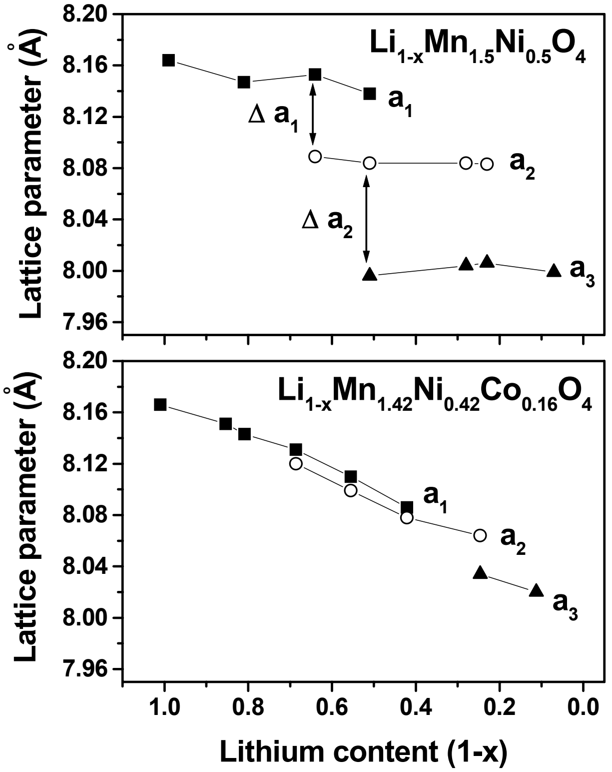

Figure 3.27: Variations of the lattice parameters with lithium content (1-x) in $Li_{1-x}Mn_{1.5}Ni_{0.5}O_4$ and $Li_{1-x}Mn_{1.42}Ni_{0.42}Co_{0.16}O_4$: first cubic phase (■); second cubic phase (○); and third cubic phase (▲).

Figure 3.28 relates the % capacity fade of several $LiMn_{1.5-y}Ni_{0.5-z}M_{y+z}O_4$ samples investigated in this study to the lattice parameter difference Δa_1, Δa_2, and the total lattice parameter difference $\Delta a_1 + \Delta a_2$. The % capacity fade decreases with decreasing lattice parameter difference (Δa_1 or Δa_2) between the cubic phases formed during the charge-discharge process similar to that found before by our group with the 4 V spinel system,[51,52] and $LiMn_{1.5}Ni_{0.5}O_4$ with the largest Δa_1 and Δa_2 shows the highest % capacity fade.

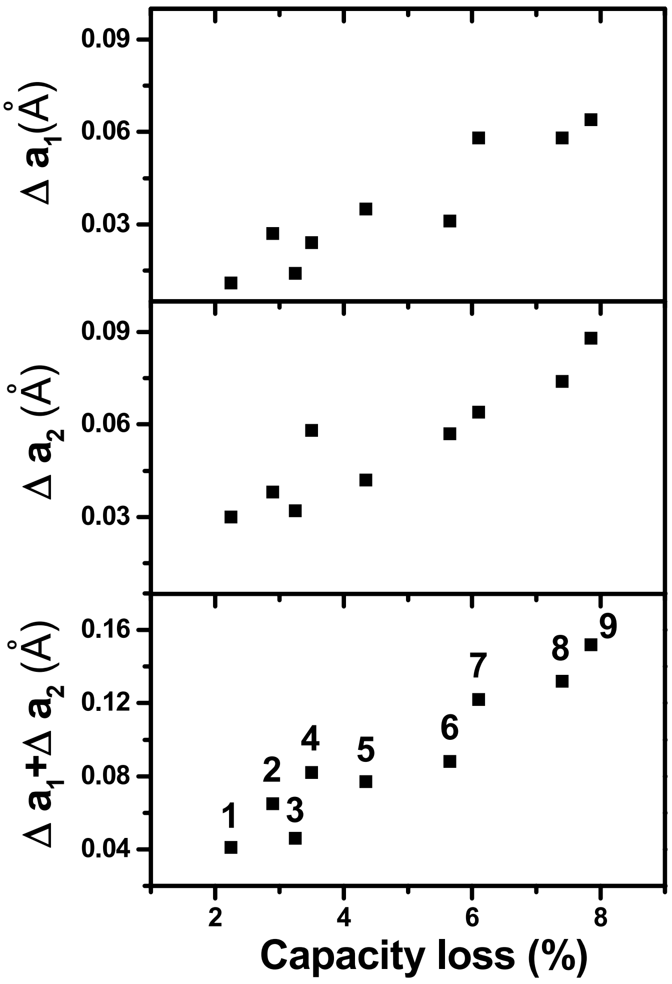

Figure 3.28: Correlation of the % capacity loss to the lattice parameter difference between the cubic phases formed during the charge-discharge process of the 5 V $LiMn_{1.5-y}Ni_{0.5-z}M_{y+z}O_4$ (M = Li, Mg, Fe, Co, and Zn) cathodes investigated in this study. Δa_1 is the maximum lattice parameter differences between the first and second cubic phases and Δa_2 is that between the second and third cubic phases formed during the charge-discharge process. (1) $Li_{1-x}Mn_{1.42}Ni_{0.42}Co_{0.16}O_4$, (2) $Li_{1-x}Mn_{1.5}Ni_{0.42}Zn_{0.08}O_4$, (3) $Li_{1-x}Mn_{1.42}Ni_{0.42}Fe_{0.16}O_4$, (4) $Li_{1-x}Li_{0.026}Mn_{1.474}Ni_{0.42}Co_{0.08}O_4$, (5) $Li_{1-x}Mn_{1.5}Ni_{0.42}Mg_{0.08}O_4$, (6) $Li_{1-x}Li_{0.026}Mn_{1.474}Ni_{0.42}Fe_{0.08}O_4$, (7) $Li_{1-x}Mn_{1.58}Ni_{0.42}O_4$, (8) $Li_{1-x}Li_{0.053}Mn_{1.527}Ni_{0.42}O_4$, and (9) $Li_{1-x}Mn_{1.5}Ni_{0.5}O_4$.

Interestingly, the lattice parameter difference between the fully discharged (before delithiation) and the fully charged (after the maximum possible delithiation) samples is approximately the same for each system investigated here. In other words, the overall volume change between the fully discharged and fully charged states remains approximately the same for each material, but the instantaneous volume change due to the lattice parameter difference between the different cubic phases formed during the charge-discharge process differs for each material. Therefore, the stress experienced during the instantaneous lattice parameter changes (Δa_1 and Δa_2) appears to play a more important role in the capacity fade of these spinel oxides. A large instantaneous volume change (e.g., 3.3% in $LiMn_{1.5}Ni_{0.5}O_4$) on going from one cubic phase to another cubic phase can lead to a breaking and loss of interparticle contact during charge-discharge cycling analogous to that occurring during Jahn-Teller distortion, resulting in poor Li^+ diffusion, electrical conductivity, and capacity retention. The instantaneous volume changes can also lead to the formation of new surfaces, enhancing the electrode-electrolyte reactivity. The 5 V and 4 V spinel oxide systems thus appear to exhibit a common dependence of the electrochemical performance on the lattice parameter differences among the cubic phases formed during the charge-discharge process.

3.3.4 Manganese ion dissolution from 5 V spinel cathodes

The manganese dissolution was evaluated for various cation substituted 5 V $LiMn_{1.5-y}Ni_{0.5-z}M_{y+z}O_4$ cathodes as per the procedure described in the experimental section. For comparison, the manganese dissolution of the 4 V spinel $LiMn_2O_4$ is presented in Table 3.1 along with the 5 V $LiMn_{1.5-y}Ni_{0.5-z}M_{y+z}O_4$ cathodes.[112] The degree of manganese dissolution is expressed as a % of the initial Mn content for all the samples investigated. The error in the % Mn dissolution values is ±0.1 %. The 4 V $LiMn_2O_4$ spinel in which manganese exists as $Mn^{3.5+}$ shows a high manganese dissolution of 5.3 %.

Interestingly, all the 5 V $LiMn_{1.5-y}Ni_{0.5-z}M_{y+z}O_4$ spinel cathodes in which manganese exists as Mn^{4+} exhibit a much lower Mn ion dissolution of < 1.0 % compared to $LiMn_2O_4$. The data reveals that the presence of Mn^{3+} leads to a significantly larger amount of manganese dissolution compared to Mn^{4+} due to the disproportionation of Mn^{3+} to Mn^{2+} and Mn^{4+}.[46] In addition, we are not able to find a clear correlation between the amount of Mn dissolution from the 5 V $LiMn_{1.5-y}Ni_{0.5-z}M_{y+z}O_4$ spinel cathodes and its electrochemical performance. For example, the unsubstituted $LiMn_{1.5}Ni_{0.5}O_4$ exhibiting the highest capacity loss shows the same amount of manganese dissolution (0.7 %) as the cation substituted $LiMn_{1.42}Ni_{0.42}Co_{0.16}O_4$ sample that exhibits a much better capacity retention.

Table 3.1: Manganese dissolution in spinel oxide cathodes.

Composition	Mn dissolution as a % of the initial Mn content
$LiMn_2O_4$	5.3
$LiMn_{1.5}Ni_{0.5}O_4$	0.7
$Li_{1.053}Mn_{1.527}Ni_{0.42}O_4$	0.4
$LiMn_{1.42}Ni_{0.42}Co_{0.16}O_4$	0.7
$Li_{1.026}Mn_{1.474}Ni_{0.42}Co_{0.08}O_4$	0.5
$LiMn_{1.5}Ni_{0.42}Zn_{0.08}O_4$	0.9
$LiMn_{1.5}Ni_{0.42}Mg_{0.08}O_4$	0.8

3.4 CONCLUSIONS

The cation-substituted $LiMn_{1.5-y}Ni_{0.5-z}M_{y+z}O_4$ (M = Li, Mg, Fe, Co, and Zn) spinel oxides exhibit better cyclability and rate capability in the 5 V region compared to the unsubstituted $LiMn_{1.5}Ni_{0.5}O_4$ cathodes although the degree of manganese dissolution does not vary significantly. The better electrochemical properties of $LiMn_{1.5-y}Ni_{0.5-z}M_{y+z}O_4$ are found to be due to a smaller lattice parameter difference among the three cubic phases formed during the charge-discharge process. The smaller or negligible instantaneous volume change is believed to suppress the stress involved and impart superior electrochemical properties. The excellent performance with moderate reversible capacities of around 120 mAh/g along with the low cost, low toxicity, and ease of synthesis may make the 5 V $LiMn_{1.5-y}Ni_{0.5-z}M_{y+z}O_4$ cathodes attractive for electric and hybrid electric vehicle applications.

CHAPTER 4

Proton Insertion and Oxygen Loss in the Spinel Oxide Systems

4.1 INTRODUCTION

Commercial lithium ion cells mostly employ the layered $LiCoO_2$ as the cathode material. However, only 50% of its theoretical capacity, corresponding to a reversible extraction of 0.5 Li per Co is utilized in practical cells. In comparison, the nickel and manganese rich compositions such as $LiMn_{1/2}Ni_{1/2}O_2$, $LiMn_{1/3}Co_{1/3}Ni_{1/3}O_2$, and $LiNi_{0.85}Co_{0.15}O_2$ exhibit a reversible extraction of 0.6 to 0.7 Li per transition metal ion[113-119] although they all have the same O3 type layered structure like $LiCoO_2$. To understand the factors controlling the reversible capacities, our group has been focusing on the chemical and structural characterization of bulk delithiated samples obtained by chemically extracting lithium from various oxide cathodes with the oxidizer NO_2BF_4 in acetonitrile medium.[23,24,29,120-123]

An analysis of the average oxidation state of the transition metal ions in some of the chemically delithiated layered oxide phases by a redox titration has shown that the oxidation state deviates from the theoretically expected value (solid line) and remains constant at deep lithium extraction although Li^+ ions are continuously being extracted (Figure 4.1). However, the lithium content at which the oxidation state begins to remain constant depends on the layered oxide system. The charge compensation during lithium extraction, while the oxidation state deviates from the theoretically expected value, could be accommodated by either a loss of oxygen from the lattice or an exchange of lithium ions by protons from the reaction medium. Either situation (ion exchange by protons or oxygen loss) may reflect the onset of chemical instability in the system. Thus the chemical delithiation experiments may serve as a tool to assess the relative chemical stability of the oxide cathodes with various transition metal ions. The deviation of the oxidation state from the theoretical value at a higher lithium content (1-x) < 0.5 in $Li_{1-x}CoO_2$ compared to that in the nickel and manganese rich systems ((1-x) < 0.4) in Figure 4.1 may imply a greater chemical instability and consequently a lower reversible capacity for the $LiCoO_2$ system.

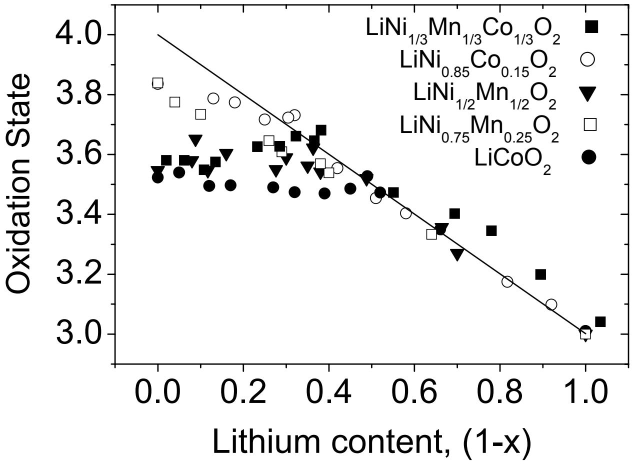

Figure 4.1: Comparisons of the variations of the average oxidation state of the transition metal ions with lithium content (1-x) in $Li_{1-x}Ni_{1-y-z}Mn_yCo_zO_2$.[24,29,122,123] The solid line refers to the theoretically expected oxidation state.

Previously, the constancy of the oxidation state of the transition metal ions at lower lithium contents was attributed to a loss of oxygen from the lattice, assuming no proton insertion (ion exchange of Li^+ by H^+) occuring during the chemical delithiation process considering the non-aqueous (acetonitrile) reaction medium.[23,24,29,120-123] However, there is a possibility of an ion exchange of Li^+ by H^+ ions that could be produced from acetonitrile in the presence of a powerful oxidizer like NO_2BF_4.[124] In this regard, ion-exchange of Li^+ by H^+ as well as loss of oxygen from the lattice have been reported by Robertson and Bruce[125,126] during the electrochemical charging of Li_2MnO_3 and $Li_xMn_{1-y}Li_yO_2$ beyond Mn^{4+}. Recently, a quantitative determination of proton contents in various chemically delithiated oxide cathodes has been carried out with Prompt Gamma Ray Activation Analysis (PGAA), and the results are complemented by mass spectrometric and thermogravimetric analysis data.[127] While the delithiated layered $Li_{1-x}CoO_2$, $Li_{1-x}Ni_{1/3}Mn_{1/3}Co_{1/3}O_2$, and $Li_{1-x}Ni_{1/2}Mn_{1/2}O_2$ oxides were shown to contain a significant amount of proton in the lattice at deep lithium extraction, orthorhombic $Li_{1-x}MnO_2$, spinel $Li_{1-x}Mn_2O_4$, and olivine $Li_{1-x}FePO_4$ were shown to be devoid of such proton insertion. In addition, using the charge neutrality principle, these oxides were shown not to loss any oxygen at deep lithium extraction.

In this chapter, the proton contents in the chemically delithiated $Li_{1-x}Mn_{1.58}Ni_{0.42}O_4$ and $Li_{1-x}Co_2O_4$ oxides are quantitatively determined using PGAA, in addition to the redox titrations and AAS analysis to find any oxygen loss from the system at deep lithium extraction. The results are further complemented by thermogravimetric analysis (TGA).

4.2 EXPERIMENTAL

The $LiMn_{1.58}Ni_{0.42}O_4$ spinel oxide was synthesized by a hydroxide precursor method as described in chapter 3. Low temperature $LiCoO_2$ that has a lithiated spinel structure $Li_2Co_2O_4$ was synthesized by firing a stoichiometric amount of Li_2CO_3 and Co_3O_4 at 400 °C in air for 1 week.[128-131] Chemical extraction of lithium from the oxide cathodes was carried out by stirring the oxide powders with an acetonitrile solution of NO_2BF_4 (oxide to NO_2BF_4 molar ratio was 1:2), as described in chapter 2. The lithium contents were determined by atomic absorption spectroscopy (AAS) and the oxidation state of the transition metal ions was determined by treating with a known excess of sodium oxalate and titrating the unreacted sodium oxalate with potassium permanganate.

TGA data was collected with a Perkin-Elmer Series 7 Thermogravimetric Analyzer with a heating rate of 3 °C/min in flowing air. Direct quantitative measurements of hydrogen contents in the chemically delithiated samples were carried out with Prompt Gamma-Ray Activation Analysis (PGAA).

4.3 RESULTS AND DISCUSSION

4.3.1 Proton insertion and oxygen loss in the $Li_{1-x}Mn_{1.58}Ni_{0.42}O_4$ and $Li_{1-x}Co_2O_4$ systems

Table 4.1 summarizes the hydrogen content, the lithium content, and the average oxidation states of the transition metal ions present in the delithiated $Li_{1-x}Mn_{1.58}Ni_{0.42}O_4$ and $Li_{1-x}Co_2O_4$ oxides as measured by, respectively, PGAA, AAS, and redox titration. Using the charge neutrality principle, the oxygen content present in the delithiated sample is calculated.

Table 4.1: Chemical analysis and PGAA data of the chemically delithiated (with NO_2BF_4 in acetonitrile medium) spinel oxide cathodes.

Compound	H^+ content from PGAA (atom)	Li content (atom)	Average oxidation state (M^{n+})	Delithiated composition
$LiMn_{1.58}Ni_{0.42}O_4$	0.00	0.08	3.96	$Li_{0.08}Mn_{1.58}Ni_{0.42}O_4$
$Li_2Co_2O_4$[a]	0.18	0.60	3.38	$H_{0.18}Li_{0.60}Co_2O_{3.77}$

[a] Low temperature $LiCoO_2$ that has a lithiated spinel ($Li_2Co_2O_4$) structure[128-131]

Similar to the 4 V spinel $Li_{1-x}Mn_2O_4$, the 5 V spinel $Li_{1-x}Mn_{1.58}Ni_{0.42}O_4$ does not encounter any proton insertion or oxygen loss from the lattice at deep lithium extraction. Interestingly, the spinel $Li_{1-x}Co_2O_4$ shows both proton insertion and oxygen loss at deep lithium extraction. While the expected amount of proton based on the lithium content and oxidation state analysis assuming no oxygen loss occurring from the lattice is 0.64, the PGAA data indicate a much lower proton content of 0.18. This suggests that the charge compensation in the spinel $Li_{1-x}Co_2O_4$ at deep lithium extraction may occur both by proton insertion into (an ion exchange of Li^+ by H^+) and oxygen loss from the lattice as shown in Table 4.1.

4.3.2 TGA analysis of the $Li_{1-x}Co_2O_4$ system

The composition of the chemically delithiated $Li_{1-x}Co_2O_4$ can also be determined by thermogravimetric analysis (TGA). The delithiated $Li_{1-x}Co_2O_4$ sample was heated to 600 °C in a thermogravimetric analyzer with a heating rate of 3 °C/min in flowing air as shown in Figure 4.2.

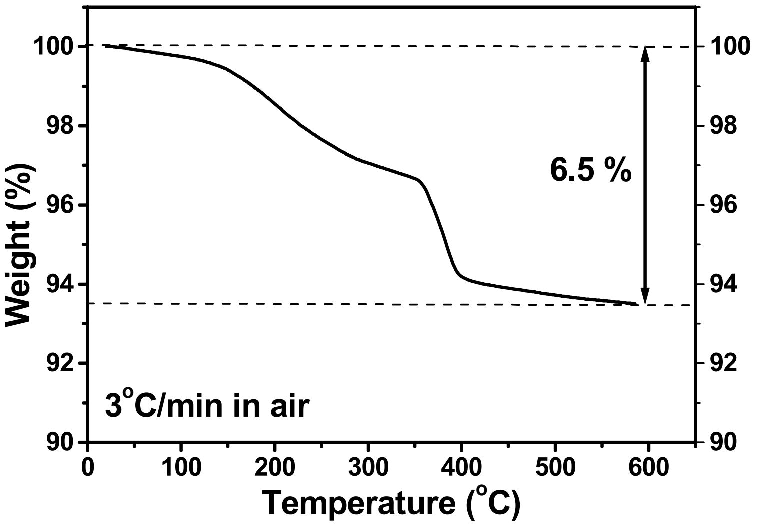

Figure 4.2: TGA plot of chemically delithiated $Li_{1-x}Co_2O_4$ oxide.

The observed weight loss of 6.5 % is smaller than the value (8.3 %) expected for the formula $H_{0.64}Li_{0.60}Co_2O_4$ (assuming only proton insertion), but higher than the value (5.4 %) expected for the formula $Li_{0.60}CoO_{3.68}$ (assuming only oxygen loss), with the final product after the TGA experiment to be (0.6)$LiCoO_2$ and (1.4/3)Co_3O_4 as indicated by the XRD data. Based on the observed weight loss and charge neutrality principle, the composition was determined to be $H_{0.24}Li_{0.60}Co_2O_{3.80}$, which is in close agreement with the composition $H_{0.18}Li_{0.60}Co_2O_{3.77}$ reported in Table 4.1 using PGAA. Thus, the chemical instability associated with the $Co^{3+/4+}$ couple is largely relieved by a loss of oxygen from the lattice in the case of spinel $Li_{1-x}Co_2O_4$ possibly due to the difficulty of incorporating protons into the spinel lattice in contrast to the layered $Li_{1-x}CoO_2$ lattice.

4.4 CONCLUSIONS

The possibility of proton incorporation into and oxygen loss from the lattice during the chemical delithiation process has been investigated with $Li_{1-x}Mn_{1.58}Ni_{0.42}O_4$ and $Li_{1-x}Co_2O_4$ spinel oxide cathodes. The spinel $Li_{1-x}Mn_{1.58}Ni_{0.42}O_4$ does not encounter any proton insertion or oxygen loss from the lattice at deep lithium extraction. However, the spinel $Li_{1-x}Co_2O_4$ shows both proton insertion and oxygen loss at deep lithium extraction. The differences could be related to the differences in the relative positions of the transition metal ion $M^{n+/(n+1)+}$:3d band with respect to the top of the O^{2-}:2p band and the consequent chemical instability arising from an introduction of significant amount of holes into the O^{2-}:2p band at deep lithium extraction. For example, a significant overlap of the $Co^{3+/4+}$:3d band with the top of the O^{2-}:2p band results in an ion exchange of Li^+ by H^+ and an oxygen loss from the lattice at deep lithium extraction in $Li_{1-x}Co_2O_4$ to relieve the chemical instability while the lying of the $Mn^{3+/4+}$:3d and $Ni^{2+/4+}$:3d bands well above the top of the O^{2-}:2p band in $Li_{1-x}Mn_{1.58}Ni_{0.42}O_4$ avoids such chemical instabilities (Figure 1.7).

CHAPTER 5

Chemical and Electrochemical Characterization of Complex Layered Cathodes in the $Li[Li_{1/3}Mn_{2/3}]O_2$ - $LiCoO_2$ - $LiNiO_2$ Solid Solution

5.1 INTRODUCTION

As mentioned in chapter 1, lithium ion batteries are becoming increasingly popular for portable electronic devices such as cellular phones and laptops due to their higher volumetric and gravimetric energy densities. Most commercial lithium ion cells are presently made with the layered $LiCoO_2$ cathode, but only 50% of its theoretical capacity can be utilized in practical cells (140 mAh/g) due to the chemical and structural instabilities at deep charge with $(1-x) < 0.5$ in $Li_{1-x}CoO_2$.[24] Also, Co is relatively toxic and expensive. These drawbacks have prompted interest in alternative cathodes materials. Recently, solid solutions between layered $LiMO_2$ ($M = Mn_{0.5}Ni_{0.5}$,[116,132-135] Co,[136,137] and Ni[138,139]) and layered Li_2MnO_3 are being intensively pursued as some of them exhibit high capacities of around 250 mAh/g at a lower cost compared to $LiCoO_2$. Layered Li_2MnO_3 has the same O3 type structure as $LiCoO_2$, but with one-third of the transition metal ion sites occupied by lithium ions in the transition metal layer as $Li[Li_{1/3}Mn_{2/3}]O_2$. Although $Li[Li_{1/3}Mn_{2/3}]O_2$ is electrochemically inactive as it is difficult to oxidize beyond Mn^{4+}, its solid solutions with other $LiMO_2$ oxides exhibit good electrochemical activity.

The discharge capacities of the above mentioned solid solution cathodes are often much higher than the theoretical capacity values expected based on the initial oxidation states of Mn, Co, and Ni. Also, the first charge profile is accompanied by an irreversible voltage plateau around 4.5 V, which has been confirmed from both *in-situ* X-ray diffraction[140] and differential electrochemical mass spectrometry studies[134] to be due to an irreversible loss of oxygen from the lattice for charging involving oxidation beyond the formal oxidation states of Mn^{4+}, Ni^{4+}, and Co^{4+}. The oxygen loss leads to a lowering of the oxidation states of transition metal ions correspondingly at the end of first discharge, which facilitates a higher reversible capacity in subsequent cycles. However, the amount of oxygen loss from the lattice and the reversible capacity values differ significantly depending upon the composition of the $Li[Li_{1/3}Mn_{2/3}]O_2$ - $LiMO_2$ solid solutions. Moreover, the irreversible loss of oxygen from the lattice has been found recently to be sensitively suppressed by a substitution of small amount of Al^{3+} for Li^{+} or F^{-} for O^{2-}.[141]

With an aim to understand the factors that control the degree of oxygen loss and the subsequent capacity values, we investigate a new series of cathodes (1-z) $Li[Li_{1/3}Mn_{2/3}]O_2 \cdot (z)\ Li[Co_{1-y}Ni_y]O_2$ ($0 \leq y \leq 1$ and $0.2 \leq z \leq 0.7$) belonging to a solid solution between $Li[Li_{1/3}Mn_{2/3}]O_2$ - $LiCoO_2$ - $LiNiO_2$ and a comparison of their electrochemical performances in lithium cells. To understand the variations in electrochemical properties with composition, we also focus on the chemical characterization of the samples obtained by chemically extracting lithium with an oxidizer NO_2BF_4 in acetonitrile medium on the solid solution samples synthesized at two different temperatures (900 and 750 °C).

5.2 EXPERIMENTAL

The samples were synthesized by a hydroxide precursor method, as described in chapter 2, and fired in air at 900 °C for 12 h followed by quenching into liquid nitrogen. In order to understand the influence of synthesis temperatures, a second set of samples were also synthesized by firing at 750 °C instead of 900 °C. Chemical extraction of lithium was carried out by stirring the layered oxide powder with an acetonitrile solution of the oxidizer NO_2BF_4, as described before in chapter 2.[24,127]

All the samples were characterized by X-ray diffraction (XRD) and the lattice parameters were calculated with a Rietveld analysis of the XRD data.[107] The lithium contents in the parent and chemically delithiated samples were determined by atomic absorption spectroscopy (AAS). The average oxidation state of the transition metal ions in the parent and delithiated samples was determined by treating the samples with a known excess of sodium oxalate and titrating the unreacted sodium oxalate with potassium permanganate. Since there is a possibility of ion exchange of Li^+ ions by H^+ ions that could be produced by an oxidation of acetonitrile by the powerful oxidizer NO_2BF_4 during chemical delithiation, direct quantitative measurements of hydrogen contents in the chemically delithiated samples were carried out with prompt gamma-ray activation analysis (PGAA) by irradiating the samples for 2 h at a reactor power of 950 kW.[110,111] Electrochemical performances were evaluated with CR2032 coin cells at 12.5 mA/g (~ C/20 rate) between 4.8 and 2.0 V. The cathodes for evaluating the electrochemical performances were prepared as described in chapter 2.

5.3 RESULTS AND DISCUSSION

5.3.1 (1-z) $Li[Li_{1/3}Mn_{2/3}]O_2 \cdot$ (z) $Li[Co_{1-y}Ni_y]O_2$ ($0 \leq y \leq 1$ and $z = 0.5$) series synthesized at 900 °C

5.3.1.1 Crystal chemistry

The compositions studied in the (1-z) $Li[Li_{1/3}Mn_{2/3}]O_2 \cdot$ (z) $Li[Co_{1-y}Ni_y]O_2$ ($0 \leq y \leq 1$ and $z = 0.5$) solid solution series are indicated by closed circles in Figure 5.1. While the $Li[Li_{1/3}Mn_{2/3}]O_2$ and $LiCo_{1-y}Ni_yO_2$ contents in the solid solution are kept at 1:1 (50 mol % $Li[Li_{1/3}Mn_{2/3}]O_2$ and 50 mol % $LiCo_{1-y}Ni_yO_2$), the Ni content y in $LiCo_{1-y}Ni_yO_2$ is varied from 0 to 1. Table 5.1 gives the nominal composition and the observed compositions based on the experimentally determined lithium contents and the average oxidation state of the transition metal ions for the samples synthesized at 900 °C. The observed lithium content decreases with increasing Ni content y due to the difficulty of stabilizing Ni^{3+} and a consequent reduction of some Ni^{3+} to Ni^{2+} and volatilization of some lithium during synthesis at 900 °C. The calculated oxidation state values of nickel based on the experimentally observed compositions assuming Mn^{4+}, Co^{3+}, and Li^{+} are significantly lower (2.54+ to 2.62+) than the theoretically expected oxidation state of 3+ based on the nominal composition.

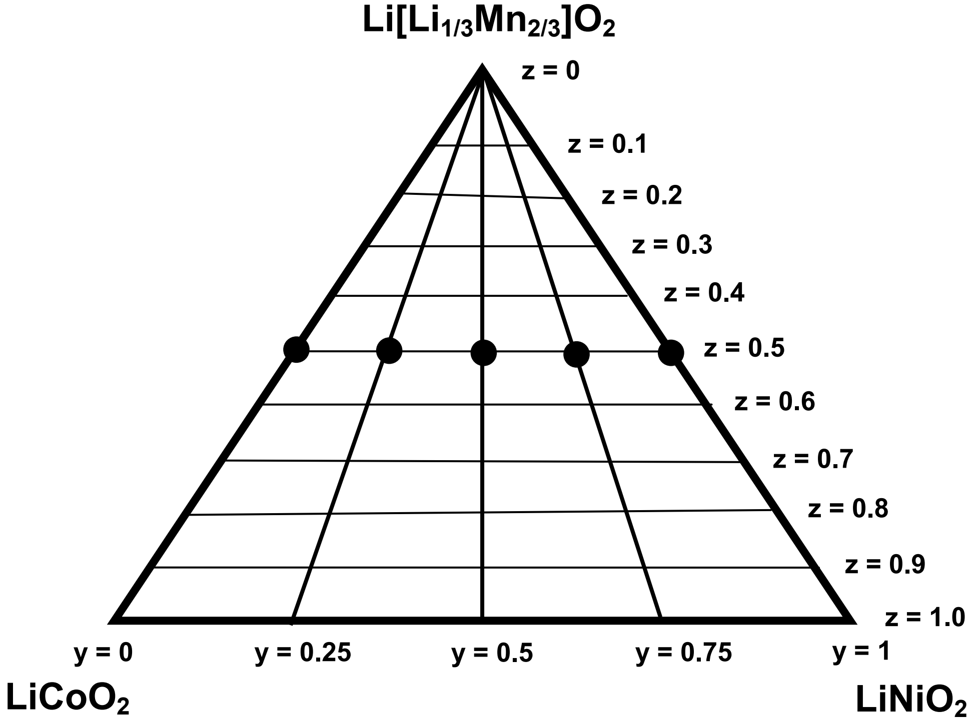

Figure 5.1: Phase diagram of the $Li[Li_{1/3}Mn_{2/3}]O_2$ - $LiCoO_2$ - $LiNiO_2$ system. The compositions studied in the (1-z) $Li[Li_{1/3}Mn_{2/3}]O_2 \cdot$ (z) $Li[Co_{1-y}Ni_y]O_2$ ($0 \leq y \leq 1$ and $z = 0.5$) system are indicated by closed circles.

Table 5.1: Observed chemical compositions and electrochemical data of (1-z) $Li[Li_{1/3}Mn_{2/3}]O_2 \cdot (z) Li[Co_{1-y}Ni_y]O_2$ ($0 \le y \le 1$ and $z = 0.5$) samples synthesized at 900 °C.

y	**z**	**Nominal composition**	**Observed composition**	**M^{n+}**	**Observed 1st charge capacity[a] (mAh/g)**			**Theoretical 1st charge capacity in region A[b] (mAh/g)**	**First discharge capacity (mAh/g)**
					Region A	**Region B**	**Total (regions A+B)**		
0		**$Li[Li_{0.17}Mn_{0.33}Co_{0.5}]O_2$**	**$Li[Li_{0.17}Mn_{0.33}Co_{0.5}]O_2$**	**3.41**	**100**	**233**	**333**	**92**	**269**
0.25		**$Li[Li_{0.17}Mn_{0.33}Co_{0.375}Ni_{0.125}]O_2$**	**$Li[Li_{0.14}Mn_{0.34}Co_{0.39}Ni_{0.13}]O_2$**	**3.33**	**135**	**181**	**316**	**127**	**233**
0.5	**0.5**	**$Li[Li_{0.17}Mn_{0.33}Co_{0.25}Ni_{0.25}]O_2$**	**$Li[Li_{0.12}Mn_{0.36}Co_{0.26}Ni_{0.26}]O_2$**	**3.27**	**150**	**155**	**305**	**159**	**205**
0.75		**$Li[Li_{0.17}Mn_{0.33}Co_{0.125}Ni_{0.375}]O_2$**	**$Li[Li_{0.10}Mn_{0.36}Co_{0.13}Ni_{0.41}]O_2$**	**3.22**	**185**	**92**	**277**	**190**	**208**
1		**$Li[Li_{0.17}Mn_{0.33}Ni_{0.5}]O_2$**	**$Li[Li_{0.08}Mn_{0.37}Ni_{0.55}]O_2$**	**3.17**	**234**	**0[c]**	**234**	**220**	**194**

[a] Regions A and B correspond to, respectively, the initial sloping region A and the plateau region B as marked in Figure 5.4.

[b] Calculated assuming the oxidation of Mn, Ni, and Co, respectively, to Mn^{4+}, Ni^{4+}, and $Co^{3.6+}$.

[c] The sample does not show a clearly recognizable plateau region.

Figure 5.2 compares the XRD patterns of the samples synthesized at 900 °C for various values of y in (1-z) $Li[Li_{1/3}Mn_{2/3}]O_2 \cdot$ (z) $Li[Co_{1-y}Ni_y]O_2$ ($0 \leq y \leq 1$ and $z = 0.5$). All the samples were found to be single phase, crystallizing in the layered α-$NaFeO_2$ structure (O3 type structure). However, the separation between the (018) and (110) reflections decrease gradually as the Ni content increases, suggesting an increase in the cation disorder between the lithium (3a sites) and transition metal (3b sites) planes.

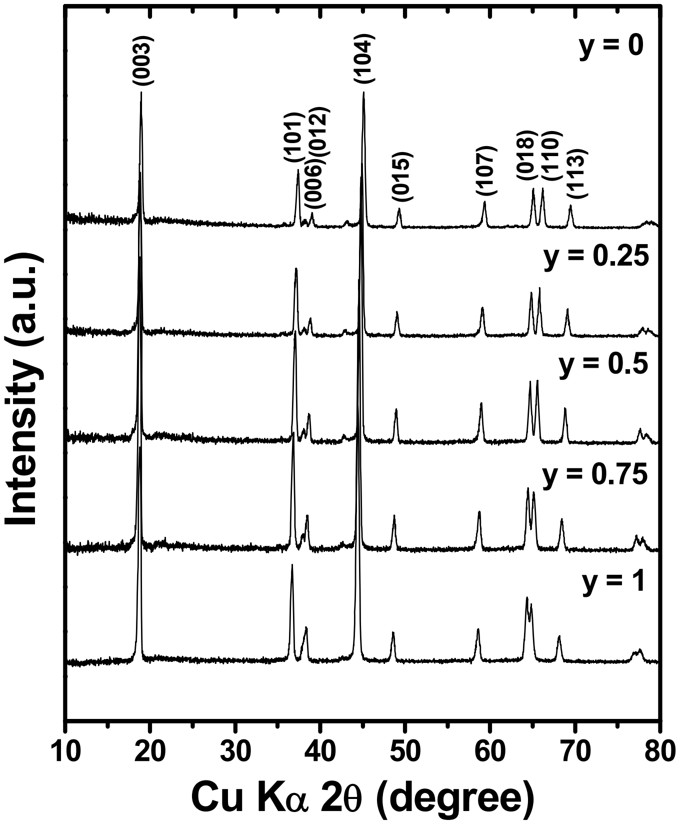

Figure 5.2: XRD patterns of (1-z) $Li[Li_{1/3}Mn_{2/3}]O_2 \cdot$ (z) $Li[Co_{1-y}Ni_y]O_2$ ($0 \leq y \leq 1$ and $z = 0.5$) samples synthesized at 900 °C.

Figure 5.3 shows the variations in the lattice parameters, *c/a* ratio, and % cation disorder as determined by the Rietveld analysis for the (1-z) $Li[Li_{1/3}Mn_{2/3}]O_2 \cdot$ (z) $Li[Co_{1-}$

$_y$Ni$_y$]O$_2$ ($0 \leq y \leq 1$ and $z = 0.5$) solid solution series. The *a* and *c* parameters increase with Ni content while the *c/a* ratio decreases. The increase in lattice parameters can be attributed to the substitution of a larger Ni^{3+} (0.0560 nm) or Ni^{2+} (0.0690 nm) ions for Co^{3+} (0.0545 nm) ions.[142] On the other hand, the decrease in *c/a* ratio with Ni content is due to the increasing cation disorder. The formation of Ni^{2+} ions with a substitution of Ni for Co and a small size and charge difference between Ni^{2+} (0.0690 nm) and Li^+ (0.076 nm) compared to those between Co^{3+} (0.0545 nm) or Mn^{4+} (0.053 nm) and Li^+ lead to an increase in cation disorder.

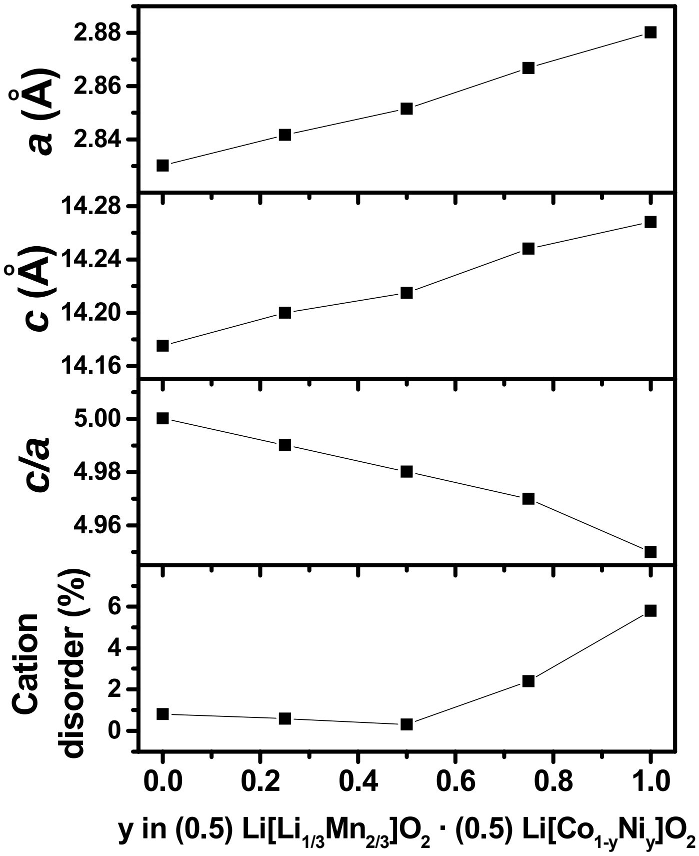

Figure 5.3: Variations of the lattice parameters *a* and *c*, *c/a* ratio, and cation disorder (fraction of lithium sites occupied by transition metal ions in the lithium layer) with y in (1-z) Li[Li$_{1/3}$Mn$_{2/3}$]O$_2$ · (z) Li[Co$_{1-y}$Ni$_y$]O$_2$ ($0 \leq y \leq 1$ and $z = 0.5$) samples synthesized at 900 °C.

5.3.1.2 Electrochemical performance

Figure 5.4 compares the first charge-discharge profiles (at 2.0 - 4.8 V and 12.5 mA/g, which corresponds to approximately C/20 rate for y = 0 and C/15 rate for y = 1) of the (1-z) $Li[Li_{1/3}Mn_{2/3}]O_2 \cdot (z) Li[Co_{1-y}Ni_y]O_2$ ($0 \leq y \leq 1$ and $z = 0.5$) samples synthesized at 900 °C. The samples exhibit two regions (A and B) during the first charge that are separated by a dashed vertical line in Figure 5.4. The y = 1 sample does not show any clear transition between the two regions and so it is not indicated in Figure 5.4. While the initial sloping region A below about 4.5 V corresponds to the oxidation of the transition metal ions to M^{4+}, the plateau region B around 4.5 V corresponds to an oxidation of O^{2-} ions and an irreversible loss of oxygen from the lattice as pointed out in the introduction section.[132-140] Table 5.1 compares the first charge capacity values in the two regions A and B and the first discharge capacity for all the samples. The total first charge capacity (regions A + B) and the discharge capacity decrease with increasing Ni content. However, while the first charge capacity in the initial sloping region A increases that in the plateau region B decreases with increasing Ni content. The former is due to an increasing amount of Ni^{2+} and its oxidation to Ni^{4+} during first charge. Table 5.1 also gives the theoretical value of the first charge capacity in region A, calculated based on the oxidation of the transition metal ions to Mn^{4+}, Ni^{4+}, and $Co^{3.6+}$. A close agreement between this theoretical value and the charge capacity in the sloping region A suggests that it may be difficult to oxidize Co beyond 3.6+ without oxidizing the oxide ions. This could be due to a significant overlap of the $Co^{3+/4+}$:3d band with the top of the O^{2-}:2p band and a consequent introduction of holes into the O^{2-}:2p band for oxidations beyond $Co^{3.6+}$, which is consistent with the limited practical capacity (50 %) of $LiCoO_2$.[121,127]

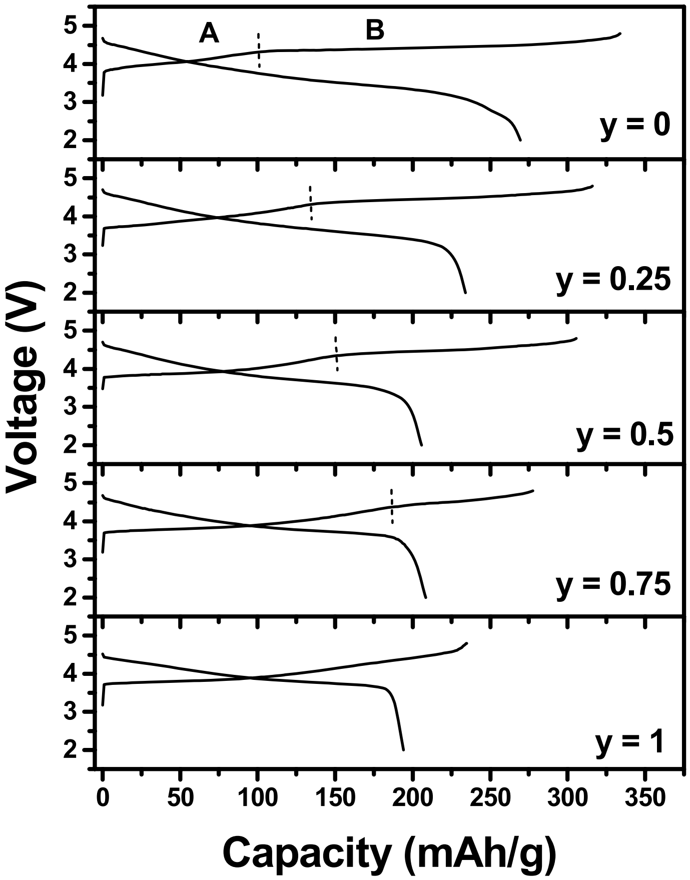

Figure 5.4: Comparison of the first charge-discharge profiles (recorded at 12.5 mA/g between 2.0 - 4.8 V) of the (1-z) $Li[Li_{1/3}Mn_{2/3}]O_2 \cdot$ (z) $Li[Co_{1-y}Ni_y]O_2$ ($0 \leq y \leq 1$ and $z = 0.5$) samples synthesized at 900 °C. The dashed vertical lines separate the initial sloping region A from the plateau region B.

Figure 5.5 compares the cyclability of the samples (synthesized at 900 °C) for various y values at 12.5 mA/g between 2.0 - 4.8 V. The cyclability does not vary much with Ni content. However, the samples with an intermediate Ni content of around 0.5 show slightly better cyclability than the y = 0 or y = 1 samples. This could be related to the chemical instabilities that could occur at deep charge (high charge voltages) with higher Co contents and a significant cation disorder that occurs with higher Ni contents. Both chemical instability and cation disorder can cause capacity fade.

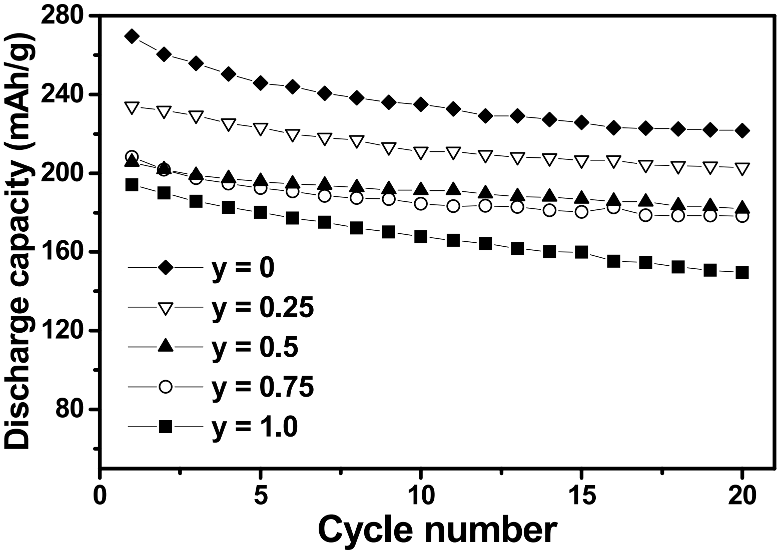

Figure 5.5: Comparison of the cyclability data (12.5 mA/g between 2.0 – 4.8 V) of the (1-z) $Li[Li_{1/3}Mn_{2/3}]O_2 \cdot (z) Li[Co_{1-y}Ni_y]O_2$ ($0 \leq y \leq 1$ and $z = 0.5$) samples synthesized at 900 °C.

5.3.1.3 Chemical stability of delithiated samples

In order to understand the factors that control the reversible capacity values, we focused on the chemical characterizations of bulk samples obtained by chemically extracting lithium from layered (1-z) $Li[Li_{1/3}Mn_{2/3}]O_2 \cdot (z) Li[Co_{1-y}Ni_y]O_2$ ($0 \leq y \leq 1$ and $z = 0.5$) samples synthesized at 900 °C with the oxidizer NO_2BF_4 in acetonitrile medium. Table 5.2 gives the compositions of the delithiated samples that were calculated based on the experimentally determined lithium content, proton content, and oxidation state values, respectively, by atomic absorption spectroscopy, prompt gamma-ray activation analysis, and redox titration. The delithiated samples contain some residual lithium and inserted protons in the lithium plane. The proton content is due to an ion exchange of Li^+ ions by

H^+ ions that are generated by an oxidation of acetonitrile by the powerful oxidizer NO_2BF_4.[127]

The compositions given in Table 5.2 indicate that the amount of oxygen lost during chemical delithiation decreases with increasing Ni content, which is consistent with a decreasing plateau region B in the first charge profiles given in Figure 5.4. The decrease in oxygen loss with increasing Ni content could be understood by considering the experimentally determined chemical compositions for the parent samples and a mechanism proposed by Armstrong *et al*[134] recently for the system $Li[Li_{0.2}Mn_{0.6}Ni_{0.2}]O_2$, which is a solid solution between $Li[Li_{1/3}Mn_{2/3}]O_2$ and $Li[Mn_{0.5}Ni_{0.5}]O_2$. Based on neutron powder diffraction data, Armstrong *et al*[134] suggested that the oxygen loss from the surface of the particle is accompanied by a migration of Li^+ ions from 3b octahedral sites in the transition metal layer into the 3a octahedral sites in the lithium layer, generating cation vacancies in the transition metal layer, which are subsequently filled by a cooperative displacement and diffusion of transition metal ions from the surface to the bulk of the particle. Such a rearrangement will result in the formation of a layered structure in which the 3b octahedral sites in the transition metal layer are occupied exclusively by the transition metal ions. Based on this hypothesis, the oxygen evolution from the lattice will cease when all the Li^+ ion vacancies in the transition metal layer (3b sites) are filled by the transition metal ions diffusing from the surface to the bulk. Thus, one would expect the limiting (or lowest) oxygen content value in the delithiated sample to be twice that of the transition metal ion content or the maximum amount of oxygen loss from the lattice to be twice the amount of lithium in the transition metal layer.

Table 5.2: Chemical analysis data of chemically delithiated (1-z) $Li[Li_{1/3}Mn_{2/3}]O_2 \cdot$ (z) $Li[Co_{1-y}Ni_y]O_2$ ($0 \leq y \leq 1$ and z = 0.5) samples synthesized at 900 °C.

y	z	Observed parent composition	Observed composition after chemical delithiation[a]		M^{n+}	Calculated limiting oxygen content (2-δ)[b]
			Before rearrangement	After rearrangement		
0	0.5	$Li[Li_{0.17}Mn_{0.33}Co_{0.5}]O_2$	$Li_{0.04}H_{0.18}[Li_{0.17}Mn_{0.33}Co_{0.5}]O_{1.66}$	$Li_{0.25}H_{0.22}[Mn_{0.4}Co_{0.6}]O_2$	3.53	1.66
0.25		$Li[Li_{0.14}Mn_{0.34}Co_{0.39}Ni_{0.13}]O_2$	$Li_{0.09}H_{0.15}[Li_{0.14}Mn_{0.34}Co_{0.39}Ni_{0.13}]O_{1.72}$	$Li_{0.27}H_{0.17}[Mn_{0.40}Co_{0.45}Ni_{0.15}]O_2$	3.56	1.72
0.5		$Li[Li_{0.12}Mn_{0.36}Co_{0.26}Ni_{0.26}]O_2$	$Li_{0.05}H_{0.18}[Li_{0.12}Mn_{0.36}Co_{0.26}Ni_{0.26}]O_{1.78}$	$Li_{0.18}H_{0.20}[Li_{0.01}Mn_{0.41}Co_{0.29}Ni_{0.29}]O_2$	3.65	1.76
0.75		$Li[Li_{0.10}Mn_{0.36}Co_{0.13}Ni_{0.41}]O_2$	$Li_{0.07}H_{0.18}[Li_{0.10}Mn_{0.36}Co_{0.13}Ni_{0.41}]O_{1.84}$	$Li_{0.16}H_{0.20}[Li_{0.02}Mn_{0.39}Co_{0.14}Ni_{0.45}]O_2$	3.70	1.80
1.0		$Li[Li_{0.08}Mn_{0.37}Ni_{0.55}]O_2$	$Li_{0.12}H_{0.15}[Li_{0.08}Mn_{0.37}Ni_{0.55}]O_{1.90}$	$Li_{0.18}H_{0.16}[Li_{0.03}Mn_{0.39}Ni_{0.58}]O_2$	3.75	1.84

[a] Determined based on the experimentally observed lithium and proton contents and oxidation state values.

[b] Calculated based on the maximum amount of oxygen the sample could lose (see text).

Table 5.2 gives the limiting oxygen content values calculated based on the above mechanism as well as the observed chemical compositions after the cation rearrangement (obtained by normalizing the oxygen content to 2.0). The calculated limiting oxygen content values agree closely with the observed oxygen content values in the delithiated samples (see the formula before cation rearrangement) particularly in the case of samples with low Ni content. A slightly larger observed oxygen content values (or smaller amount of oxygen loss) in the case of samples with high Ni content could be due to the presence of a significant amount of Ni^{2+} ions in the lithium planes of the parent samples (before delithiation) due to a high degree of cation disorder as seen in Figure 5.3 and the consequent changes in the electronic environment and lithium and oxygen mobility.

Interestingly, despite the same transition metal ion content in the nominal compositions of the $(1-z)\ Li[Li_{1/3}Mn_{2/3}]O_2 \cdot (z)\ Li[Co_{1-y}Ni_y]O_2$ ($0 \le y \le 1$ and $z = 0.5$) samples, both the calculated and observed amounts of oxygen loss from the lattice in Table 5.2 decrease with increasing Ni content. This is due to a volatilization of lithium during the synthesis of the parent samples and a consequent increase in the transition metal ion to lithium ratio in the experimentally determined parent compositions as seen in Table 5.1. Additionally, the decrease in the amount of oxygen loss with increasing Ni content accounts for the decrease in the plateau region B (Figure 5.4) as well as the total first charge capacity and discharge capacity (Table 5.1). A decrease in the irreversible loss of oxygen during the first charge results in a lowering of the charge and discharge capacities.

5.3.2 (1-z) $Li[Li_{1/3}Mn_{2/3}]O_2 \cdot$ (z) $Li[Co_{1-y}Ni_y]O_2$ ($0 \le y \le 1$ and $z = 0.5$) series synthesized at 750 °C

5.3.2.1 Crystal chemistry

To investigate the effect of synthesis temperature, a second set of (1-z) $Li[Li_{1/3}Mn_{2/3}]O_2 \cdot$ (z) $Li[Co_{1-y}Ni_y]O_2$ ($0 \le y \le 1$ and $z = 0.5$) samples were also synthesized at 750 °C and characterized similar to the 900 °C samples. Figure 5.6 compares the XRD patterns of the samples synthesized at 750 °C for various values of y in (1-z) $Li[Li_{1/3}Mn_{2/3}]O_2 \cdot$ (z) $Li[Co_{1-y}Ni_y]O_2$ ($0 \le y \le 1$ and $z = 0.5$).

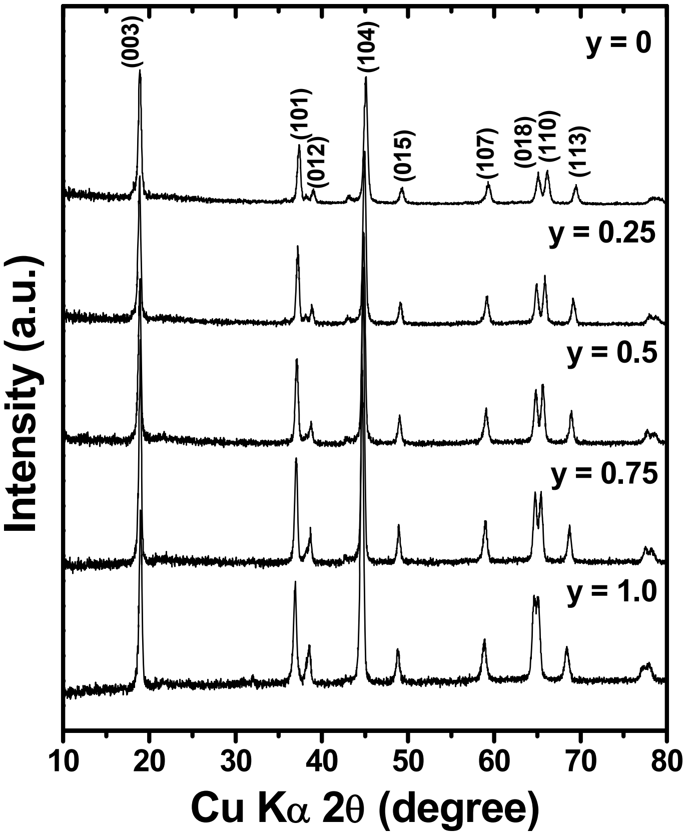

Figure 5.6: XRD patterns of (1-z) $Li[Li_{1/3}Mn_{2/3}]O_2 \cdot$ (z) $Li[Co_{1-y}Ni_y]O_2$ ($0 \le y \le 1$ and $z = 0.5$) samples synthesized at 750 °C.

All the samples were found to be single phase with the layered O3 type structure. However, similar to the 900 °C samples, the 750 °C samples exhibit a gradual decrease in the separation between the (018) and (110) reflections as the Ni content increases, suggesting an increase in the cation disorder between the lithium (3a sites) and transition metal (3b sites) planes. The 750 °C samples exhibited trends in the *a* and *c* parameters and cation disorder similar to the 900 °C samples (Figure 5.7). However, the observed lithium contents in the 750 °C samples were slightly higher than that in the 900 °C samples (Table 5.3) due to a suppression of the volatilization of lithium during synthesis.

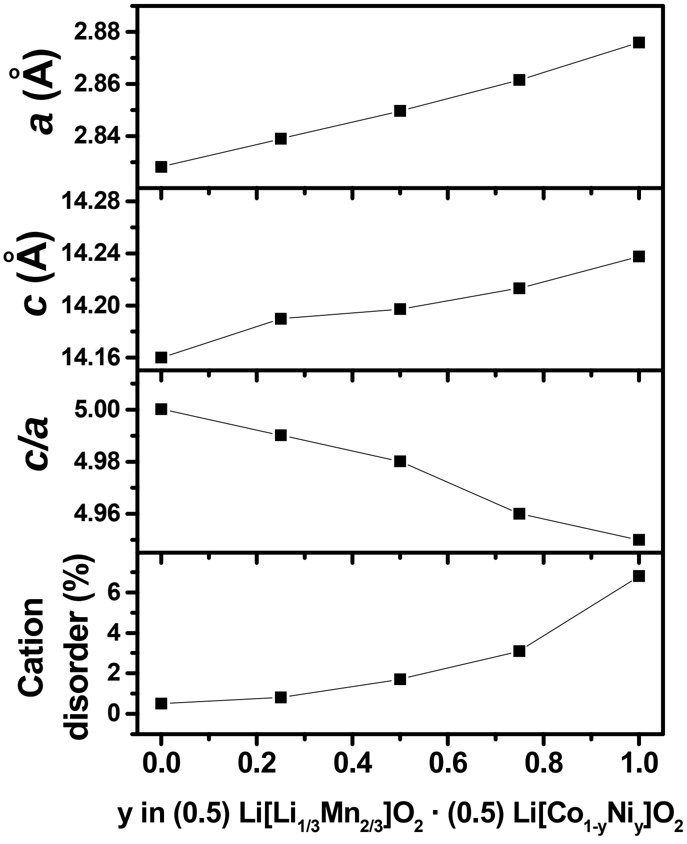

Figure 5.7: Variations of the lattice parameters *a* and *c*, *c/a* ratio, and cation disorder with y in (1-z) $Li[Li_{1/3}Mn_{2/3}]O_2 \cdot$ (z) $Li[Co_{1-y}Ni_y]O_2$ ($0 \leq y \leq 1$ and $z = 0.5$) samples synthesized at 750 °C.

Table 5.3: Observed chemical compositions and electrochemical data of (1-z) $Li[Li_{1/3}Mn_{2/3}]O_2 \cdot (z)\ Li[Co_{1-y}Ni_y]O_2$ ($0 \leq y \leq 1$ and $z = 0.5$) samples synthesized at 750 °C.

y	z	Nominal composition	Observed composition	M^{n+}	Observed 1st charge capacity[a] (mAh/g)			Theoretical 1st charge capacity in region A[b] (mAh/g)	First discharge capacity (mAh/g)
					Region A	Region B	Total (regions A+B)		
0	0.5	$Li[Li_{0.17}Mn_{0.33}Co_{0.5}]O_2$	$Li[Li_{0.17}Mn_{0.33}Co_{0.5}]O_2$	3.41	125	221	346	114	254
0.25		$Li[Li_{0.17}Mn_{0.33}Co_{0.375}Ni_{0.125}]O_2$	$Li[Li_{0.15}Mn_{0.34}Co_{0.38}Ni_{0.13}]O_2$	3.35	150	192	342	137	265
0.5		$Li[Li_{0.17}Mn_{0.33}Co_{0.25}Ni_{0.25}]O_2$	$Li[Li_{0.15}Mn_{0.35}Co_{0.25}Ni_{0.25}]O_2$	3.35	145	185	330	147	232
0.75		$Li[Li_{0.17}Mn_{0.33}Co_{0.125}Ni_{0.375}]O_2$	$Li[Li_{0.13}Mn_{0.35}Co_{0.13}Ni_{0.39}]O_2$	3.30	160	157	317	172	207
1		$Li[Li_{0.17}Mn_{0.33}Ni_{0.5}]O_2$	$Li[Li_{0.12}Mn_{0.35}Ni_{0.53}]O_2$	3.27	200	90	290	190	178

[a] Regions A and B correspond to, respectively, the initial sloping region A and the plateau region B as marked in Figure 5.8.
[b] Calculated assuming the oxidation of Mn, Ni, and Co, respectively, to Mn^{4+}, Ni^{4+}, and $Co^{3.75+}$.

5.3.2.2 Electrochemical performance

Figure 5.8 compares the first charge-discharge profiles of the 750 °C samples at 12.5 mA/g and 2.0 - 4.8 V. Table 5.3 compares the first charge and discharge capacities of the 750 °C samples. In general, the first total charge capacity and the first discharge capacity decrease with increasing Ni content similar to that found with the 900 °C samples. Also, while the initial sloping region A in the first charge profile increases, the plateau region B decreases with Ni content as in the 900 °C samples. However, the decrease in the first total charge capacity with increasing Ni content is smaller than that observed with the 900 °C samples. Also, the decrease in the plateau region B with increasing Ni content is smaller compared to that in the 900 °C sample; for example, a clear plateau region B could be observed for y = 1 in the 750 °C sample compared to that in the 900 °C sample. A larger plateau region B at a given Ni content in the 750 °C sample compared to that in the 900 °C sample is due to a higher amount of lithium ions in the transition metal layer (compare observed compositions in Tables 5.1 and 5.3) and a consequent loss of a larger amount of oxygen from the lattice during the first charge. In other words, the 750 °C samples will have a lower limiting oxygen content value compared to that in Table 5.2 for the 900 °C sample.

Table 5.3 also gives the theoretical value of the first charge capacity in region A, calculated based on the oxidation of the transition metal ions to Mn^{4+}, Ni^{4+}, and $Co^{3.75+}$. A close agreement between this theoretical value and the charge capacity in the sloping region A suggests that it may be difficult to oxidize Co beyond 3.75+ without oxidizing the oxide ions in the 750 °C sample. This cutoff oxidation state value of 3.75+ for Co in the 750 °C sample is slightly higher than the value of 3.6+ in the 900 °C sample (Table 5.1). This difference could be due to a narrowing of the $Co^{3+/4+}$:3d band in the 750 °C sample resulting from a lower crystallinity compared to that in the 900 °C sample and a consequent decrease in the overlap of the $Co^{3+/4+}$:3d band with the top of the O^{2-}:2p band.[143]

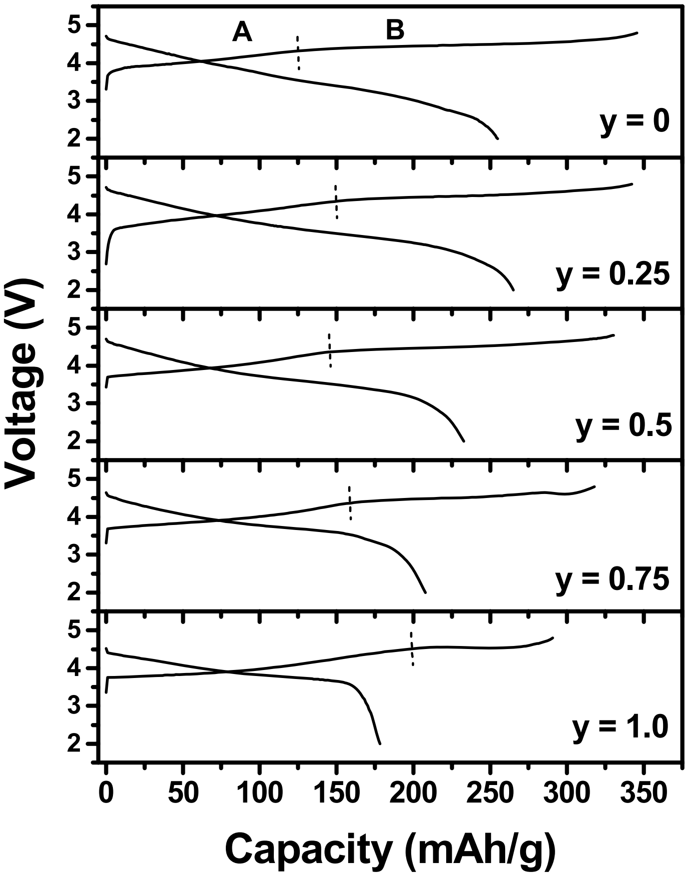

Figure 5.8: Comparison of the first charge-discharge profiles (recorded at 12.5 mA/g between 2.0 - 4.8 V) of the (1-z) $Li[Li_{1/3}Mn_{2/3}]O_2 \cdot$ (z) $Li[Co_{1-y}Ni_y]O_2$ ($0 \leq y \leq 1$ and z = 0.5) samples synthesized at 750 °C. The dashed vertical lines separate the initial sloping region A from the plateau region B.

Figure 5.9 compares the cyclability of the samples synthesized at 750 °C at 12.5 mA/g between 2.0 - 4.8 V. The samples generally show cycling behaviors similar to the 900 °C samples excepting $Li[Li_{0.17}Mn_{0.33}Co_{0.5}]O_2$, which exhibits a faster decline in capacity. Figure 5.10 compares the XRD patterns of the 750 °C cathodes after 20 cycles.

While the rest of the cathodes maintain good crystallinity, the $Li[Li_{0.17}Mn_{0.33}Co_{0.5}]O_2$ cathode suffers from a significant line broadening and loss of crystallinity on cycling. $LiCoO_2$ synthesized at low temperatures (400 °C) is known to adopt a lithiated spinel structure instead of the O3 layer structure and exhibit poor electrochemical properties.[144,145] Thus, a possible structural disorder in the Co-rich sample (y = 0) synthesized at 750 °C may cause a loss of crystallinity and a rapid capacity fade on cycling.

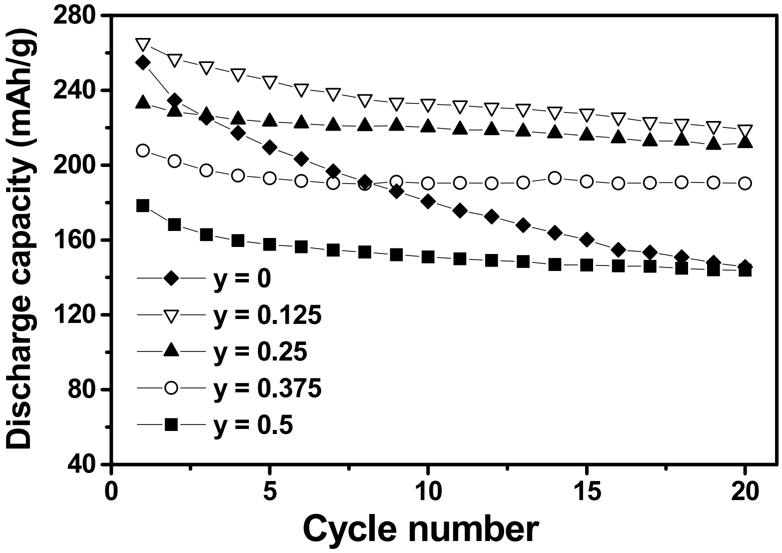

Figure 5.9: Comparison of the cyclability data (12.5 mA/g between 2.0 – 4.8 V) of the (1-z) $Li[Li_{1/3}Mn_{2/3}]O_2 \cdot$ (z) $Li[Co_{1-y}Ni_y]O_2$ ($0 \leq y \leq 1$ and z = 0.5) samples synthesized at 750 °C.

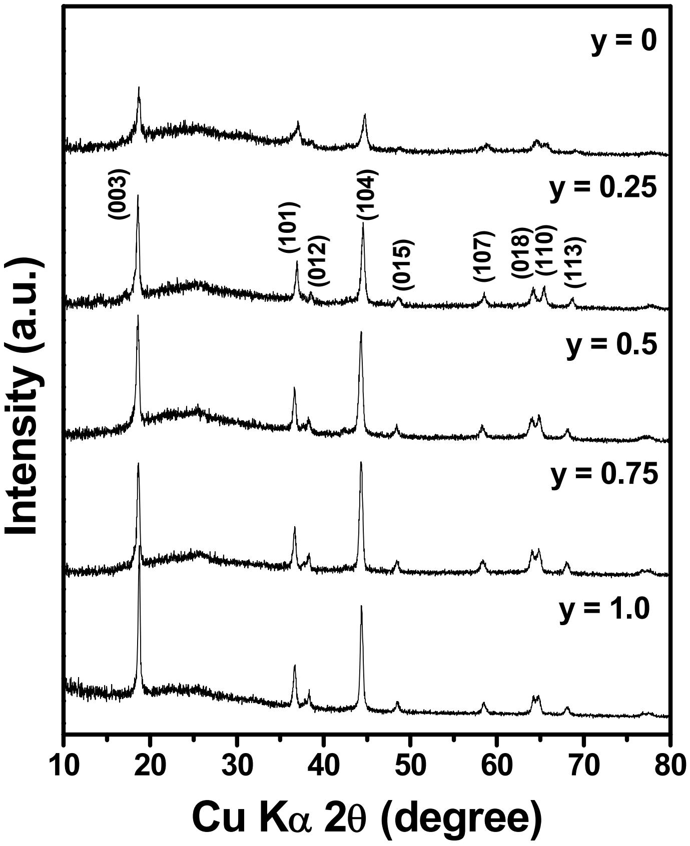

Figure 5.10: XRD patterns of (1-z) $Li[Li_{1/3}Mn_{2/3}]O_2 \cdot$ (z) $Li[Co_{1-y}Ni_y]O_2$ ($0 \leq y \leq 1$ and $z = 0.5$; synthesized at 750 °C) cathodes after 20 cycles.

5.3.3 (1-z) $Li[Li_{1/3}Mn_{2/3}]O_2$ · (z) $Li[Co_{1-y}Ni_y]O_2$ ($0 \leq y \leq 1$ and $z = 0.7$) series synthesized at 900 °C

5.3.3.1 Crystal chemistry

The compositions studied in the (1-z) $Li[Li_{1/3}Mn_{2/3}]O_2$ · (z) $Li[Co_{1-y}Ni_y]O_2$ ($0 \leq y \leq 1$ and $z = 0.7$) solid solution series are indicated by closed circles in Figure 5.11. While the $Li[Li_{1/3}Mn_{2/3}]O_2$ to $LiCo_{1-y}Ni_yO_2$ ratio in the solid solution is kept at 3:7 (30 mol % $Li[Li_{1/3}Mn_{2/3}]O_2$ and 70 mol % $LiCo_{1-y}Ni_yO_2$), the Ni content y in $LiCo_{1-y}Ni_yO_2$ is varied from 0 to 1.

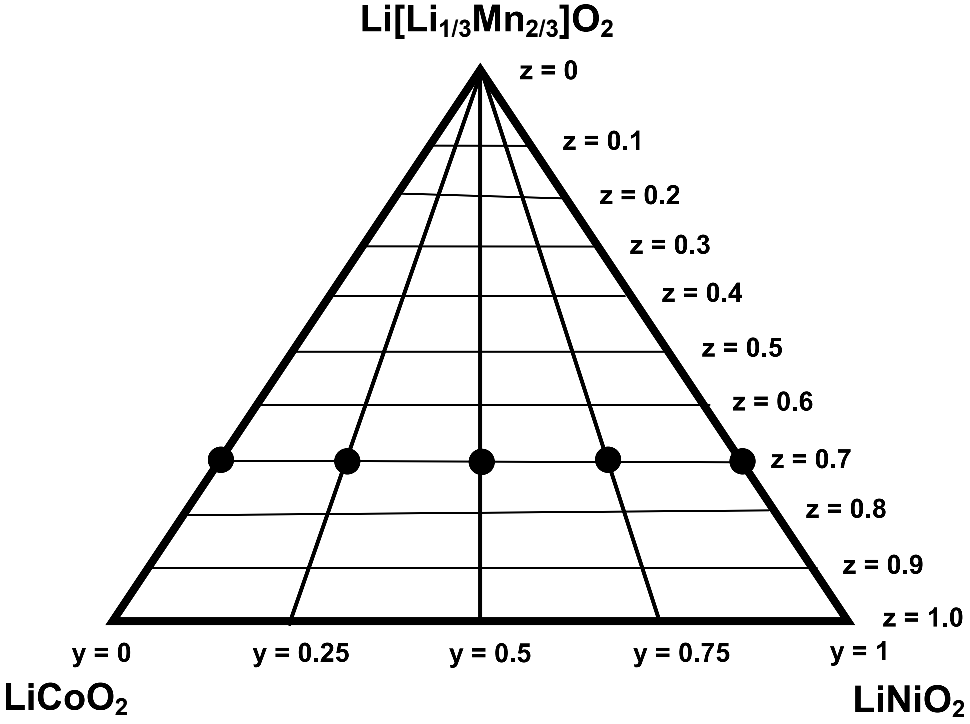

Figure 5.11: Phase diagram of the $Li[Li_{1/3}Mn_{2/3}]O_2$ - $LiCoO_2$ - $LiNiO_2$ system. The compositions studied in the (1-z) $Li[Li_{1/3}Mn_{2/3}]O_2$ · (z) $Li[Co_{1-y}Ni_y]O_2$ ($0 \leq y \leq 1$ and $z = 0.7$) system are indicated by closed circles.

Table 5.4: Observed chemical compositions of the parent and chemically delithiated (1-z) $Li[Li_{1/3}Mn_{2/3}]O_2 \cdot$ (z) $Li[Co_{1-y}Ni_y]O_2$ ($0 \leq y \leq 1$ and $z = 0.7$) samples synthesized at 900 °C.

y	z	Nominal composition	Observed composition	Observed composition after chemical delithiation[a]	M^{n+}	Calculated limiting oxygen content (2-δ)[b]
0	0.7	$Li[Li_{0.1}Mn_{0.2}Co_{0.7}]O_2$	$Li[Li_{0.1}Mn_{0.2}Co_{0.7}]O_2$	$Li_{0.07}H_{0.24}[Li_{0.1}Mn_{0.2}Co_{0.7}]O_{1.78}$	3.50	1.80
0.25		$Li[Li_{0.1}Mn_{0.2}Co_{0.525}Ni_{0.175}]O_2$	$Li[Li_{0.08}Mn_{0.2}Co_{0.54}Ni_{0.18}]O_2$	$Li_{0.04}H_{0.38}[Li_{0.08}Mn_{0.2}Co_{0.54}Ni_{0.18}]O_{1.86}$	3.50	1.84
0.5		$Li[Li_{0.1}Mn_{0.2}Co_{0.35}Ni_{0.35}]O_2$	$Li[Li_{0.05}Mn_{0.21}Co_{0.37}Ni_{0.37}]O_2$	$Li_{0.02}H_{0.43}[Li_{0.05}Mn_{0.21}Co_{0.37}Ni_{0.37}]O_{1.90}$	3.47	1.90
0.75		$Li[Li_{0.1}Mn_{0.2}Co_{0.175}Ni_{0.525}]O_2$	$Li[Li_{0.02}Mn_{0.22}Co_{0.19}Ni_{0.57}]O_2$	$Li_{0.12}H_{0.14}[Li_{0.02}Mn_{0.22}Co_{0.19}Ni_{0.57}]O_{1.96}$	3.72	1.96
1.0		$Li[Li_{0.1}Mn_{0.2}Ni_{0.7}]O_2$	$Li_{0.96}Ni_{0.04}[Mn_{0.23}Ni_{0.77}]O_{1.97}$	$Li_{0.47}Ni_{0.04}[Mn_{0.23}Ni_{0.77}]O_{1.97}$	3.33	2.00

[a] Determined based on the experimentally observed lithium and proton contents and oxidation state values.
[b] Calculated based on the maximum amount of oxygen the sample could lose (see text).

Table 5.4 gives the nominal compositions and the observed compositions of the z = 0.7 samples synthesized at 900 ^{o}C. The data show a decrease in the observed lithium content with increasing Ni content y, similar to that discussed for the z = 0.5 solid solution series in section 5.3.1.1.

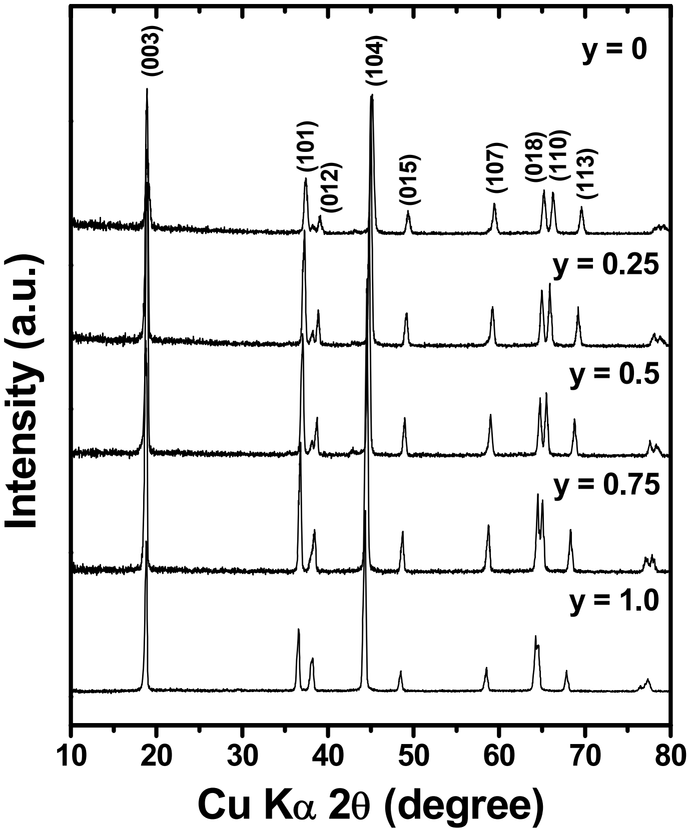

Figure 5.12: XRD patterns of (1-z) $Li[Li_{1/3}Mn_{2/3}]O_2 \cdot$ (z) $Li[Co_{1-y}Ni_y]O_2$ ($0 \leq y \leq 1$ and z = 0.7) samples synthesized at 900 ^{o}C.

Figure 5.12 compares the XRD patterns of the samples synthesized at 900 ^{o}C for various values of y in (1-z) $Li[Li_{1/3}Mn_{2/3}]O_2 \cdot$ (z) $Li[Co_{1-y}Ni_y]O_2$ ($0 \leq y \leq 1$ and z = 0.7). Similar to the z = 0.5 series of samples, the z = 0.7 samples were found to be single phase, crystallizing in the layered O3 type structure and the separation between the (018) and (110) reflections decrease gradually as the Ni content increases.

The z = 0.7 series of samples exhibit trends in the *a* and *c* parameters and cation disorder (Figure 5.13) similar to the z = 0.5 series of samples synthesized at 900 °C (Figure 5.3). However, the extent of variations in the lattice parameters of the z = 0.7 samples are found to be higher than that found in the z = 0.5 series of samples due to a relatively higher Ni content.

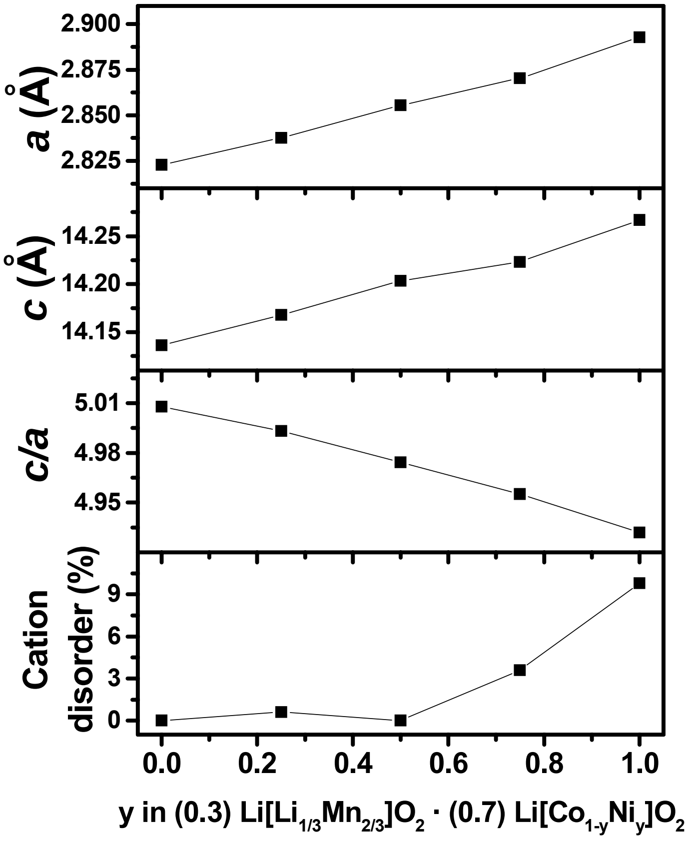

Figure 5.13: Variations of the lattice parameters *a* and *c*, *c/a* ratio, and cation disorder (fraction of lithium sites occupied by transition metal ions in the lithium layer) with y in (1-z) $Li[Li_{1/3}Mn_{2/3}]O_2 \cdot$ (z) $Li[Co_{1-y}Ni_y]O_2$ ($0 \leq y \leq 1$ and z = 0.7) samples synthesized at 900 °C.

5.3.3.2 Chemical stability of delithiated samples

With an aim to understand the factors that influence the irreversible oxygen loss from the solid solution samples, we performed chemical characterizations on bulk samples obtained by chemically extracting lithium from layered (1-z) $Li[Li_{1/3}Mn_{2/3}]O_2 \cdot$ (z) $Li[Co_{1-y}Ni_y]O_2$ ($0 \leq y \leq 1$ and $z = 0.7$) samples synthesized at 900 °C with the oxidizer NO_2BF_4 in acetonitrile medium. Table 5.4 gives the compositions of the delithiated samples containing some residual lithium and inserted protons in the lithium plane. As with the z = 0.5 series of samples discussed in section 5.3.1.3, the decrease in the amount of oxygen lost during chemical delithiation with increasing Ni content for the z = 0.7 series could be explained by considering the experimentally determined chemical compositions for the parent samples and using the mechanism proposed by Armstrong *et al*.[134] The calculated limiting oxygen content values based on the above mechanism agree closely with the observed oxygen content values in the delithiated samples and they both decrease with increasing Ni content and thus the results obtained with the z = 0.7 solid solution series complement the oxygen loss behavior of the z = 0.5 solid solution series.

5.3.4 (1-z) $Li[Li_{1/3}Mn_{2/3}]O_2 \cdot$ (z) $Li[Co_{1-y}Ni_y]O_2$ (y = 0.5 and $0.2 \leq z \leq 0.7$) series synthesized at 900 °C

5.3.4.1 Crystal chemistry

The compositions studied in the (1-z) $Li[Li_{1/3}Mn_{2/3}]O_2 \cdot$ (z) $Li[Co_{1-y}Ni_y]O_2$ (y = 0.5 and $0.2 \leq z \leq 0.7$) solid solution series are indicated by closed circles in Figure 5.14. While the Ni to Co ratio is kept at 1:1, the proportion of $LiCo_{0.5}Ni_{0.5}O_2$ to $Li[Li_{1/3}Mn_{2/3}]O_2$ (z value) is varied in this series.

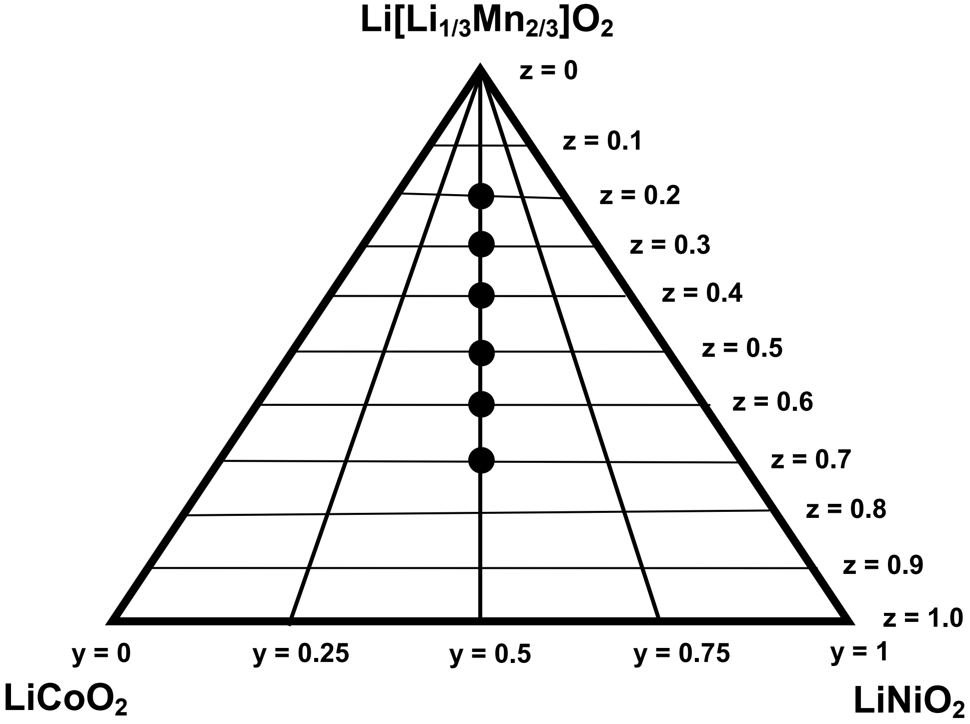

Figure 5.14: Phase diagram of the $Li[Li_{1/3}Mn_{2/3}]O_2$ - $LiCoO_2$ - $LiNiO_2$ system. The compositions studied in the (1-z) $Li[Li_{1/3}Mn_{2/3}]O_2 \cdot$ (z) $Li[Co_{1-y}Ni_y]O_2$ (y = 0.5 and $0.2 \leq z \leq 0.7$) system are indicated by closed circles.

X-ray diffraction data (Figure 5.15) indicated all the samples to be single phase materials belonging to the α-$NaFeO_2$ layered structure (O3 structure). However, in addition to the reflections corresponding to the O3 layered structure, weak superstructure reflections were observed around $2\theta = 20 - 25^{o}$ for samples with high $Li[Li_{1/3}Mn_{2/3}]O_2$ content, which are known to correspond to the ordering of the Li^{+}, Ni^{2+}, and Mn^{4+} ions in the transition metal layer of the layered lattice.[146,147] The superstructure reflections vanish for $z > 0.5$ as seen in the expanded region on the right in Figure 5.15.

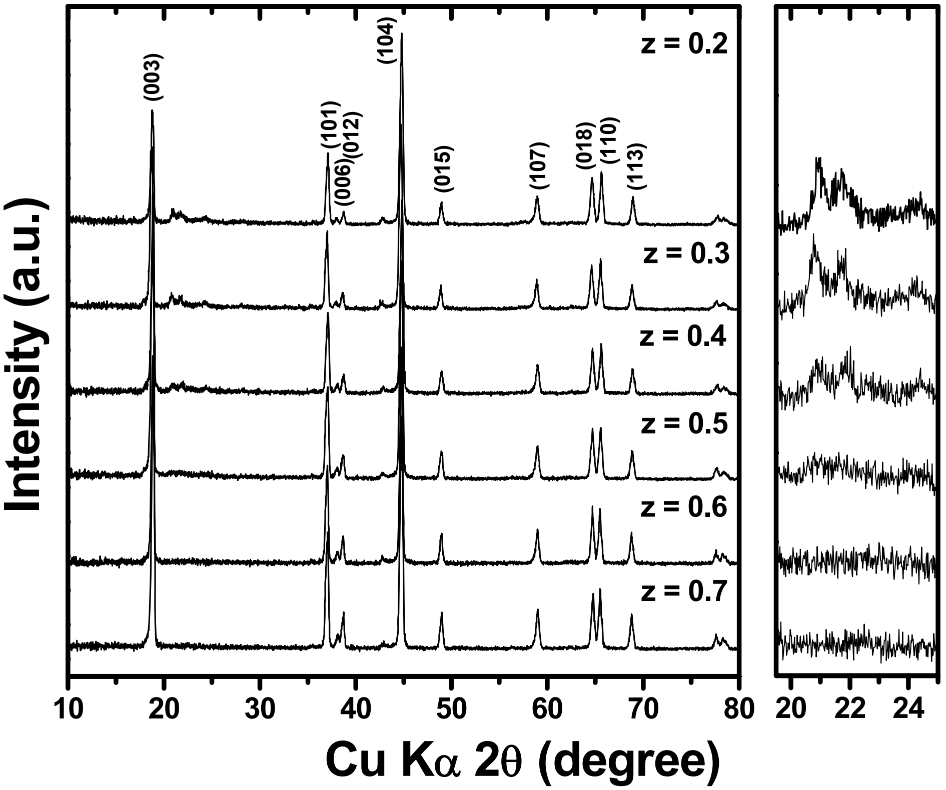

Figure 5.15: XRD patterns of the (1-z) $Li[Li_{1/3}Mn_{2/3}]O_2 \cdot (z)\ Li[Co_{1-y}Ni_y]O_2$ ($y = 0.5$ and $0.2 \leq z \leq 0.7$) samples synthesized at 900 °C. The expanded region on the right shows the superstructure reflections arising from an ordering among Li^{+}, Mn^{4+}, and Ni^{2+}.

Figure 5.16 shows the variations of the unit cell parameters of the y = 0.5 series of samples with z in (1-z) $Li[Li_{1/3}Mn_{2/3}]O_2 \cdot$ (z) $Li[Co_{1-y}Ni_y]O_2$. The *a* parameter and the unit cell volume increase with the z value while the *c* parameter and the *c/a* ratio decrease, illustrating the formation of solid solutions.

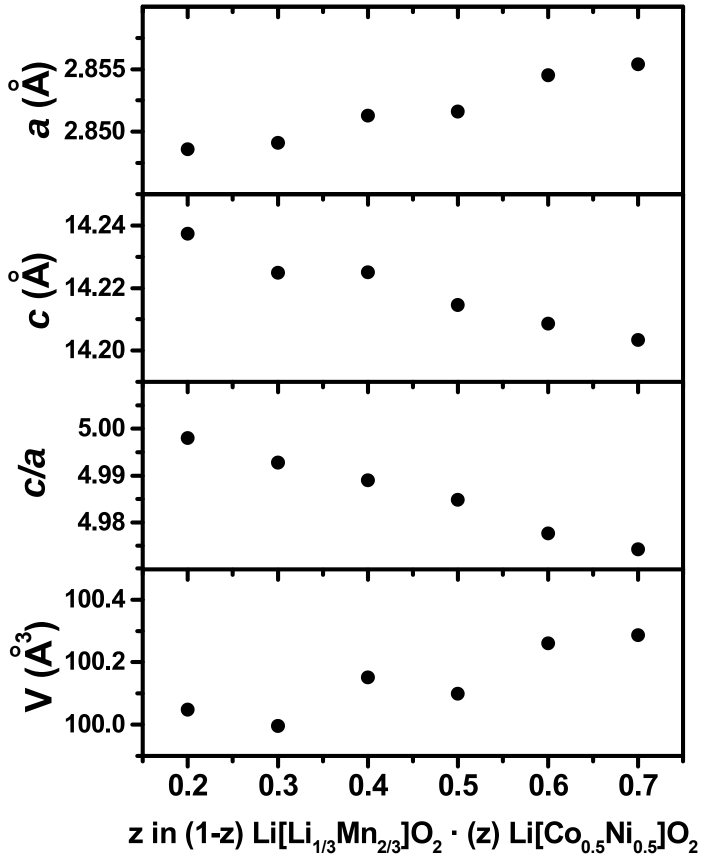

Figure 5.16: Variations of the unit cell parameters with z in the (1-z) $Li[Li_{1/3}Mn_{2/3}]O_2 \cdot$ (z) $Li[Co_{1-y}Ni_y]O_2$ (y = 0.5 and $0.2 \leq z \leq 0.7$) samples synthesized at 900 °C.

Table 5.5: Observed chemical compositions and electrochemical data of (1-z) $Li[Li_{1/3}Mn_{2/3}]O_2 \cdot (z) Li[Co_{1-y}Ni_y]O_2$ ($y = 0.5$ and $0.2 \leq z \leq 0.7$) samples synthesized at 900 °C.

y	z	Nominal composition	Observed composition	M^{n+}	Observed 1st charge capacity[a] (mAh/g)			Theoretical 1st charge capacity in region A[b] (mAh/g)	First discharge capacity (mAh/g)
					Region A	Region B	Total (regions A+B)		
0.5	0.2	$Li[Li_{0.27}Mn_{0.53}Co_{0.1}Ni_{0.1}]O_2$	$Li[Li_{0.27}Mn_{0.53}Co_{0.1}Ni_{0.1}]O_2$	3.74	65	188	253	53	168
	0.3	$Li[Li_{0.23}Mn_{0.47}Co_{0.15}Ni_{0.15}]O_2$	$Li[Li_{0.21}Mn_{0.48}Co_{0.155}Ni_{0.155}]O_2$	3.53	110	200	310	97	205
	0.4	$Li[Li_{0.2}Mn_{0.4}Co_{0.2}Ni_{0.2}]O_2$	$Li[Li_{0.16}Mn_{0.42}Co_{0.21}Ni_{0.21}]O_2$	3.38	130	189	319	133	200
	0.5	$Li[Li_{0.17}Mn_{0.33}Co_{0.25}Ni_{0.25}]O_2$	$Li[Li_{0.12}Mn_{0.36}Co_{0.26}Ni_{0.26}]O_2$	3.27	150	155	305	159	205
	0.6	$Li[Li_{0.13}Mn_{0.26}Co_{0.3}Ni_{0.3}]O_2$	$Li[Li_{0.08}Mn_{0.28}Co_{0.32}Ni_{0.32}]O_2$	3.17	180	113	293	183	208
	0.7	$Li[Li_{0.1}Mn_{0.2}Co_{0.35}Ni_{0.35}]O_2$	$Li[Li_{0.05}Mn_{0.21}Co_{0.37}Ni_{0.37}]O_2$	3.11	215	57	272	200	220

[a] Regions A and B correspond to, respectively, the initial sloping region A and the plateau region B as marked in Figure 5.17.

[b] Calculated assuming the oxidation of Mn, Ni, and Co, respectively, to Mn^{4+}, Ni^{4+}, and $Co^{3.6+}$.

Chemical analysis indicated the lithium content in the synthesized samples to be lower than that in the nominal compositions for the y = 0.5 series of samples. The oxidation state analysis by the redox titration indicated the nickel oxidation state to be lower (2.52+ to 2.70+) than the expected value of 3+ assuming Li^+, Mn^{4+} and Co^{3+}. Thus, the lower lithium content in the samples is due to a reduction of Ni^{3+} to Ni^{2+} and the consequent volatilization of lithium during synthesis at elevated temperatures (900 °C). The observed compositions based on the experimentally determined lithium content and the average oxidation state of the transition metal ions are given in Table 5.5. For example, while the nominal composition for the y = 0.5 and z = 0.7 sample is $Li[Li_{0.1}Mn_{0.2}Co_{0.35}Ni_{0.35}]O_2$, the observed composition is $Li[Li_{0.05}Mn_{0.21}Ni_{0.37}Co_{0.37}]O_2$ with a loss of small amount of lithium while maintaining the ratio among the transition metal ions as in the nominal composition.

5.3.4.2 Electrochemical performance

Figure 5.17 compares the first charge-discharge profiles of the (1-z) $Li[Li_{1/3}Mn_{2/3}]O_2 \cdot (z)\ Li[Co_{1-y}Ni_y]O_2$ ($y = 0.5$ and $0.2 \leq z \leq 0.7$) solid solution samples synthesized at 900 °C. The dashed vertical lines separate the initial sloping region A from the plateau region B in Figure 5.17. Table 5.5 compares the first charge capacity values in the two regions A and B and the first discharge capacity for all the samples. The initial sloping region A increases with increasing z in Table 5.5 (or decreasing lithium content in the transition metal layer) due to an increase in $Ni^{2+/3+}$ and Co^{3+} contents (or a decrease in the average oxidation state of transition metal ions) and their oxidation during first charge, while the plateau region B decreases with increasing z in Table 5.5 (or decreasing lithium content in the transition metal layer) excepting for the z = 0.2 sample. A good agreement between the observed and calculated charge capacities in the sloping region A confirms the oxygen evolution from the lattice for oxidations beyond approximately $Co^{3.6+}$ for the samples synthesized at 900 °C.

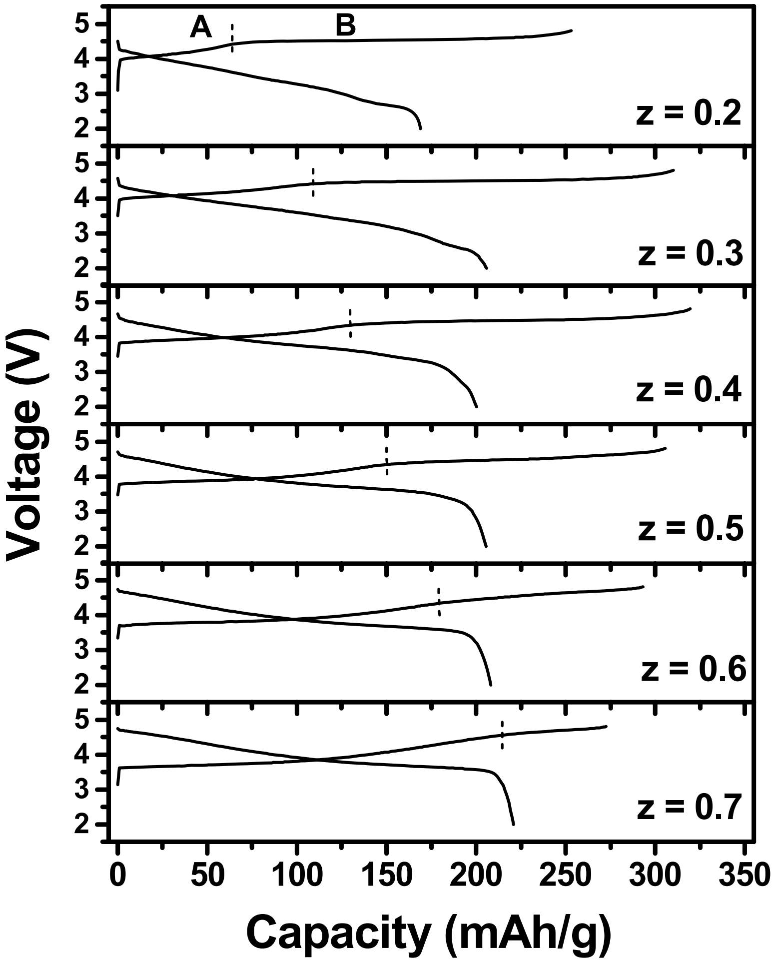

Figure 5.17: Comparison of the first charge-discharge profiles (recorded at 12.5 mA/g between 2.0 – 4.8 V) of the (1-z) $Li[Li_{1/3}Mn_{2/3}]O_2 \cdot$ (z) $Li[Co_{1-y}Ni_y]O_2$ (y = 0.5 and $0.2 \leq z \leq 0.7$) samples synthesized at 900 °C. The dashed vertical lines separate the initial sloping region A from the plateau region B.

Figure 5.18 compares the cyclability of the samples synthesized at 900 °C for various z values at 12.5 mA/g between 2.0 - 4.8 V. The samples with an intermediate z value of around 0.4 shows better cyclability. The samples with higher Co contents (z =

0.6, 0.7) show poor cyclability due to the chemical instabilities that could occur at deep charge (high charge voltages),[24] while the sample with z = 0.2 shows lower discharge capacity values due to the presence of a significant amount of electrochemically inactive Mn^{4+} ions.

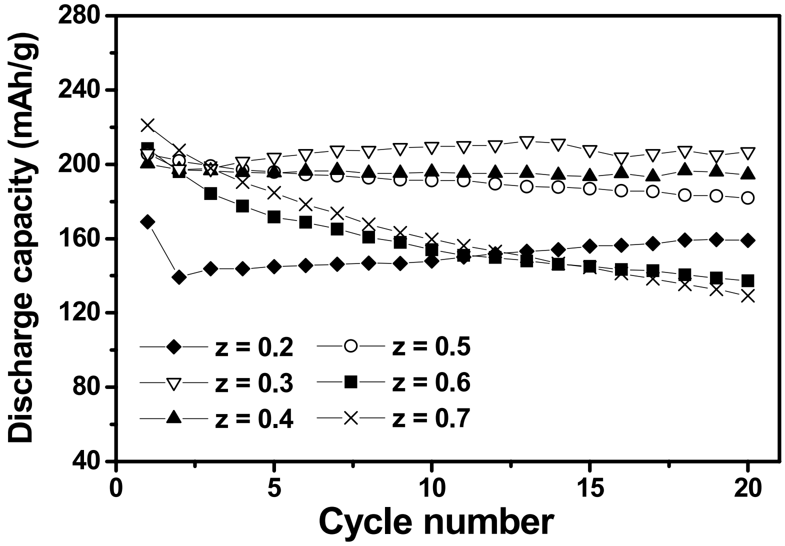

Figure 5.18: Comparison of the cyclability data (12.5 mA/g between 2.0 – 4.8 V) of the (1-z) $Li[Li_{1/3}Mn_{2/3}]O_2 \cdot (z)\ Li[Co_{1-y}Ni_y]O_2$ (y = 0.5 and $0.2 \leq z \leq 0.7$) samples synthesized at 900 °C.

5.3.4.3 Chemical stability of delithiated samples

To gain an understanding of the factors that control the reversible capacity values, we performed chemical characterizations on bulk samples obtained by chemically extracting lithium from layered (1-z) $Li[Li_{1/3}Mn_{2/3}]O_2 \cdot (z)\ Li[Co_{1-y}Ni_y]O_2$ (y = 0.5 and $0.2 \leq z \leq 0.7$) samples synthesized at 900 °C with the oxidizer NO_2BF_4 in acetonitrile medium. Table 5.6 gives the compositions of the delithiated samples containing some residual lithium and inserted protons in the lithium plane. The amount of residual lithium was found to increase, while the inserted proton content decreases with decreasing z value. The increase in the residual lithium with decreasing z values is due to an increasing amount of electrochemically inactive Mn^{4+} ions in the parent sample that decrease the electronic and ionic conductivity of the sample. Consequently, the presence of residual lithium in the lithium plane hinders the insertion of proton into the layered compounds.

Table 5.6 gives the limiting oxygen content values calculated based on the mechanism proposed by Armstrong *et al*,[134] as well as the observed chemical compositions after the cation rearrangement (obtained by normalizing the oxygen content to 2.0). The calculated limiting oxygen content values agree closely with the observed oxygen content values in the delithiated samples for $z \geq 0.5$ (see the formula before cation rearrangement). For samples with $z < 0.5$, the observed oxygen content values in the delithiated samples were found to be higher than the calculated limiting oxygen content values and the difference increases with decreasing z value. A larger observed oxygen content values (or smaller amount of oxygen loss) in the case of samples with low z value could be due to the presence of a significant amount of electrochemically inactive Mn^{4+} ions in the parent samples (before delithiation) and the consequent decrease in the oxygen mobility to leave the lattice. Thus, a smaller plateau region B and a lower total charge and discharge capacities than that expected for the samples with low z values (Table 5.5) are due to an increasing amount of electrochemically inactive Mn^{4+} ion in the lattice. An interplay between the relative changes in the regions A and B makes the variations in the discharge capacity with z less significant.

Table 5.6: Chemical analysis data of chemically delithiated (1-z) $Li[Li_{1/3}Mn_{2/3}]O_2 \cdot (z) Li[Co_{1-y}Ni_y]O_2$ (y = 0.5 and 0.2 ≤ z ≤ 0.7) samples synthesized at 900 °C.

y	z	Observed parent composition	Observed composition after chemical delithiation[a]		M^{n+}	Calculated limiting oxygen content (2-δ)[b]
			Before rearrangement	After rearrangement		
0.5	0.2	$Li[Li_{0.27}Mn_{0.53}Co_{0.1}Ni_{0.1}]O_2$	$Li_{0.33}H_{0.03}[Li_{0.27}Mn_{0.53}Co_{0.1}Ni_{0.1}]O_{1.72}$	$Li_{0.55}H_{0.03}[Li_{0.15}Mn_{0.61}Co_{0.12}Ni_{0.12}]O_2$	3.85	1.46
	0.3	$Li[Li_{0.21}Mn_{0.48}Co_{0.155}Ni_{0.155}]O_2$	$Li_{0.19}H_{0.09}[Li_{0.21}Mn_{0.48}Co_{0.155}Ni_{0.155}]O_{1.70}$	$Li_{0.40}H_{0.11}[Li_{0.07}Mn_{0.57}Co_{0.18}Ni_{0.18}]O_2$	3.68	1.58
	0.4	$Li[Li_{0.16}Mn_{0.42}Co_{0.21}Ni_{0.21}]O_2$	$Li_{0.04}H_{0.12}[Li_{0.16}Mn_{0.42}Co_{0.21}Ni_{0.21}]O_{1.73}$	$Li_{0.20}H_{0.14}[Li_{0.03}Mn_{0.49}Co_{0.24}Ni_{0.24}]O_2$	3.73	1.68
	0.5	$Li[Li_{0.12}Mn_{0.36}Co_{0.26}Ni_{0.26}]O_2$	$Li_{0.05}H_{0.18}[Li_{0.12}Mn_{0.36}Co_{0.26}Ni_{0.26}]O_{1.78}$	$Li_{0.18}H_{0.20}[Li_{0.01}Mn_{0.41}Co_{0.29}Ni_{0.29}]O_2$	3.65	1.76
	0.6	$Li[Li_{0.08}Mn_{0.28}Co_{0.32}Ni_{0.32}]O_2$	$Li_{0.08}H_{0.26}[Li_{0.08}Mn_{0.28}Co_{0.32}Ni_{0.32}]O_{1.86}$	$Li_{0.16}H_{0.28}[Li_{0.01}Mn_{0.31}Co_{0.34}Ni_{0.34}]O_2$	3.58	1.84
	0.7	$Li[Li_{0.05}Mn_{0.21}Co_{0.37}Ni_{0.37}]O_2$	$Li_{0.02}H_{0.43}[Li_{0.05}Mn_{0.21}Co_{0.37}Ni_{0.37}]O_{1.90}$	$Li_{0.08}H_{0.45}[Mn_{0.22}Co_{0.39}Ni_{0.39}]O_2$	3.47	1.90

[a] Determined based on the experimentally observed lithium and proton contents and oxidation state values.
[b] Calculated based on the maximum amount of oxygen the sample could lose (see text).

5.3.5 (1-z) $Li[Li_{1/3}Mn_{2/3}]O_2 \cdot$ (z) $Li[Co_{1-y}Ni_y]O_2$ (y = 0.5 and $0.2 \leq z \leq 0.7$) series synthesized at 750 °C

5.3.5.1 Crystal chemistry

To investigate the effect of synthesis temperature, a second set of (1-z) $Li[Li_{1/3}Mn_{2/3}]O_2 \cdot$ (z) $Li[Co_{1-y}Ni_y]O_2$ (y = 0.5 and $0.2 \leq z \leq 0.7$) samples were also synthesized at 750 °C and characterized similar to the 900 °C samples.

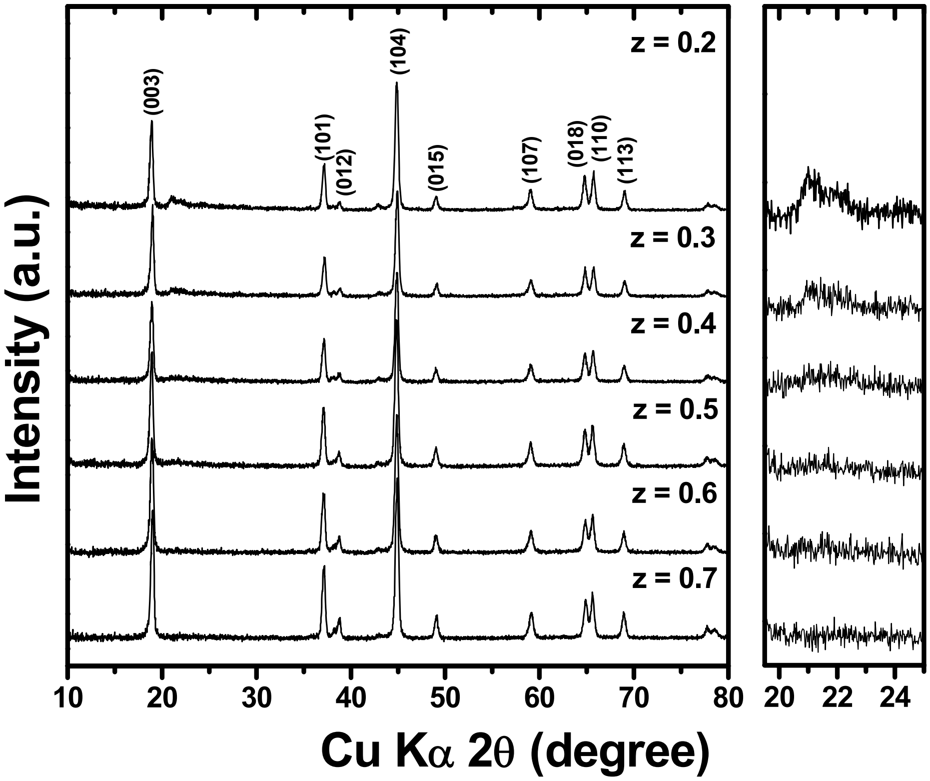

Figure 5.19: XRD patterns of the (1-z) $Li[Li_{1/3}Mn_{2/3}]O_2 \cdot$ (z) $Li[Co_{1-y}Ni_y]O_2$ (y = 0.5 and $0.2 \leq z \leq 0.7$) samples synthesized at 750 °C. The expanded region on the right shows the superstructure reflections arising from an ordering among Li^+, Mn^{4+}, and Ni^{2+}.

Figure 5.19 compares the XRD patterns of the samples synthesized at 750 °C for various values of z in (1-z) $Li[Li_{1/3}Mn_{2/3}]O_2 \cdot$ (z) $Li[Co_{1-y}Ni_y]O_2$ (y = 0.5 and $0.2 \leq z \leq 0.7$). All the samples were found to be single phase with the layered O3 type structure. However, similar to the 900 °C samples, weak superstructure reflections were observed around $2\theta = 20 - 25^\circ$ for samples with high $Li[Li_{1/3}Mn_{2/3}]O_2$ content, which are known to correspond to the ordering of the Li^+, Ni^{2+}, and Mn^{4+} ions in the transition metal layer of the layered lattice.[146,147] The superstructure reflections vanish for z > 0.4 as seen in the expanded region on the right in Figure 5.19.

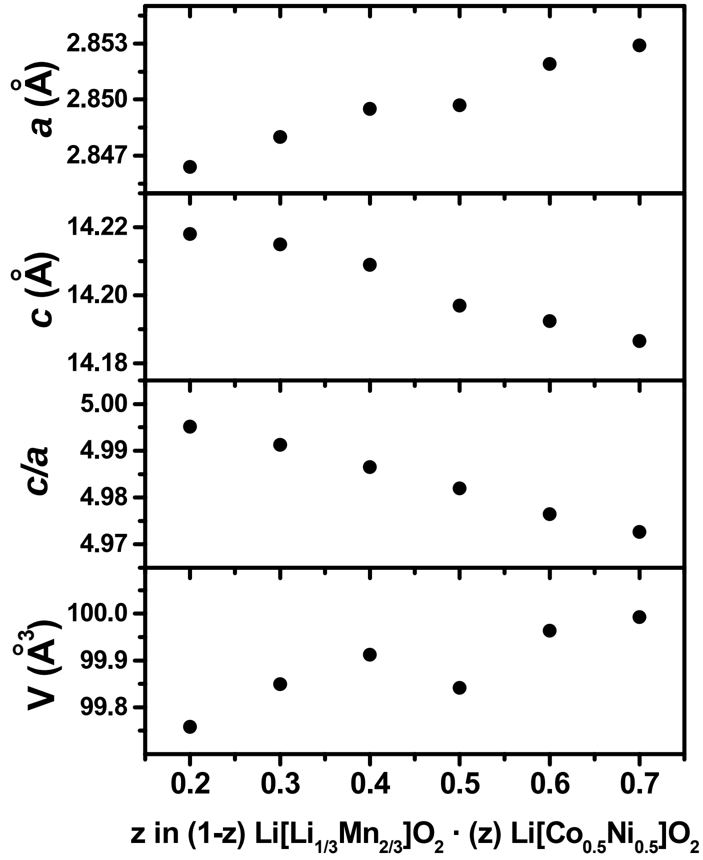

Figure 5.20: Variations of the unit cell parameters with z in the (1-z) $Li[Li_{1/3}Mn_{2/3}]O_2 \cdot$ (z) $Li[Co_{1-y}Ni_y]O_2$ (y = 0.5 and $0.2 \leq z \leq 0.7$) samples synthesized at 750 °C.

Figure 5.20 shows the variations of the unit cell parameters of the y = 0.5 series of samples synthesized at 750 °C with z in (1-z) $Li[Li_{1/3}Mn_{2/3}]O_2 \cdot (z) Li[Co_{1-y}Ni_y]O_2$. The 750 °C samples exhibited trends in the unit cell parameters similar to the 900 °C samples. The *a* parameter and the unit cell volume increase with the z value while the *c* parameter and the *c/a* ratio decrease, illustrating the formation of solid solutions.

Chemical analysis indicated the lithium content in the synthesized samples to be lower than that in the nominal compositions for the y = 0.5 series of samples synthesized at 750 °C. The lower lithium content in the samples is due to a reduction of Ni^{3+} to Ni^{2+} and the consequent volatilization of lithium during synthesis at elevated temperatures, as explained for the 900 °C samples. However, the observed lithium contents in the 750 °C samples were slightly higher than that in the 900 °C samples due to a reduced volatilization of lithium during synthesis. The observed compositions based on the experimentally determined lithium content and the average oxidation state of the transition metal ions are given in Table 5.7.

5.3.5.2 Electrochemical performance

Figure 5.21 compares the first charge-discharge profiles of the 750 °C samples at 12.5 mA/g and 2.0 - 4.8 V. Table 5.7 compares the first charge capacity values in regions A and B and the first discharge capacity for all the samples. Except at a high $Li[Li_{1/3}Mn_{2/3}]O_2$ content or low z value (0.2), the first total charge capacity (regions A + B) and the discharge capacity decrease with increasing z value similar to that found with the 900 °C samples. Also, while the first charge capacity in the initial sloping region A increases, the plateau region B decreases with increasing z value as in the 900 °C samples.

Table 5.7: Observed chemical compositions and electrochemical data of (1-z) $Li[Li_{1/3}Mn_{2/3}]O_2 \cdot$ (z) $Li[Co_{1-y}Ni_y]O_2$ (y = 0.5 and $0.2 \leq z \leq 0.7$) samples synthesized at 750 °C.

y	z	Nominal composition	Observed composition	M^{n+}	Observed 1st charge capacity[a] (mAh/g)			Theoretical 1st charge capacity in region A[b] (mAh/g)	First discharge capacity (mAh/g)
					Region A	Region B	Total (regions A+B)		
0.5	0.2	$Li[Li_{0.27}Mn_{0.53}Co_{0.1}Ni_{0.1}]O_2$	$Li[Li_{0.27}Mn_{0.53}Co_{0.1}Ni_{0.1}]O_2$	3.74	65	220	285	54	173
	0.3	$Li[Li_{0.23}Mn_{0.47}Co_{0.15}Ni_{0.15}]O_2$	$Li[Li_{0.23}Mn_{0.47}Co_{0.15}Ni_{0.15}]O_2$	3.60	95	281	376	87	257
	0.4	$Li[Li_{0.2}Mn_{0.4}Co_{0.2}Ni_{0.2}]O_2$	$Li[Li_{0.19}Mn_{0.41}Co_{0.2}Ni_{0.2}]O_2$	3.47	115	239	354	118	249
	0.5	$Li[Li_{0.17}Mn_{0.33}Co_{0.25}Ni_{0.25}]O_2$	$Li[Li_{0.15}Mn_{0.35}Co_{0.25}Ni_{0.25}]O_2$	3.35	145	185	330	147	232
	0.6	$Li[Li_{0.13}Mn_{0.26}Co_{0.3}Ni_{0.3}]O_2$	$Li[Li_{0.11}Mn_{0.27}Co_{0.31}Ni_{0.31}]O_2$	3.25	160	147	307	172	205
	0.7	$Li[Li_{0.1}Mn_{0.2}Co_{0.35}Ni_{0.35}]O_2$	$Li[Li_{0.07}Mn_{0.21}Co_{0.36}Ni_{0.36}]O_2$	3.15	185	121	306	201	213

[a] Regions A and B correspond to, respectively, the initial sloping region A and the plateau region B as marked in Figure 5.21.
[b] Calculated assuming the oxidation of Mn, Ni, and Co, respectively, to Mn^{4+}, Ni^{4+}, and $Co^{3.75+}$.

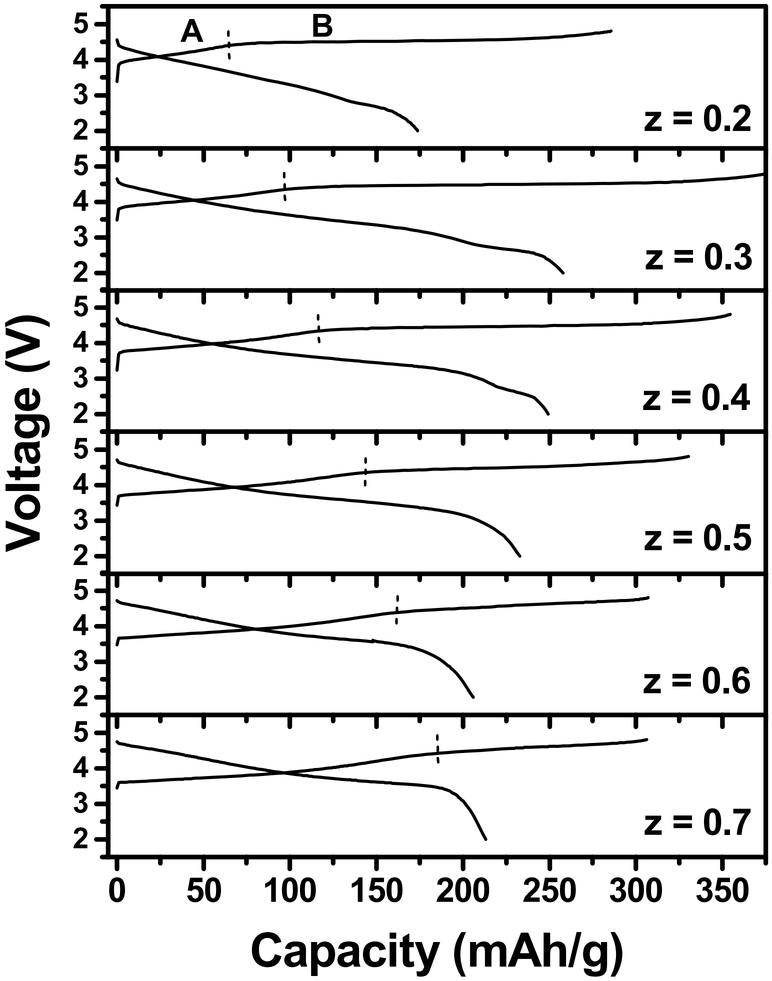

Figure 5.21: Comparison of the first charge-discharge profiles (recorded at 12.5 mA/g between 2.0 – 4.8 V) of the (1-z) Li[$Li_{1/3}Mn_{2/3}$]O_2 · (z) Li[$Co_{1-y}Ni_y$]O_2 (y = 0.5 and $0.2 \leq z \leq 0.7$) samples synthesized at 750 °C. The dashed vertical lines separate the initial sloping region A from the plateau region B.

However, the first charge capacities in region A of the 750 °C samples are in general smaller than that observed with the 900 °C samples. Also, the first charge capacities in the plateau region B and the total first charge and discharge capacities of the 750 °C samples are higher compared to that in the 900 °C sample. This could be the result of the presence of higher amount of lithium ions in the transition metal layer and a consequent loss of higher amount of oxygen from the lattice during the first charge of the 750 °C samples compared to that in the 900 °C samples (compare observed compositions in Tables 5.5 and 5.7). A good agreement between the observed and calculated charge capacities in the sloping region A confirm the oxygen evolution from the lattice for oxidations beyond approximately $Co^{3.75+}$ for the samples synthesized at 750 °C.

Figure 5.22 compares the cyclability of the samples synthesized at 750 °C for various z values at 12.5 mA/g between 2.0 - 4.8 V. Similar to the 900 °C samples, the 750 °C samples with an intermediate z value (0.4 and 0.5) shows better cyclability compared to the samples with high Co content (0.6 and 0.7) and high Mn content (0.2 and 0.3).

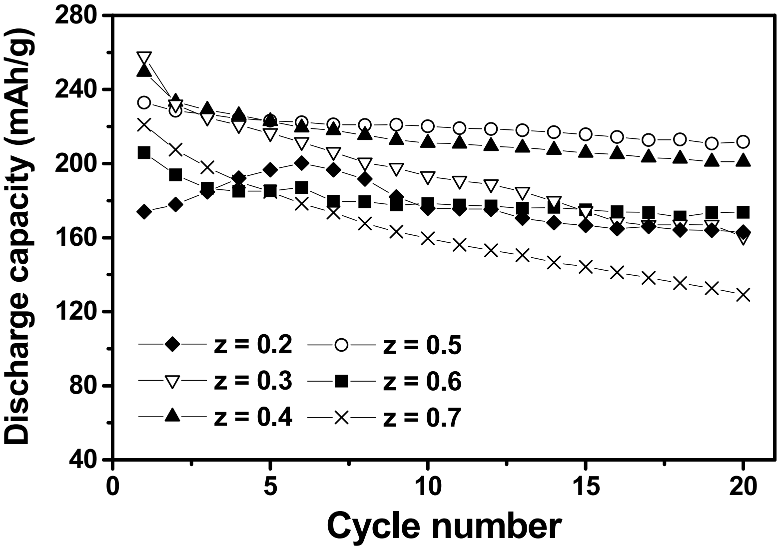

Figure 5.22: Comparison of the cyclability data (12.5 mA/g between 2.0 – 4.8 V) of the (1-z) $Li[Li_{1/3}Mn_{2/3}]O_2 \cdot$ (z) $Li[Co_{1-y}Ni_y]O_2$ ($y = 0.5$ and $0.2 \leq z \leq 0.7$) samples synthesized at 750 °C.

5.3.5.3 Chemical stability of delithiated samples

To understand the factors that control the reversible capacity values, we performed chemical characterizations on bulk samples obtained by chemically extracting lithium from layered (1-z) $Li[Li_{1/3}Mn_{2/3}]O_2 \cdot$ (z) $Li[Co_{1-y}Ni_y]O_2$ (y = 0.5 and $0.2 \leq z \leq 0.7$) samples synthesized at 750 °C with the oxidizer NO_2BF_4 in acetonitrile medium. Table 5.8 gives the compositions of the delithiated samples that were calculated based on the experimentally determined lithium content, proton content, and oxidation state values. The amount of proton inserted into the 750 °C samples were found to be higher than that in the 900 °C samples. This could probably be due to the smaller particle size of the 750 °C samples (~0.2 μm) compared to the 900 °C samples (~1 μm) as seen in Figure 5.23 for the z = 0.2 sample. The smaller particle size provides a larger surface area for the ion exchange of Li^+ ions by H^+ ions, resulting in higher proton insertion in the 750 °C samples compared to the 900 °C samples.

Table 5.8 gives the limiting oxygen content values calculated based on the mechanism proposed by Armstrong *et al*,[134] as well as the observed chemical compositions obtained by normalizing the oxygen content to 2.0. The calculated limiting oxygen content values agree closely with the observed oxygen content values in the delithiated samples for $z \geq 0.4$ (see the formula before cation rearrangement). For samples with $z < 0.4$, the observed oxygen content values in the delithiated samples were found to be higher than the calculated limiting oxygen content values and the difference increases with decreasing z value. A larger observed oxygen content values (or smaller amount of oxygen loss) in the case of samples with low z value could be due to the presence of a significant amount of electrochemically inactive Mn^{4+} ions in the parent samples and the consequent decrease in the oxygen mobility to leave the lattice, as seen before for the 900 °C samples. Thus, a smaller plateau region B and a lower total charge and discharge capacities than that expected in the case of the z = 0.2 sample (Table 5.7) is due to the presence of a significant amount of electrochemically inactive Mn^{4+} ions in the lattice.

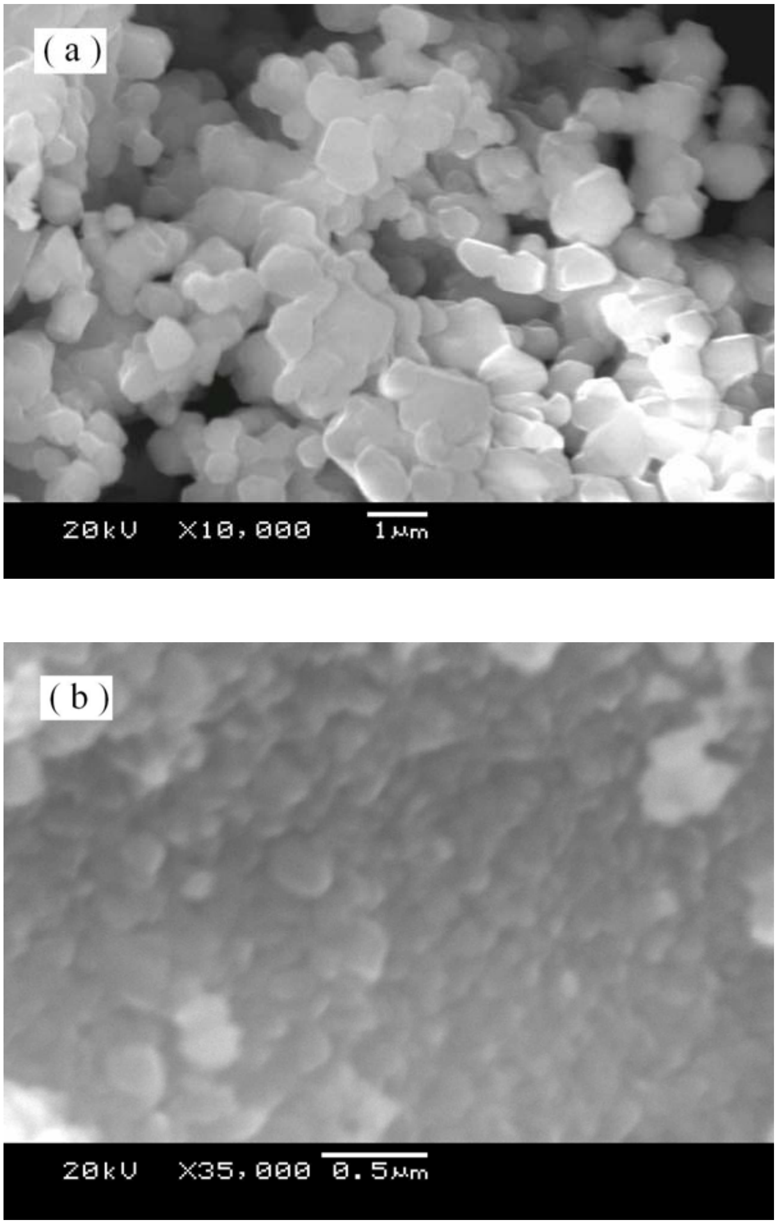

Figure 5.23: SEM images of the (1-z) $Li[Li_{1/3}Mn_{2/3}]O_2 \cdot$ (z) $Li[Co_{1-y}Ni_y]O_2$ (y = 0.5 and z = 0.2) sample synthesized at (a) 900 ^{o}C and (b) 750 ^{o}C.

Table 5.8: Chemical analysis data of chemically delithiated (1-z) $Li[Li_{1/3}Mn_{2/3}]O_2$ · (z) $Li[Co_{1-y}Ni_y]O_2$ (y = 0.5 and 0.2 ≤ z ≤ 0.7) samples synthesized at 750 °C.

y	z	Observed parent composition	Observed composition after chemical delithiation[a]		M^{n+}	Calculated limiting oxygen content (2-δ)[b]
			Before rearrangement	After rearrangement		
0.5	0.2	$Li[Li_{0.27}Mn_{0.53}Co_{0.1}Ni_{0.1}]O_2$	$H_{0.48}[Li_{0.27}Mn_{0.53}Co_{0.1}Ni_{0.1}]O_{1.72}$	$Li_{0.16}H_{0.56}[Li_{0.15}Mn_{0.61}Co_{0.12}Ni_{0.12}]O_2$	3.68	1.46
	0.3	$Li[Li_{0.23}Mn_{0.47}Co_{0.15}Ni_{0.15}]O_2$	$H_{0.27}[H_{0.09}Li_{0.14}Mn_{0.47}Co_{0.15}Ni_{0.15}]O_{1.66}$	$Li_{0.1}H_{0.43}[Li_{0.07}Mn_{0.57}Co_{0.18}Ni_{0.18}]O_2$	3.67	1.54
	0.4	$Li[Li_{0.19}Mn_{0.41}Co_{0.2}Ni_{0.2}]O_2$	$H_{0.23}[H_{0.11}Li_{0.08}Mn_{0.41}Co_{0.2}Ni_{0.2}]O_{1.61}$	$Li_{0.11}H_{0.43}[Mn_{0.5}Co_{0.25}Ni_{0.25}]O_2$	3.45	1.62
	0.5	$Li[Li_{0.15}Mn_{0.35}Co_{0.25}Ni_{0.25}]O_2$	$H_{0.29}[H_{0.15}Li_{0.07}Mn_{0.35}Co_{0.25}Ni_{0.25}]O_{1.70}$	$Li_{0.08}H_{0.52}[Mn_{0.42}Co_{0.29}Ni_{0.29}]O_2$	3.40	1.70
	0.6	$Li[Li_{0.11}Mn_{0.27}Co_{0.31}Ni_{0.31}]O_2$	$H_{0.42}[H_{0.04}Li_{0.08}Mn_{0.27}Co_{0.31}Ni_{0.31}]O_{1.76}$	$Li_{0.1}H_{0.53}[Mn_{0.3}Co_{0.35}Ni_{0.35}]O_2$	3.35	1.78
	0.7	$Li[Li_{0.07}Mn_{0.21}Co_{0.36}Ni_{0.36}]O_2$	$H_{0.55}[Li_{0.07}Mn_{0.21}Co_{0.36}Ni_{0.36}]O_{1.86}$	$Li_{0.08}H_{0.59}[Mn_{0.22}Co_{0.39}Ni_{0.39}]O_2$	3.33	1.86

[a] Determined based on the experimentally observed lithium and proton contents and oxidation state values.

[b] Calculated based on the maximum amount of oxygen the sample could lose (see text).

5.3.6 Correlation between lithium content in the transition metal layer and oxygen loss in the $Li[Li_{1/3}Mn_{2/3}]O_2$ – $LiCoO_2$ – $LiNiO_2$ solid solution cathodes

With an aim to acquire a complete understanding of the factors that influences the irreversible oxygen loss, we performed chemical characterizations of additional bulk samples obtained by chemically extracting lithium from the solid solution samples in the (1-z) $Li[Li_{1/3}Mn_{2/3}]O_2 \cdot$ (z) $Li[Co_{1-y}Ni_y]O_2$ ($0 \leq y \leq 1$and $0 \leq z \leq 1$) system that were not investigated so far in the previous sections. Figure 5.24 indicates the compositions that were investigated in this section (open circles) in addition to the compositions that were investigated in the previous sections (closed circles).

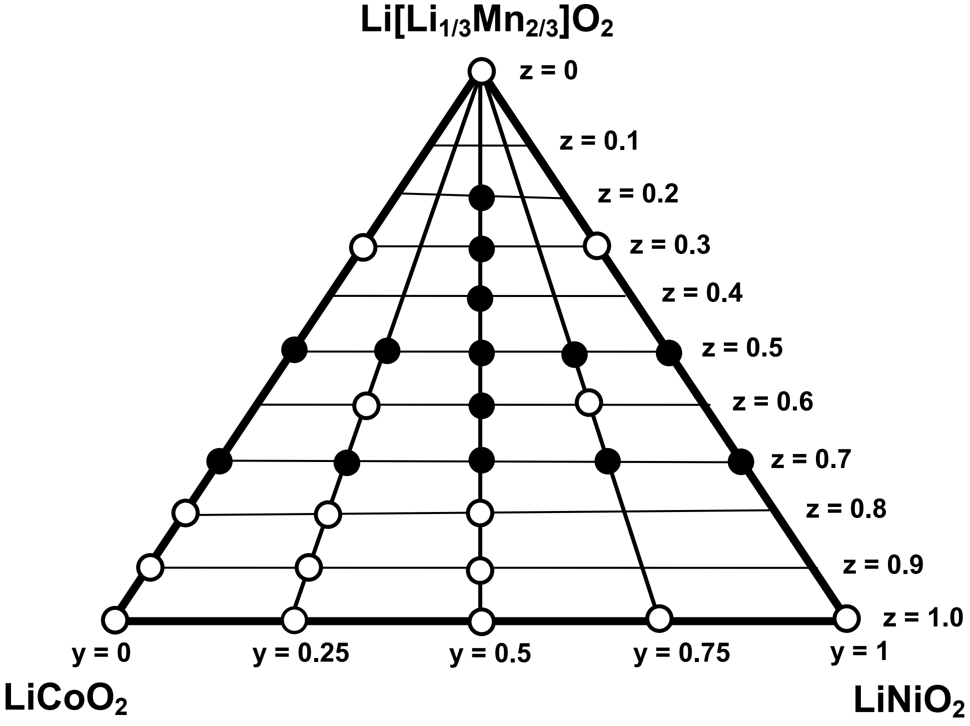

Figure 5.24: Phase diagram of the $Li[Li_{1/3}Mn_{2/3}]O_2$ - $LiCoO_2$ - $LiNiO_2$ system. The compositions studied in this section are indicated by open circles, while the composition studied in the previous sections are indicated by closed circles.

Table 5.9: Observed chemical compositions of the parent and chemically delithiated (1-z) $Li[Li_{1/3}Mn_{2/3}]O_2 \cdot$ (z) $Li[Co_{1-y}Ni_y]O_2$ ($0 \leq y \leq 1$ and $0 \leq z \leq 1$) samples synthesized at 900 °C.

y	z	Nominal composition	Observed parent composition	Observed composition after chemical delithiation[a]	M^{n+}	Calculated limiting oxygen content (2-δ)[b]
0	1.0	$Li[Co]O_2$	$Li[Co]O_2$	$Li_{0.02}H_{0.40}[Co]O_{1.99}$	3.55	2.00
0.25	1.0	$Li[Co_{0.75}Ni_{0.25}]O_2$	$Li_{0.98}Ni_{0.02}[Co_{0.77}Ni_{0.23}]O_2$	$Li_{0.02}H_{0.36}Ni_{0.02}[Co_{0.77}Ni_{0.23}]O_{1.95}$	3.44	2.00
0.5	1.0	$Li[Co_{0.5}Ni_{0.5}]O_2$	$Li_{0.94}Ni_{0.06}[Co_{0.53}Ni_{0.47}]O_2$	$Li_{0.03}H_{0.22}Ni_{0.06}[Co_{0.53}Ni_{0.47}]O_{2.01}$	3.55	2.00
0.75	1.0	$Li[Co_{0.25}Ni_{0.75}]O_2$	$Li_{0.9}Ni_{0.1}[Co_{0.28}Ni_{0.72}]O_2$	$Li_{0.72}Ni_{0.1}[Co_{0.28}Ni_{0.72}]O_{1.99}$	2.96	2.00
1.0	1.0	$Li[Ni]O_2$	$Li_{0.85}Ni_{0.15}[Ni]O_{1.80}$	$Li_{0.66}Ni_{0.15}[Ni]O_{1.80}$	2.56	2.00
0	0.9	$Li[Li_{0.03}Mn_{0.07}Co_{0.9}]O_2$	$Li[Li_{0.02}Mn_{0.07}Co_{0.91}]O_2$	$Li_{0.02}H_{0.36}[Li_{0.02}Mn_{0.07}Co_{0.91}]O_{1.94}$	3.55	1.96
0.25	0.9	$Li[Li_{0.03}Mn_{0.07}Co_{0.67}Ni_{0.23}]O_2$	$Li[Li_{0.01}Mn_{0.07}Co_{0.69}Ni_{0.23}]O_2$	$Li_{0.08}H_{0.34}[Li_{0.01}Mn_{0.07}Co_{0.69}Ni_{0.23}]O_{1.98}$	3.56	1.98
0.5	0.9	$Li[Li_{0.03}Mn_{0.07}Co_{0.45}Ni_{0.45}]O_2$	$Li_{0.99}Ni_{0.01}[Mn_{0.07}Co_{0.47}Ni_{0.46}]O_2$	$Li_{0.02}H_{0.30}Ni_{0.01}[Mn_{0.07}Co_{0.47}Ni_{0.46}]O_{1.95}$	3.55	2.00

0	0.8	$Li[Li_{0.07}Mn_{0.13}Co_{0.8}]O_2$	$Li[Li_{0.06}Mn_{0.13}Co_{0.81}]O_2$	$Li_{0.04}H_{0.44}[Li_{0.06}Mn_{0.13}Co_{0.81}]O_{1.88}$	3.43	1.88
0.25	0.8	$Li[Li_{0.07}Mn_{0.13}Co_{0.6}Ni_{0.2}]O_2$	$Li[Li_{0.04}Mn_{0.13}Co_{0.62}Ni_{0.21}]O_2$	$Li_{0.02}H_{0.41}[Li_{0.04}Mn_{0.13}Co_{0.62}Ni_{0.21}]O_{1.91}$	3.49	1.92
0.5	0.8	$Li[Li_{0.07}Mn_{0.13}Co_{0.4}Ni_{0.4}]O_2$	$Li[Li_{0.02}Mn_{0.14}Co_{0.42}Ni_{0.42}]O_2$	$Li_{0.01}H_{0.46}[Li_{0.02}Mn_{0.14}Co_{0.42}Ni_{0.42}]O_{1.93}$	3.44	1.96
0.25	0.6	$Li[Li_{0.13}Mn_{0.27}Co_{0.45}Ni_{0.15}]O_2$	$Li[Li_{0.12}Mn_{0.27}Co_{0.46}Ni_{0.15}]O_2$	$Li_{0.01}H_{0.26}[Li_{0.12}Mn_{0.27}Co_{0.46}Ni_{0.15}]O_{1.76}$	3.56	1.76
0.75	0.6	$Li[Li_{0.13}Mn_{0.27}Co_{0.15}Ni_{0.45}]O_2$	$Li[Li_{0.04}Mn_{0.29}Co_{0.17}Ni_{0.5}]O_2$	$Li_{0.07}H_{0.2}[Li_{0.04}Mn_{0.29}Co_{0.17}Ni_{0.5}]O_{1.92}$	3.69	1.92
0.0	0.3	$Li[Li_{0.23}Mn_{0.47}Co_{0.3}]O_2$	$Li[Li_{0.23}Mn_{0.47}Co_{0.3}]O_2$	$Li_{0.26}H_{0.17}[Li_{0.23}Mn_{0.47}Co_{0.3}]O_{1.78}$	3.76	1.54
1.0	0.3	$Li[Li_{0.23}Mn_{0.47}Ni_{0.3}]O_2$	$Li[Li_{0.20}Mn_{0.49}Ni_{0.31}]O_2$	$Li_{0.02}H_{0.40}[Li_{0.2}Mn_{0.49}Ni_{0.31}]O_{1.82}$	3.77	1.60
0.0	0.0	$Li[Li_{0.33}Mn_{0.67}]O_2$	$Li[Li_{0.33}Mn_{0.67}]O_2$	$Li_{0.98}H_{0.02}[Li_{0.33}Mn_{0.67}]O_{2.01}$	4.02	1.34
0.0	0.0	$Li[Li_{0.33}Mn_{0.67}]O_2$[c]	$Li[Li_{0.33}Mn_{0.67}]O_2$	$Li_{0.82}H_{0.13}[Li_{0.33}Mn_{0.67}]O_{1.99}$	4.03	1.34
0.5	1.0	$Li[Co_{0.5}Ni_{0.5}]O_2$[c]	$Li[Co_{0.5}Ni_{0.5}]O_2$	$Li_{0.07}H_{0.45}[Co_{0.5}Ni_{0.5}]O_{1.96}$	3.39	2.00

[a] Determined based on the experimentally observed lithium and proton contents and oxidation state values.
[b] Calculated based on the maximum amount of oxygen the sample could lose (see text).
[c] Samples synthesized at 750 °C.

Table 5.9 gives the nominal compositions and the observed compositions based on the experimentally determined lithium contents and the average oxidation state of the transition metal ions for the parent samples indicated by open circles in Figure 5.24. All the samples were found to be single phase, crystallizing in the layered O3 type structure. However, for the same z value, the observed lithium content decreases with increasing Ni content y due to the difficulty of stabilizing Ni^{3+} and a consequent reduction of some Ni^{3+} to Ni^{2+} and volatilization of some lithium during synthesis at 900 ^{o}C. For example, for z = 1, the observed lithium content decreases from 1 to 0.85 as the y value increases from 0 to 1. In addition, the observed composition $Li_{0.85}Ni_{0.15}[Ni]O_{1.80}$ (y = 1, z = 1) shows oxygen deficiency to compensate for the reduction of Ni^{3+} to Ni^{2+} during synthesis at 900 ^{o}C and maintain charge neutrality.

Table 5.9 gives the observed chemical compositions of the delithiated samples that were calculated based on the experimentally determined lithium content, proton content, and oxidation state values as well as the limiting oxygen content values calculated based on the mechanism proposed by Armstrong *et al.*[6] According to the mechanism, the composition $Li[Li_{\eta}M_{1-\eta}]O_2$ (where M is a combination of transition metal ions) losses oxygen on electrochemically charging to high voltages (or on complete delithiation) and transforms to the composition $[M_{1-\eta}]O_{2-2\eta}$, where the transition metal layer is occupied exclusively by the transition metal ions. In essence, the mechanism predicted the limiting (or lowest) oxygen content value in the delithiated sample to be twice that of the transition metal ion content or the maximum amount of oxygen loss from the lattice to be twice the amount of lithium in the transition metal layer. To test the validity of the mechanism, we made a plot (Figure 5.25) of the amount of lithium in the transition metal layer of the parent sample versus the absorbed oxygen loss in the chemically delithiated (1-z) $Li[Li_{1/3}Mn_{2/3}]O_2 \cdot$ (z) $Li[Co_{1-y}Ni_y]O_2$ ($0 \leq y \leq 1$and $0 \leq z \leq 1$)

solid solution samples that were investigated so far in this work. The solid line in Figure 5.25 corresponds to the theoretically expected oxygen loss based on the above described mechanism.

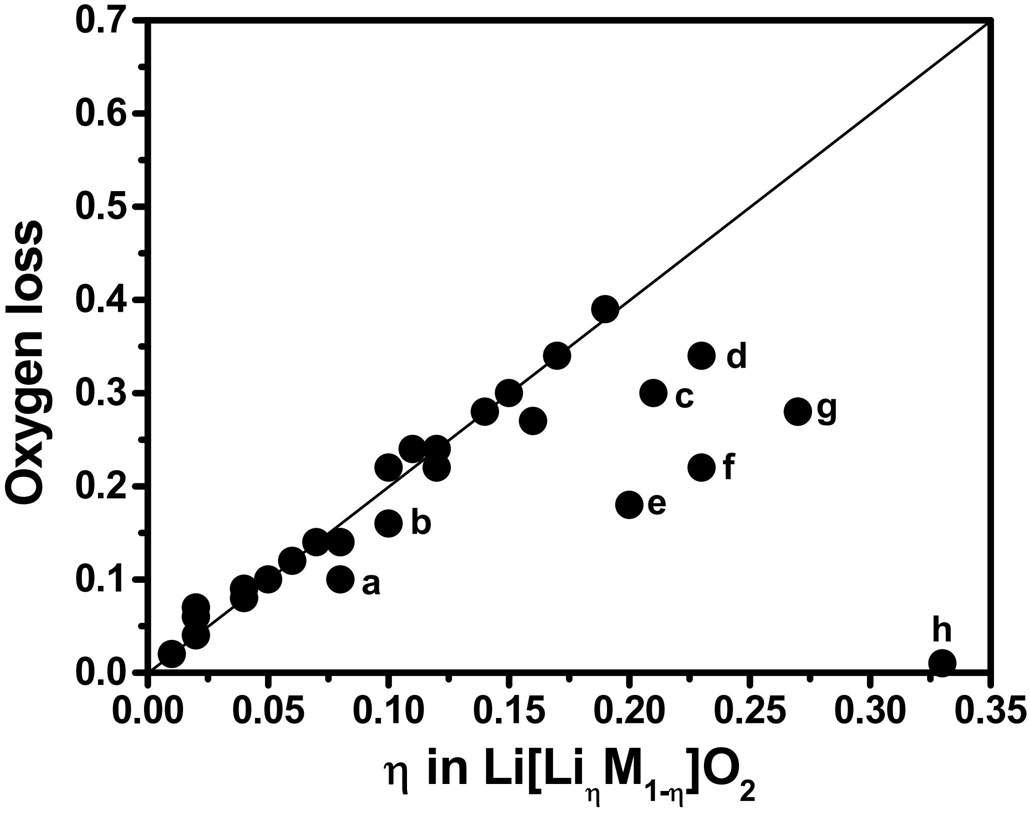

Figure 5.25: Correlation between lithium content in the transition metal layer and oxygen loss in the $Li[Li_{1/3}Mn_{2/3}]O_2$ – $LiCoO_2$ – $LiNiO_2$ solid solution cathodes. (a) $Li[Li_{0.08}Mn_{0.37}Ni_{0.55}]O_2$, (b) $Li[Li_{0.10}Mn_{0.36}Co_{0.13}Ni_{0.41}]O_2$, (c) $Li[Li_{0.21}Mn_{0.48}Co_{0.155}Ni_{0.155}]O_2$, (d) $Li[Li_{0.23}Mn_{0.47}Co_{0.15}Ni_{0.15}]O_2$, (e) $Li[Li_{0.2}Mn_{0.49}Ni_{0.31}]O_2$, (f) $Li[Li_{0.23}Mn_{0.47}Co_{0.3}]O_2$, (g) $Li[Li_{0.27}Mn_{0.53}Co_{0.1}Ni_{0.1}]O_2$, and (h) $Li[Li_{0.33}Mn_{0.67}]O_2$.

The observed oxygen loss from the chemically delithiated solid solution samples agree closely with the theoretically expected oxygen loss for $\eta < 0.20$. A slightly smaller amount of oxygen loss for a few samples with $\eta < 0.20$ (data points a and b in Figure 5.25) could be due to the presence of high Ni content and cation disorder and the consequent changes in the electronic environment and lithium and oxygen mobility. For $\eta \geq 0.20$, the observed oxygen loss values were found to be much lower than the expected values due to the presence of a high concentration of electrochemically inactive Mn^{4+} ions ($z \leq 0.3$) in the parent samples (data points c to h in Figure 5.25) and the consequent decrease in the lithium and oxygen mobility to leave the lattice. In fact, the composition $Li[Li_{0.33}Mn_{0.67}]O_2$ (h in Figure 5.25), with all manganese at 4+ oxidation state, does not lose much lithium and oxygen on reacting with the NO_2BF_4 oxidizer (Table 5.9). In addition to a high manganese content, the composition $Li[Li_{0.2}Mn_{0.49}Ni_{0.31}]O_2$ (e in Figure 5.25) also has a high nickel content that results in a lower oxygen loss from the compound.

5.4 CONCLUSIONS

The irreversible oxygen loss during the first charge from the layered solid solutions between $Li[Li_{1/3}Mn_{2/3}]O_2$, $Li[Co]O_2$, and $Li[Ni]O_2$ has been found to be determined by the amount of lithium in the transition metal layer before charge by investigating systematically five different series of samples in the $(1-z)\ Li[Li_{1/3}Mn_{2/3}]O_2 \cdot (z)\ Li[Ni_{1-y}Co_y]O_2$ systems. The lithium content in the transition metal layer is, however, sensitively influenced by the tendency of Ni^{3+} to get reduced to Ni^{2+} and the consequent volatilization of lithium during synthesis. The amount of oxygen loss during first charge in turn influences the reversible capacity values in subsequent cycles. Furthermore, while Ni^{2+} could be fully oxidized to Ni^{4+}, the oxygen loss begins to occur for oxidations beyond $Co^{3.6+}$ due to a significant overlap of the $Co^{3+/4+}$:3d band with the top of the O^{2-}:2p band. In addition, high Mn^{4+} content causes a decrease in oxygen mobility and loss. The study shows that the irreversible oxygen loss from the lattice and the reversible capacity values in the subsequent cycles could be tuned by appropriate choice of transition metal ions and contents as well as the lithium content in the parent material via the synthesis temperatures employed.

CHAPTER 6

Structural Stability of Chemically Delithiated $Li[Li_{1/3}Mn_{2/3}]O_2$ – $LiCoO_2$ – $LiNiO_2$ Solid Solution Oxides

6.1 INTRODUCTION

Alkali metal oxides with the general formula A_xMO_2 (A = alkali metal and M = transition metal) normally crystallize in layered structures in which the A^+ ions are sandwiched between the $(MO_2)_n$ sheets formed by the edge shared MO_6 octahedra. Based on the coordination environment of the A^+ ions (octahedral, prismatic, or tetrahedral) and the number of $(MO_2)_n$ sheets per unit cell, Delmas[20] classified these layered A_xMO_2 oxides into various types of structures such as O1, O3, P2, P3, T2, and T3 (O, P, and T refer to octahedral, prismatic, and tetrahedral). For example, $Na_{0.7}CoO_2$ has the P2 type structure in which Na^+ ions occupy prismatic sites with two CoO_2 sheets per unit cell.[148]

Based on the above classification, the $LiMO_2$ (M = Co and Ni) oxides, which were commonly used as cathode materials in lithium ion batteries, have the O3 type structure (space group: $R\bar{3}m$) as shown in Figure 6.1a. In this structure, the lithium ions occupy the octahedral sites with three MO_2 sheets per unit cell and an oxygen stacking sequence of ABCABC along the *c* axis. However, during the lithium extraction (charging) process, the MO_2 sheets can slide relative to one another, yielding the P3 type structure (space group: $R3m$) or the O1 type structure (space group: $P\bar{3}m1$) that have an oxygen stacking sequence of, respectively, AABBCC and ABABAB along the *c* axis (Figures 6.1b and c). Such a gliding of sheets involves very low reaction energies without the breaking of any M-O bonds and, therefore, can occur at room temperature.[149] However, the O1 structure is thermodynamically preferred when all the lithium ions are extracted due to a reduced interaction between the O^{2-}: 2p orbitals of the adjacent oxide ion layers.[27]

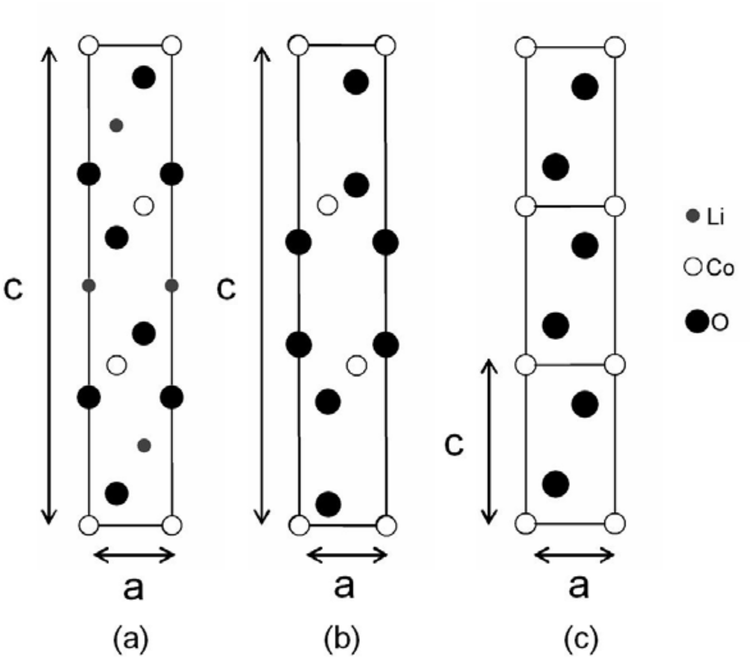

Figure 6.1: Crystal structures of (a) O3 type $LiMO_2$, (b) P3 type MO_2, and (c) O1 type MO_2 viewed along the (100) plane.

As discussed in chapter 4, our group has been focusing on the chemical and structural instabilities of the layered $Li_{1-x}MO_2$ ($0 \leq (1-x) \leq 1$ and M = 3d transition metal or their solid solutions) oxides that were obtained by chemically extracting lithium with NO_2BF_4 in acetonitrile medium with an aim to understand the factors that control the reversible capacities of these layered oxide cathodes in lithium ion batteries.[23,24,29,120-123] The chemical and structural characterization data of the chemically delithiated samples reveal that the instability associated with the $Li_{1-x}CoO_2$ system leads to a sliding of the oxide ion layers and a transformation of the initial O3 structure to the P3 structure at low lithium contents, which limits its practical capacity to 140 mA h/g. In contrast, the Li_{1-}

$_x$$Ni_{0.85}Co_{0.15}O_2$ system maintains the initial O3 layer structure to low lithium contents, which allows it to realize a much higher practical capacity (180 mAh/g).[23,120] In general, the nickel-rich end members of the $Li_{1-x}Co_{1-y}Ni_yO_2$ system maintains the initial O3 type structure, while the cobalt-rich end members transforms to a mixture of P3 and O1 phases on deep lithium extraction.[24] The manganese-rich $Li_{1-x}Ni_{0.5}Mn_{0.5}O_2$ system maintains the parent O3-type structure without the formation of any new phases for the entire lithium content $0 \leq (1\text{-}x) \leq 1$. In contrast, the $Li_{1-x}Ni_{0.75}Mn_{0.25}O_2$ system shows a new O3' phase, with a smaller c parameter for $(1 - x) < 0.29$.[122]

We present here a comparison of the structures of the fully delithiated samples obtained by chemically extracting all the lithium from the layered (1-z) $Li[Li_{1/3}Mn_{2/3}]O_2 \cdot$ (z) $Li[Co_{1-y}Ni_y]O_2$ ($0 \leq y \leq 1$ and $0 \leq z \leq 1$) solid solution samples with the oxidizer NO_2BF_4 in acetonitrile medium. The observed variations in the type of phases formed in the chemically delithiated solid solution samples are explained based on the degree of cation disorder, particle size of the parent sample, and proton content inserted into the delithiated samples.

6.2 EXPERIMENTAL

The samples were synthesized by a hydroxide precursor method and fired in air at 900 °C or 750 °C for 12 h followed by quenching in liquid nitrogen. Chemical extraction of lithium was carried out by stirring the layered oxide powder with an acetonitrile solution of the oxidizer NO_2BF_4 as explained in chapter 2.

All the samples were characterized by X-ray diffraction (XRD) and the lattice parameters were calculated with a Rietveld analysis of the XRD data. The lithium contents in the parent and chemically delithiated samples were determined by atomic absorption spectroscopy (AAS) and the proton contents in the delithiated samples were determined by prompt gamma-ray activation analysis (PGAA).

6.3 RESULTS AND DISCUSSION

6.3.1 Structural stability of chemically delithiated (1-z) $Li[Li_{1/3}Mn_{2/3}]O_2 \cdot$ (z) $Li[Co_{1-y}Ni_y]O_2$ ($0 \le y \le 1$ and $0 \le z \le 1$) solid solution oxides

The compositions studied in the (1-z) $Li[Li_{1/3}Mn_{2/3}]O_2 \cdot$ (z) $Li[Co_{1-y}Ni_y]O_2$ ($0 \le y \le 1$ and $0 \le z \le 1$) solid solution system are indicated by closed circles in Figure 6.2.

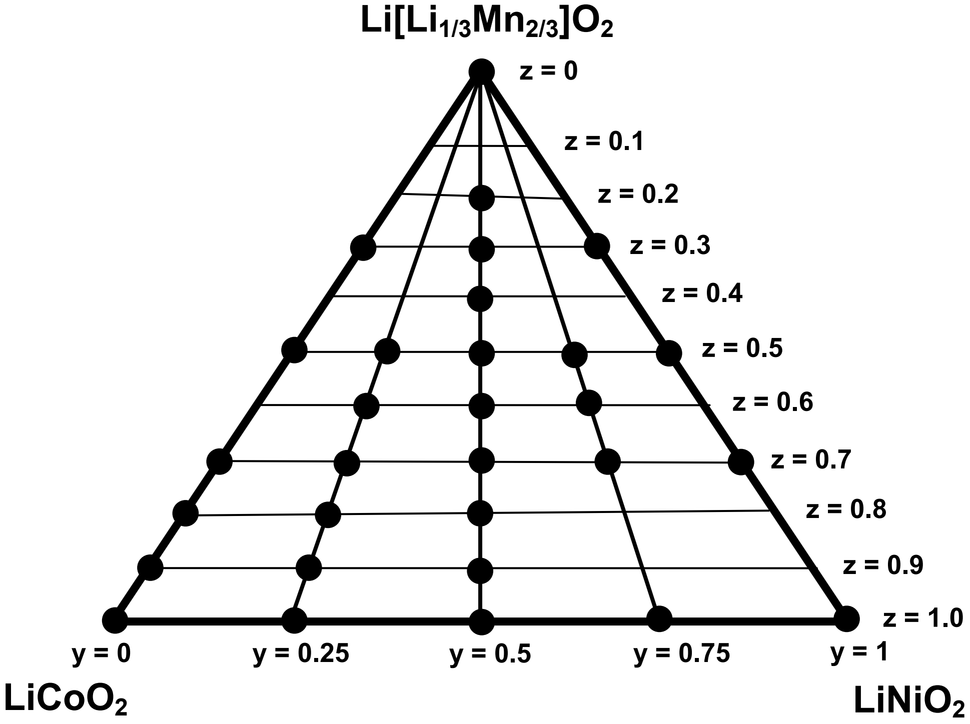

Figure 6.2: Phase diagram of the $Li[Li_{1/3}Mn_{2/3}]O_2$ - $LiCoO_2$ - $LiNiO_2$ system. The compositions studied in the (1-z) $Li[Li_{1/3}Mn_{2/3}]O_2 \cdot$ (z) $Li[Co_{1-y}Ni_y]O_2$ ($0 \le y \le 1$ and $0 \le z \le 1$) system are indicated by closed circles.

Tables 5.1, 5.4, 5.5, and 5.9 in chapter 5 give the nominal compositions and the observed compositions based on the experimentally determined lithium contents and the average oxidation state of the transition metal ions for the samples synthesized at 900 °C. In general, the observed lithium content decreases with increasing Ni content in the composition due to the difficulty of stabilizing Ni^{3+} and a consequent reduction of some Ni^{3+} to Ni^{2+} and volatilization of some lithium during synthesis at 900 °C. XRD data showed the samples to be single phase, crystallizing in the layered O3 type structure. However, in addition to the reflections corresponding to the O3 layered structure, weak superstructure reflections were observed around $2\theta = 20 - 25^{o}$ for samples with high $Li[Li_{1/3}Mn_{2/3}]O_2$ content, which are known to correspond to the ordering of the Li^+, Ni^{2+}, and Mn^{4+} ions in the transition metal layer of the layered lattice.[146,147] Tables 5.2, 5.4, 5.6, and 5.9 in chapter 5 give the compositions of the delithiated samples that were calculated based on the experimentally determined lithium content, proton content, and oxidation state values, respectively, by atomic absorption spectroscopy, prompt gamma-ray activation analysis, and redox titration. Most of the delithiated samples contain some residual lithium and inserted protons in the lithium plane.

Figure 6.3 shows the XRD patterns of the delithiated samples in the (1-z) $Li[Li_{1/3}Mn_{2/3}]O_2 \cdot (z)\ Li[Co_{1-y}Ni_y]O_2$ ($y = 0$ and $0 \leq z \leq 1$) series that were obtained by chemically extracting all the lithium from the parent samples synthesized at 900 °C. While the delithiated samples maintain the initial O3 structure for $z \leq 0.7$, the $z = 0.8$ sample shows the formation of the P3 structure in addition to the initial O3 structure. The $z = 0.9$ and 1.0 samples completely transform to the P3 structure on chemical delithiation. The P3 phase is formed by a gliding of selected MO_2 sheets at ambient temperature, as explained in the introduction. Figure 6.4 shows the Rietveld fitting of the X-ray diffraction data of the delithiated $z = 0.9$ sample. The P3 structure (space group: *R3m*) was fitted with the transition metal ions at the 3a site (0,0,0) and the oxide ions also at the 3a site $(0,0,z_{ox})$ and $(0,0,z'_{ox})$, where $z_{ox} = 0.641(3)$ and $z'_{ox} = 0.383(3)$. A good matching between the observed and calculated patterns with a low R_{wp} value and a satisfactory goodness of fit value *s* confirms the P3 type structure with a strictly two-dimensional nature.

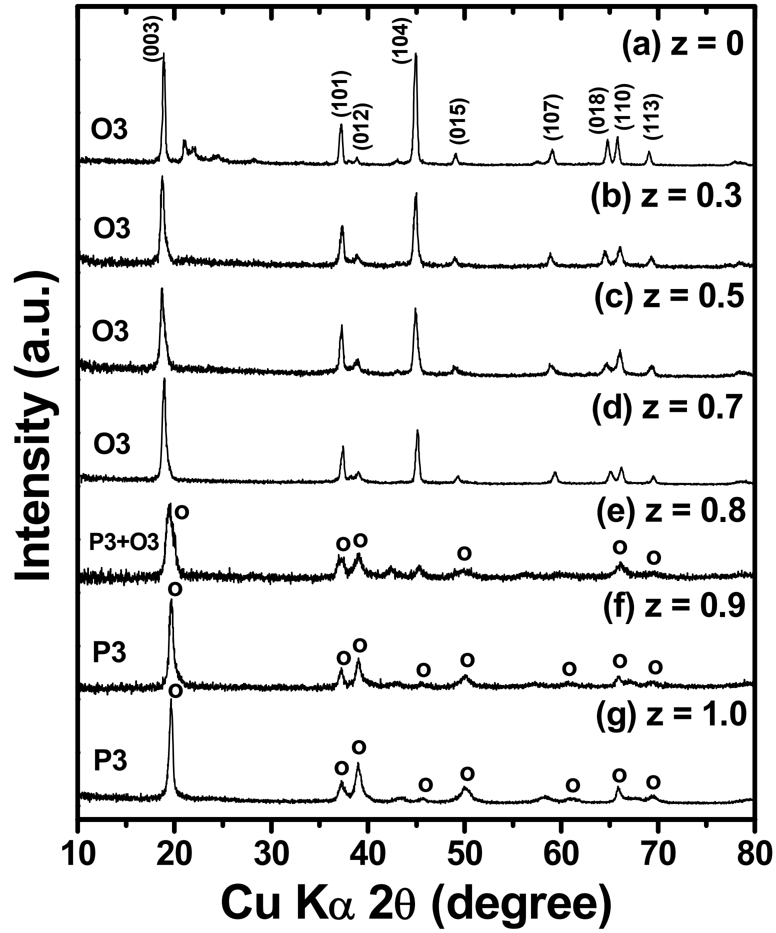

Figure 6.3: XRD patterns of the chemically delithiated samples obtained from the (1-z) $Li[Li_{1/3}Mn_{2/3}]O_2 \cdot$ (z) $Li[Co_{1-y}Ni_y]O_2$ ($y = 0$ and $0 \leq z \leq 1$) series synthesized at 900 °C. The reflections marked with hkl values refer to the layered O3 phase and those marked with o refer to the P3 phase.
(a) $Li_{0.98}H_{0.02}[Li_{0.33}Mn_{0.67}]O_{2.01}$, (b) $Li_{0.26}H_{0.17}[Li_{0.23}Mn_{0.47}Co_{0.3}]O_{1.78}$,
(c) $Li_{0.04}H_{0.18}[Li_{0.17}Mn_{0.33}Co_{0.5}]O_{1.66}$, (d) $Li_{0.07}H_{0.24}[Li_{0.1}Mn_{0.2}Co_{0.7}]O_{1.78}$,
(e) $Li_{0.04}H_{0.44}[Li_{0.06}Mn_{0.13}Co_{0.81}]O_{1.88}$, (f) $Li_{0.02}H_{0.36}[Li_{0.02}Mn_{0.07}Co_{0.91}]O_{1.94}$, and (g) $Li_{0.02}H_{0.40}[Co]O_{1.99}$.

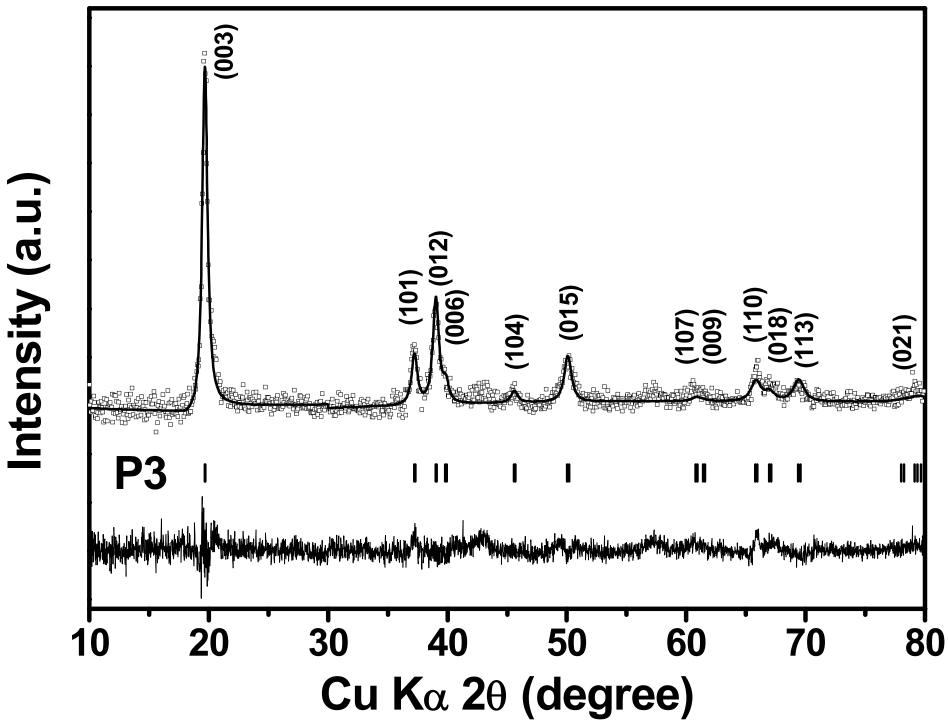

Figure 6.4: Rietveld fitting of the X-ray diffraction data of the chemically delithiated (1-z) $Li[Li_{1/3}Mn_{2/3}]O_2 \cdot (z) Li[Co_{1-y}Ni_y]O_2$ ($y = 0$ and $z = 0.9$) sample synthesized at 900 °C. $a = 2.8399(8)$ Å, $c = 13.597(9)$ Å, $V = 94.97(7)$ Å^3, $R_{wp} = 12.21$ %, $R_p = 9.51$ %, and $s = 2.13$. Squares and lines correspond, respectively, to the observed and calculated intensities. The difference between the observed and calculated patterns and the peak positions corresponding to the P3 type phase are also shown.

The compositions given in the caption to Figure 6.3 indicate a higher amount of proton insertion in the delithiated samples that transformed to the P3 structure, compared to those that retained the initial O3 structure. In this regard, the presence of protons in $H_{1-x}Li_x[Li_{0.33}Mn_{0.67}]O_2$ has been suggested before to favor the P3 type phase formation by hydrogen bonding.[125]

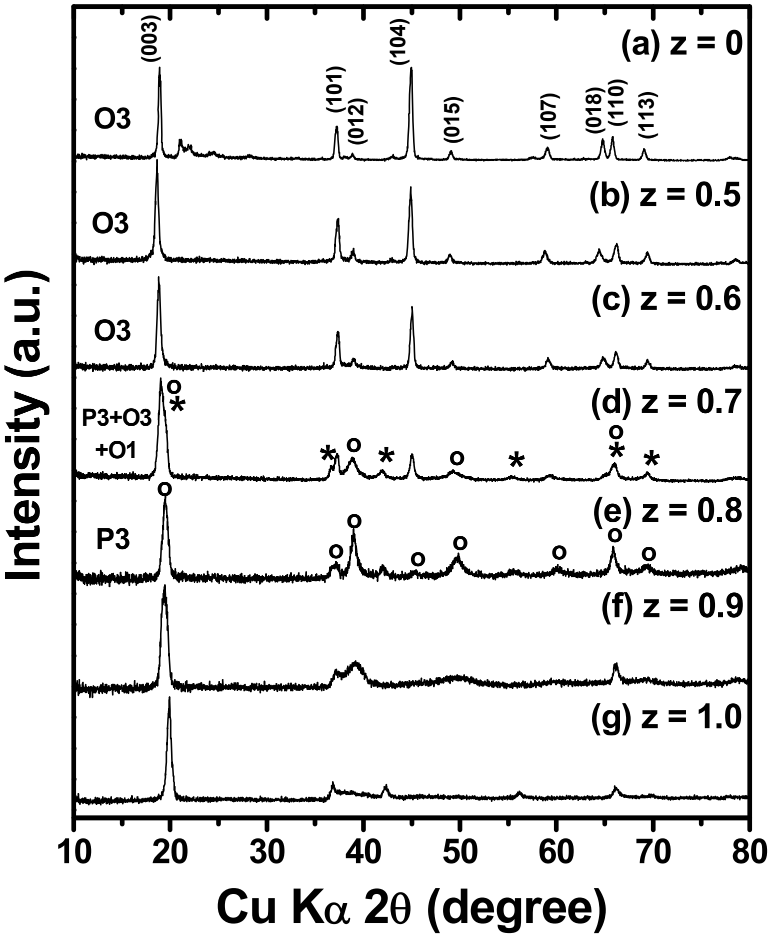

Figure 6.5: XRD patterns of the chemically delithiated samples obtained from the (1-z) $Li[Li_{1/3}Mn_{2/3}]O_2 \cdot (z)\ Li[Co_{1-y}Ni_y]O_2$ ($y = 0.25$ and $0 \leq z \leq 1$) series synthesized at 900 °C. The reflections marked with hkl values refer to the layered O3 phase and those marked with o and * refer to the P3 and O1 phases, respectively. (a) $Li_{0.98}H_{0.02}[Li_{0.33}Mn_{0.67}]O_{2.01}$,
(b) $Li_{0.09}H_{0.15}[Li_{0.14}Mn_{0.34}Co_{0.39}Ni_{0.13}]O_{1.72}$,
(c) $Li_{0.01}H_{0.26}[Li_{0.12}Mn_{0.27}Co_{0.46}Ni_{0.15}]O_{1.76}$,
(d) $Li_{0.04}H_{0.38}[Li_{0.08}Mn_{0.2}Co_{0.54}Ni_{0.18}]O_{1.86}$,
(e) $Li_{0.02}H_{0.41}[Li_{0.04}Mn_{0.13}Co_{0.62}Ni_{0.21}]O_{1.91}$,
(f) $Li_{0.08}H_{0.34}[Li_{0.01}Mn_{0.07}Co_{0.69}Ni_{0.23}]O_{1.98}$, and
(g) $Li_{0.02}H_{0.36}Ni_{0.02}[Co_{0.77}Ni_{0.23}]O_{1.95}$.

Figure 6.5 shows the XRD patterns of the delithiated samples in the y = 0.25 series synthesized at 900 °C. The delithiated samples maintain the initial O3 type structure for $z \leq 0.6$. For z = 0.7, the sample shows the formation of the P3 phase and a small amount of O1 phase in addition to the initial O3 structure. Similar to the P3 phase, the O1 phase is formed by a gliding of selected MO_2 sheets at ambient temperature, as explained in the introduction. The z = 0.8 sample completely transforms to the P3 structure on chemical delithiation. However, the poor crystallinity of the delithiated z = 0.9 and 1.0 samples made the Rietveld refinement of the XRD data unsatisfactory. Similar to the y = 0 series, the compositions of the y = 0.25 series given in the caption to Figure 6.5 indicates a higher amount of proton insertion into the delithiated samples that exhibit the P3 structure.

Figure 6.6 shows the XRD patterns of the delithiated samples in the y = 0.5 series synthesized at 900 °C. While the delithiated samples maintain the initial O3 structure for $z \leq 0.5$, the z = 0.6 sample shows the formation of the O1 phase in addition to the initial O3 structure. The z = 0.7 and 0.8 samples completely transform to the O1 structure on delithiation. Similar to the P3 type samples we saw before, the chemical compositions of the O1 type samples in the y = 0.5 series (given in the caption to Figure 6.6) indicate a higher amount of proton insertion, compared to the samples that retained their initial O3 structure. Figure 6.7 shows the Rietveld fitting of the X-ray diffraction data of the delithiated z = 0.7 sample. The O1 structure (space group: $P\bar{3}m1$) was fitted with the transition metal ions at the 1a site (0,0,0) and the oxide ions at the 2d site $(1/3,2/3,z_{ox})$, where $z_{ox} = 0.194(1)$. A good match between the observed and calculated patterns in Figure 6.7 confirms the O1 type structure of the z = 0.7 sample.

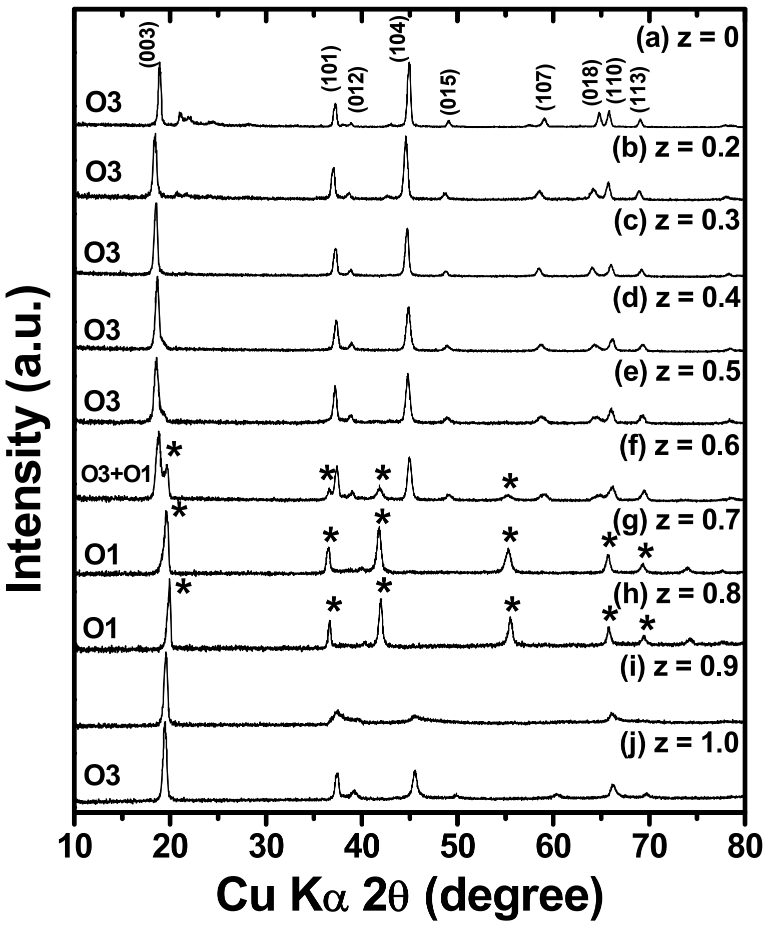

Figure 6.6: XRD patterns of the chemically delithiated samples obtained from the (1-z) $Li[Li_{1/3}Mn_{2/3}]O_2 \cdot$ (z) $Li[Co_{1-y}Ni_y]O_2$ ($y = 0.5$ and $0 \leq z \leq 1$) series synthesized at 900 ^{o}C. The reflections marked with hkl values refer to the layered O3 phase and those marked with * refer to the O1 phase.
(a) $Li_{0.98}H_{0.02}[Li_{0.33}Mn_{0.67}]O_{2.01}$, (b) $Li_{0.33}H_{0.03}[Li_{0.27}Mn_{0.53}Co_{0.1}Ni_{0.1}]O_{1.72}$,
(c) $Li_{0.19}H_{0.09}[Li_{0.21}Mn_{0.48}Co_{0.155}Ni_{0.155}]O_{1.70}$,
(d) $Li_{0.04}H_{0.12}[Li_{0.16}Mn_{0.42}Co_{0.21}Ni_{0.21}]O_{1.73}$,
(e) $Li_{0.05}H_{0.18}[Li_{0.12}Mn_{0.36}Co_{0.26}Ni_{0.26}]O_{1.78}$,
(f) $Li_{0.08}H_{0.26}[Li_{0.08}Mn_{0.28}Co_{0.32}Ni_{0.32}]O_{1.86}$,
(g) $Li_{0.02}H_{0.43}[Li_{0.05}Mn_{0.21}Co_{0.37}Ni_{0.37}]O_{1.90}$,
(h) $Li_{0.01}H_{0.46}[Li_{0.02}Mn_{0.14}Co_{0.42}Ni_{0.42}]O_{1.93}$,
(i) $Li_{0.02}H_{0.30}Ni_{0.01}[Mn_{0.07}Co_{0.47}Ni_{0.46}]O_{1.95}$, and
(j) $Li_{0.03}H_{0.22}Ni_{0.06}[Co_{0.53}Ni_{0.47}]O_{2.01}$.

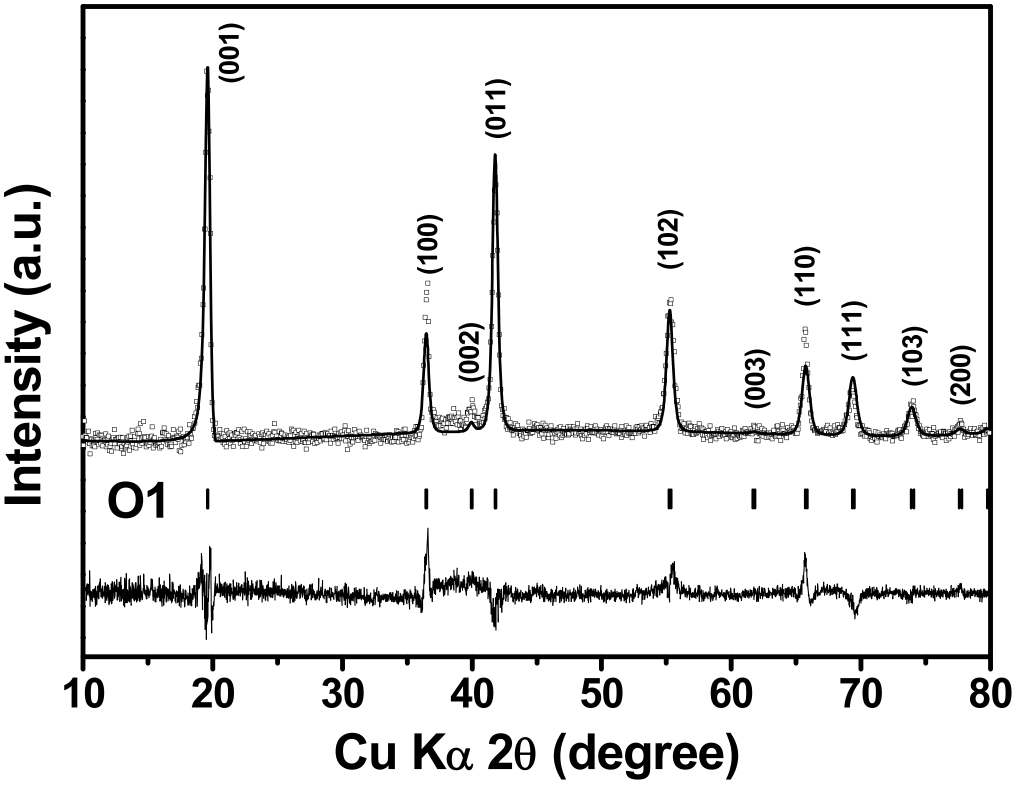

Figure 6.7: Rietveld fitting of the X-ray diffraction data of the chemically delithiated (1-z) $Li[Li_{1/3}Mn_{2/3}]O_2 \cdot (z) Li[Co_{1-y}Ni_y]O_2$ (y = 0.5 and z = 0.7) sample synthesized at 900 °C. $a = 2.8373(2)$ Å, $c = 4.5028(6)$ Å, $V = 31.393(5)$ Å^3, $R_{wp} = 11.98$ %, $R_p = 9.24$ %, and $s = 2.51$. Squares and lines correspond, respectively, to the observed and calculated intensities. The difference between the observed and calculated patterns and the peak positions corresponding to the O1 type phase are also shown.

Although the poor crystallinity of the delithiated z = 0.9 sample made the structure unidentifiable by Rietveld analysis, the z = 1.0 sample was found to retain its initial O3 structure on complete delithiation. The high cation disorder (5.5 %) of the z = 1.0 sample, as a result of the presence of Ni ions in the lithium plane (as evident from composition (j) given in the caption to Figure 6.6), could probably aid the sample to retain its initial O3 structure on delithiation. The cation disorder present in the parent samples may destabilize the formation of P3 and O1 type structures due to the electrostatic repulsion between the transition metal ions present in the lithium planes and transition metal planes across the shared polyhedral faces. In addition, the weak superstructure reflections observed around 2θ = 20 - 25° for the parent samples with high $Li[Li_{1/3}Mn_{2/3}]O_2$ content (Figure 5.15, z = 0.2, 0.3, and 0.4) corresponding to the ordering of the Li^+, Ni^{2+}, and Mn^{4+} ions in the transition metal layer of the layered lattice[146,147] were suppressed in the delithiated samples due to a cation rearrangement that occurs on deep lithium extraction, as explained in chapter 5. However, the parent $Li[Li_{0.33}Mn_{0.67}]O_2$ (z = 0) sample, with all manganese at 4+ oxidation state, does not lose much lithium or oxygen on reacting with the NO_2BF_4 oxidizer (composition (a) in Figure 6.6) due to poor electronic and ionic conductivity and thus maintains its initial superstructure reflections.

To investigate the effect of synthesis temperature, chemical delithiation experiments were performed on a second set of $(1-z)\ Li[Li_{1/3}Mn_{2/3}]O_2 \cdot (z)\ Li[Co_{1-y}Ni_y]O_2$ ($0 \leq y \leq 1$ and z = 0.5) samples synthesized at 750 °C. Tables 5.7, 5.8, and 5.9 in chapter 5 gives the nominal compositions, the observed compositions, and the composition of the chemically delithiated samples in the y = 0.5 series synthesized at 750 °C. Figure 6.8 shows the XRD patterns of the delithiated samples in the y = 0.5 series synthesized at 750 °C. Unlike the delithiated 900 °C samples, which either retained the initial O3 structure or transformed to O1 structure, the 750 °C delithiated samples show the formation of the P3 structure along with the initial O3 structure. The proportion of the P3 phase in the delithiated samples increases gradually from 63 % in the z = 0.2 sample to 81% in the z = 0.7 sample. In addition, the z = 0.7 sample exhibits a small amount of O1 phase. The poor crystallinity of the delithiated z = 1.0 sample made the structure unidentifiable by Rietveld analysis. The proton content found in the chemical compositions of the delithiated y = 0.5 samples synthesized at 750 °C are in general, higher than that found for the 900 °C samples (compare the compositions given in caption to Figures 6.6 and 6.8). As explained in chapter 5, the smaller particle size and larger surface area of the 750 °C samples may lead to the incorporation of a larger amount of proton during chemical delithiation, which could probably aid the transformation of the structure from O3 to P3. Additionally, a faster lithium extraction in the $Li[Ni_{1/3}Mn_{1/3}Co_{1/3}]O_2$ samples synthesized at lower temperatures was shown previously to lead the formation of the metastable P3 type phase, while the slow lithium extraction in the samples synthesized at higher temperatures leads to the formation of the thermodynamically more stable O1 type phase.[150]

Figure 6.9 shows the XRD patterns of the delithiated samples in the y = 0.75 series synthesized at 900 °C. Although the delithiated samples with an intermediate z value of 0.5 and 0.6 show the formation of a small amount of O1 structure, the y = 0.75 series in general maintains its initial O3 structure on chemical delithiation due to the presence of a high nickel content and a consequent cation disorder in the parent sample, as explained previously. In fact, the z = 1.0 sample does not lose much lithium during chemical delithiation as a result of a high cation disorder (10 %) in the parent sample, as evident from the composition (e) in Figure 6.9.

Figure 6.10 shows the XRD patterns of the delithiated samples in the y = 1.0 series synthesized at 900 °C. Similar to the y = 0.75 samples, the y = 1.0 samples maintain their initial O3 structure on chemical delithiation due to the presence of a high nickel content. However, the delithiated z = 0.3 sample shows the formation of a P3 structure in addition to the initial O3 structure. This could be a result of high proton insertion with a relatively lower nickel content, as evident from the composition (b) given in the caption to Figure 6.10.

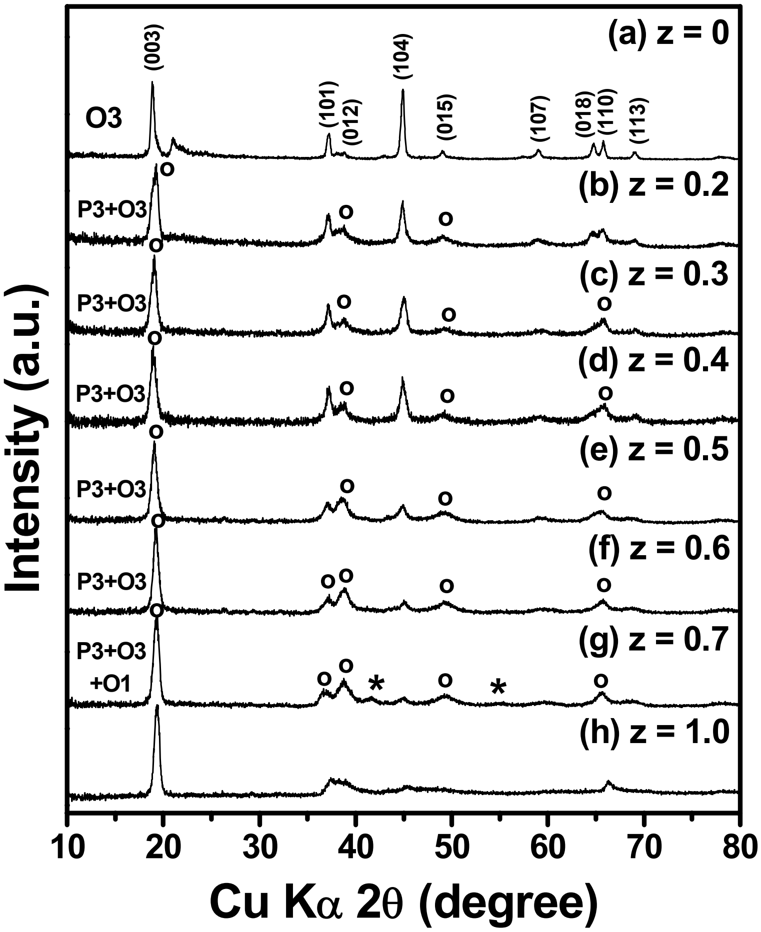

Figure 6.8: XRD patterns of the chemically delithiated samples obtained from the (1-z) $Li[Li_{1/3}Mn_{2/3}]O_2 \cdot$ (z) $Li[Co_{1-y}Ni_y]O_2$ (y = 0.5 and $0 \le z \le 1$) series synthesized at 750 °C. The reflections marked with hkl values refer to the layered O3 phase and those marked with o and * refer to the P3 and O1 phases, respectively. (a) $Li_{0.82}H_{0.13}[Li_{0.33}Mn_{0.67}]O_{1.99}$,
(b) $H_{0.48}[Li_{0.27}Mn_{0.53}Co_{0.1}Ni_{0.1}]O_{1.72}$,
(c) $H_{0.27}[H_{0.09}Li_{0.14}Mn_{0.47}Co_{0.15}Ni_{0.15}]O_{1.66}$,
(d) $H_{0.23}[H_{0.11}Li_{0.08}Mn_{0.41}Co_{0.2}Ni_{0.2}]O_{1.61}$,
(e) $H_{0.29}[H_{0.15}Li_{0.07}Mn_{0.35}Co_{0.25}Ni_{0.25}]O_{1.70}$,
(f) $H_{0.42}[H_{0.04}Li_{0.08}Mn_{0.27}Co_{0.31}Ni_{0.31}]O_{1.76}$,
(g) $H_{0.55}[Li_{0.07}Mn_{0.21}Co_{0.36}Ni_{0.36}]O_{1.86}$, and
(h) $Li_{0.07}H_{0.45}[Co_{0.5}Ni_{0.5}]O_{1.96}$.

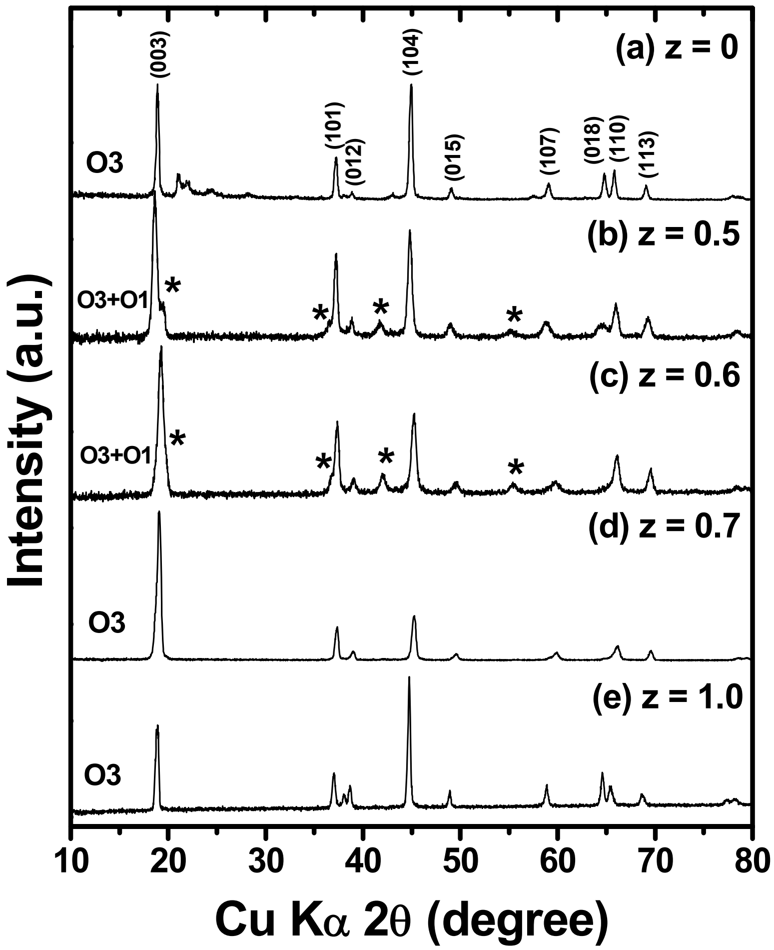

Figure 6.9: XRD patterns of the chemically delithiated samples obtained from the (1-z) $Li[Li_{1/3}Mn_{2/3}]O_2 \cdot$ (z) $Li[Co_{1-y}Ni_y]O_2$ ($y = 0.75$ and $0 \leq z \leq 1$) series synthesized at 900 °C. The reflections marked with hkl values refer to the layered O3 phase and those marked with * refer to the O1 phase.
(a) $Li_{0.98}H_{0.02}[Li_{0.33}Mn_{0.67}]O_{2.01}$, (b) $Li_{0.07}H_{0.18}[Li_{0.10}Mn_{0.36}Co_{0.13}Ni_{0.41}]O_{1.84}$,
(c) $Li_{0.07}H_{0.2}[Li_{0.04}Mn_{0.29}Co_{0.17}Ni_{0.5}]O_{1.92}$,
(d) $Li_{0.12}H_{0.14}[Li_{0.02}Mn_{0.22}Co_{0.19}Ni_{0.57}]O_{1.96}$, and
(e) $Li_{0.72}Ni_{0.1}[Co_{0.28}Ni_{0.72}]O_{1.99}$.

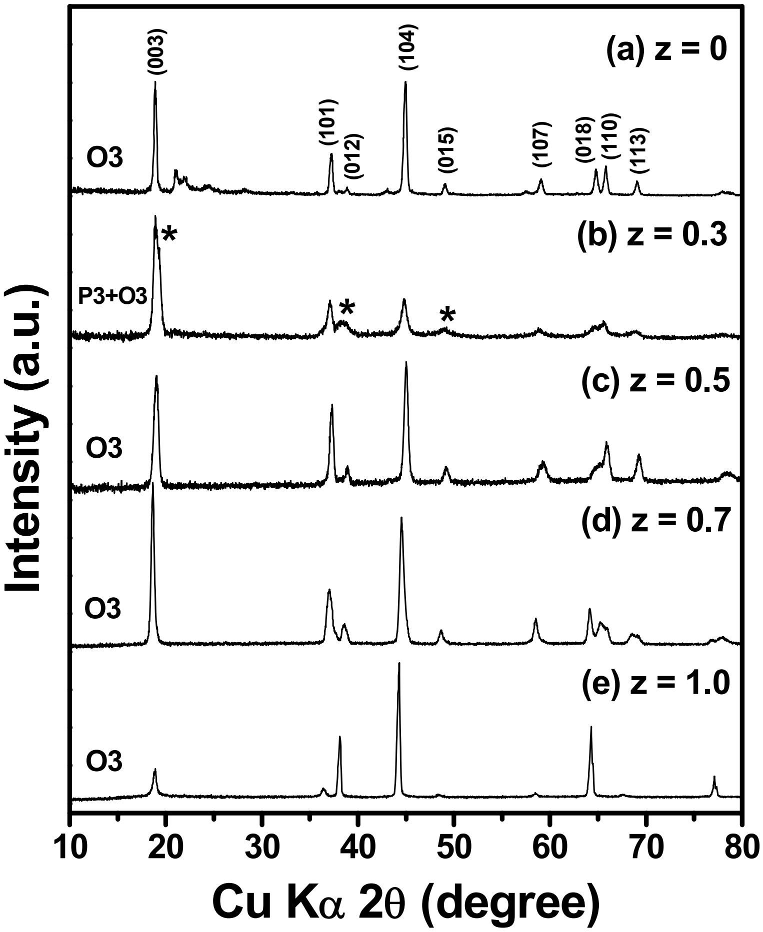

Figure 6.10: XRD patterns of the chemically delithiated samples obtained from the (1-z) $Li[Li_{1/3}Mn_{2/3}]O_2 \cdot$ (z) $Li[Co_{1-y}Ni_y]O_2$ (y = 1.0 and $0 \leq z \leq 1$) series synthesized at 900 °C. The reflections marked with hkl values refer to the layered O3 phase and those marked with * refer to the P3 phase. (a) $Li_{0.98}H_{0.02}[Li_{0.33}Mn_{0.67}]O_{2.01}$, (b) $Li_{0.02}H_{0.40}[Li_{0.2}Mn_{0.49}Ni_{0.31}]O_{1.82}$, (c) $Li_{0.12}H_{0.15}[Li_{0.08}Mn_{0.37}Ni_{0.55}]O_{1.90}$, (d) $Li_{0.47}Ni_{0.04}[Mn_{0.23}Ni_{0.77}]O_{1.97}$, and (e) $Li_{0.66}Ni_{0.15}[Ni]O_{1.80}$.

6.3.2 Influence of proton content and cation disorder on phase transformations

To understand the factors that influence the structural stability of the chemically delithiated (1-z) $Li[Li_{1/3}Mn_{2/3}]O_2 \cdot$ (z) $Li[Co_{1-y}Ni_y]O_2$ ($0 \leq y \leq 1$ and $0 \leq z \leq 1$) solid solution samples, we made a plot (Figure 6.11) of the degree of cation disorder versus the inserted proton content in all the delithiated samples investigated. Figure 6.11 also indicates the structure of each delithiated phase next to their respective icon.

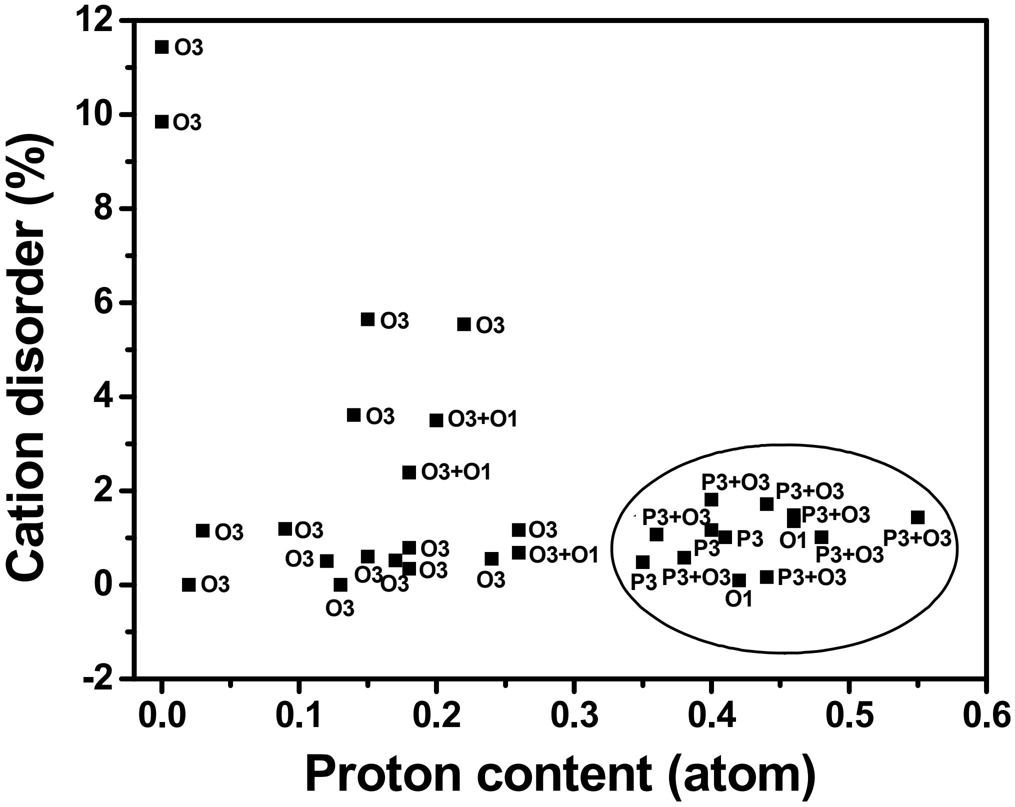

Figure 6.11: Proton content vs. cation disorder in the chemically delithiated (1-z) $Li[Li_{1/3}Mn_{2/3}]O_2 \cdot$ (z) $Li[Co_{1-y}Ni_y]O_2$ ($0 \leq y \leq 1$ and $0 \leq z \leq 1$) solid solution samples. The structure of each delithiated phase is shown next to their respective icon. The samples enclosed within the circle have predominantly either the P3 or O1 phases.

It is explicit from Figure 6.11 that the samples with lower cation disorder and higher proton content are more likely to transform to the P3 or O1 structure from their initial O3 structure. The samples enclosed within the circle in Figure 6.11 have either the P3 or O1 phase as predominant phases. As explained before, the presence of transition metal ions in the lithium plane due to a significant cation disorder in the parent layered samples may destabilize the formation of P3 and O1 type structures due to the electrostatic repulsion between the transition metal ions present in the lithium planes and transition metal planes across the shared polyhedral faces and thus a lithium plane free from transition metal cations may be necessary for the formation of the P3 and O1 type phases.[151]

In addition to the cation disorder, the proton content (ion exchange of Li^+ by H^+ occurring during chemical lithium extraction) could also possibly influence the structure of the delithiated phases. For example, the presence of protons in the layered oxides has been suggested before to favor the P3 type phase formation.[125] The hydrogen bonding between adjacent oxide ion layers has been proposed to be the driving force for the adoption of the P3 structure. Additionally, electrochemical lithium extraction (charging) of the solid solution cathodes in an actual lithium ion cell with a non-aqueous electrolyte does not yield the P3 or the O1 type structure at the end of charge. For example, the electrochemically charged ($y = 0$ and $z = 0.9$, and $y = 0.5$ and $z = 0.7$) cathodes (Figure 6.12) retain their initial O3 type structure, compared to a complete phase transformation to P3 or O1 structure on chemical delithiation (Figures 6.4 and 6.7). In essence, a lower cation disorder along with a significant proton insertion seems to favor the phase transformation of the initial O3 structure to the P3 or O1 structure. However, no clear evidence could be found as to why some compounds prefer to transform to the P3 structure and some prefer to transform to the O1 structure.

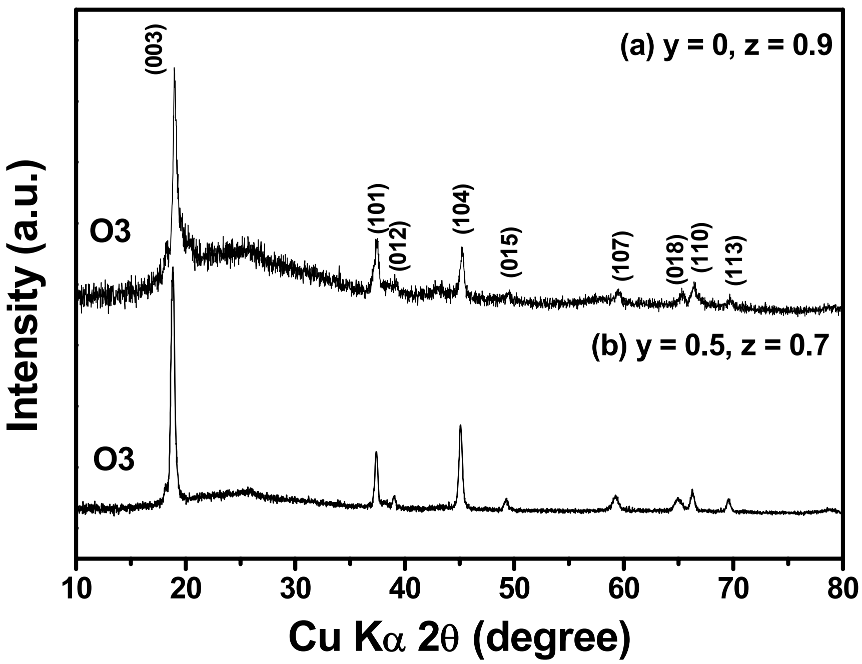

Figure 6.12: XRD patterns of the electrochemically charged (to 4.8 V at 12.5 mA/g) layered (1-z) $Li[Li_{1/3}Mn_{2/3}]O_2 \cdot (z) Li[Co_{1-y}Ni_y]O_2$ solid solution cathodes: (a) y = 0 and z = 0.9 and (b) y = 0.5 and z = 0.7.

Previous reports have attributed the formation of the metastable P3 phase to a faster lithium extraction caused by good cation ordering or larger surface area of the layered oxide samples, while a slow, more equilibrated lithium extraction leads to the formation of the thermodynamically more stable O1 type phase.[150] For example, the end member CoO_2 obtained by the electrochemical charging of $LiCoO_2$ cathodes has been reported to have either a single O1 type phase or a mixture of two O1 type phases.[152-154] On the other hand, CoO_2 obtained by the chemical extraction of lithium from $LiCoO_2$ with an oxidizer such as NO_2BF_4 in acetonitrile medium has been found to primarily have the metastable P3 type phase.[24,29] This discrepancy was attributed to the differences in the lithium extraction rates between the electrochemical and chemical lithium extraction processes,[29] since the electrochemical charging process is generally carried out at a much lower rate than the chemical lithium extraction. Similar considerations could be applied to the present set of samples as well.

6.4 CONCLUSIONS

The factors influencing the crystal chemistry of the layered phases formed on chemically extracting lithium from the (1-z) $Li[Li_{1/3}Mn_{2/3}]O_2 \cdot$ (z) $Li[Co_{1-y}Ni_y]O_2$ ($0 \leq y \leq 1$ and $0 \leq z \leq 1$) solid solution samples have been investigated. The delithiated samples adopt either the parent O3 type structure or the new P3 or O1 type structures depending upon the composition and synthesis temperature of the parent samples and the proton content inserted into the delithiated sample. While a high proton insertion resulting from a good cation ordering or a larger surface area seems to favor the transformation of the initial O3 structure to the P3 or O1 structure, a large degree of cation disorder prevents the formation of the P3 and O1 phases due to the strong electrostatic repulsion between the transition metal cations present in the lithium planes and transition metal planes across the shared polyhedral faces. In addition, the extent of oxygen loss in these chemically delithiated solid solution samples does not seem to have any influence on the formation of the P3 or O1 phases.

CHAPTER 7

Summary

With an aim to develop a better understanding of the chemical and structural factors that control the electrochemical performance properties such as the reversible capacity, cyclability, and rate capability of the 5 V spinel cathodes, various cation substituted $LiMn_{1.5-y}Ni_{0.5-z}M_{y+z}O_4$ (M = Li, Mg, Fe, Co, and Zn) spinel oxides have been investigated by chemically extracting lithium.

Cation substituted spinel $LiMn_{1.5-y}Ni_{0.5-z}M_{y+z}O_4$ cathodes exhibit superior capacity retention and rate capability in the 5 V region compared to the unsubstituted $LiMn_{1.5}Ni_{0.5}O_4$ cathode. For example, $LiMn_{1.42}Ni_{0.42}Fe_{0.16}O_4$, $LiMn_{1.42}Ni_{0.42}Co_{0.16}O_4$, and $LiMn_{1.5}Ni_{0.42}Zn_{0.08}O_4$ exhibit capacity fades of < 3 % in 50 cycles with 115-125 mAh/g at C/5 rate compared to 8 % fade and 131 mAh/g for $LiMn_{1.5}Ni_{0.5}O_4$. Also, $LiMn_{1.42}Ni_{0.42}Co_{0.16}O_4$ retains 92 % of its capacity on going from C/10 to 4C rate compared to 82 % for $LiMn_{1.5}Ni_{0.5}O_4$. The superior performances of these cation substituted cathodes are attributed to the smaller lattice parameter differences among the three cubic phases formed during the charge-discharge process. The smaller or negligible instantaneous volume change during the charge-discharge process is believed to suppress the stress involved and impart superior electrochemical properties. Further, the presence of Mn in the 4+ oxidation state seems to suppress its dissolution by disproportionation reaction and a clear correlation between the amount of Mn dissolved from the 5 V $LiMn_{1.5-y}Ni_{0.5-z}M_{y+z}O_4$ spinel cathodes and their electrochemical performance could not be established. The excellent performance with moderate reversible capacities of around

120 mAh/g along with the low cost, low toxicity, and ease of synthesis may make the 5 V $LiMn_{1.5-y}Ni_{0.5-z}M_{y+z}O_4$ cathodes attractive for electric and hybrid vehicle applications.

In addition, the possibility of proton incorporation into and oxygen loss from the lattice during the chemical delithiation process has been investigated with $Li_{1-x}Mn_{1.58}Ni_{0.42}O_4$ and $Li_{1-x}Co_2O_4$ spinel oxide cathodes. The spinel $Li_{1-x}Mn_{1.58}Ni_{0.42}O_4$ does not encounter any proton insertion or oxygen loss from the lattice at deep lithium extraction. However, the spinel $Li_{1-x}Co_2O_4$ exhibits both proton insertion and oxygen loss at deep lithium extraction. A significant overlap of the $Co^{3+/4+}$:3d band with the top of the O^{2-}:2p band results in an ion exchange of Li^+ by H^+ and an oxygen loss from the lattice at deep lithium extraction in $Li_{1-x}Co_2O_4$ to relieve the chemical instability while the lying of the $Mn^{3+/4+}$:3d and $Ni^{2+/4+}$:3d bands well above the O^{2-}:2p band in $Li_{1-x}Mn_{1.58}Ni_{0.42}O_4$ was believed to avoid such chemical instabilities.

The electrochemical charge-discharge properties of the layered (1-z) $Li[Li_{1/3}Mn_{2/3}]O_2 \cdot (z)\ Li[Co_{1-y}Ni_y]O_2$ solid solution cathodes have been investigated with an aim to identify the factors that control the amount of oxygen loss from the lattice during the first charge and the reversible capacity values. The charge profiles exhibit an initial sloping region A followed by a plateau region B around 4.5 V. The sloping region A is found to be determined by the initial average oxidation state of the transition metal ions and their oxidation to Ni^{4+} and $Co^{3.6+}$ with Mn remaining as Mn^{4+}. The plateau region B, which corresponds to an irreversible loss of oxygen from the lattice, is found to be determined by the amount of lithium η in the transition metal layer of the solid solution $Li[Li_\eta M_{1-\eta}]O_2$, by a chemical characterization of the chemically delithiated solid solution samples.. However, high Mn^{4+} content causes a decrease in oxygen mobility and loss. Moreover, the tendency of Ni^{3+} to get reduced to Ni^{2+} and the consequent volatilization of lithium during synthesis alter the lithium content in the transition metal layer and thereby influence the degree of oxygen loss and reversible capacity values. In essence, the study shows that the electrochemical performance factors of the layered (1-z) $Li[Li_{1/3}Mn_{2/3}]O_2 \cdot (z) Li[Co_{1-y}Ni_y]O_2$ solid solution cathodes could be maximized by optimizing the contents of the various ions.

In addition, the factors influencing the crystal chemistry of the layered phases formed on chemically extracting lithium from the (1-z) $Li[Li_{1/3}Mn_{2/3}]O_2 \cdot (z) Li[Co_{1-y}Ni_y]O_2$ solid solution samples have been investigated. Depending on the composition and synthesis temperature of the parent sample and the proton content inserted, the chemically delithiated samples adopt either the initial O3 type structure or the new P3 or O1 type structures. A significant cation disorder destabilizes the formation of the P3 and O1 type phases due to the strong electrostatic repulsion between the transition metal cations present in the lithium planes and transition metal planes across the shared polyhedral faces. However, a high proton insertion resulting from a good cation ordering or a larger surface area seems to favor the phase transformation of the initial O3 structure to the P3 or O1 structure.

A firm understanding of the factors affecting the chemical and structural stabilities of the lithium rich $Li[Li,Ni,Mn,Co]O_2$ solid solution oxides could help us to design cathode materials with high reversible capacities, which could possibly replace the presently used layered $LiCoO_2$. Future experiments could focus on optimization of the microstructure with novel synthesis and processing to improve the rate capabilities of these lithium rich layered oxide systems with high reversible capacities.

References

1. D. Linden, Ed., *Handbook of batteries*, 2nd edition, McGraw-Hill, NY (1995).

2. S. Srinivasan, B. B. Dave, K. A. Murugesamoorthi, A. Parthasarathy, and A. J. Appleby, *Overview of Fuel Cell Technology In Fuel Cell Systems*, M. J. Blomen and M. N. Mugerwa, Eds., Plenum Press, NY (1993).

3. B. E. Conway, *Electrochemical Supercapacitors*, Kluwer Academic/Plenum, NY (1999).

4. A. J. Bard and L. R. Faulkner, *Electrochemical Methods*, John Wiley and Sons (1980).

5. M. Wakihara, *Material Science and Engineering Reports*, **R33,** 109 (2001).

6. R. J. Brodd, *The Electrochemical Society Interface*, **3**, 20 (1999).

7. http://en.wikipedia.org

8. T. Nagaura, M. Nagamine, I. Tanabe, and N. Miyamoto, *Prog. Batt. Solar Cells*, **8**, 84 (1989).

9. T. Nagaura and K. Tozawa, *Prog. Batt. Solar Cells*, **9**, 209 (1990).

10. J. M. Tarascon and M. Armand, *Nature*, **414**, 359 (2001).

11. M. Wakihara and O. Yamamoto, Eds., *Lithium Ion batteries Fundamentals and performance*, Wiley-VCH (1998).

12. A. Manthiram and J. Kim, *Recent Res. Devel. Electrochem*., **2**, 31 (1999).

13. Orsini, A. du Pasquier, B. Beaudouin, J. M. Tarascon, M. Trentin, N. Langenhuizen, E. de Beer, and P. Notten, *J. Power Sources*, **81-82**, 918 (1999).

14. J. O. Besenhard, *Carbon*, **14**, 93 (1976).

15. M. S. Whittingham, *Science*, **192,** 1126 (1976).

16. K. Mizushima, P. C. Jones, P. J. Wiseman, and J. B. Goodenough, *Mat. Res. Bull.* **15,** 783 (1980).

17. K. Mizushima, P. C. Jones, P. J. Wiseman, and J. B. Goodenough, *Solid state ionics*. **3/4**, 171 (1981).

18. J. B. Goodenough, K. Mizushima, and T. Takeda, *Jpn. J. Appl. Phys.*, **19,** 305 (1983).

19. M. M. Thackeray, W. I. F. David, P. G. Bruce, and J. B. Goodenough, *Mat. Res. Bull.* **18,** 461 (1983).

20. C. Delmas, C. Fouassier, and P. Hagenmuller, *Physica*, **99B**, 81 (1980).

21. A. Manthiram, in *New Trends in Intercalation Compounds for Energy Storage*, p. 177, C. Julien, J. P. Pereira-Ramos, and A. Momchilov Editors, Kluwer Academic Publisher, Netherland (2002).

22. S. Choi and A. Manthiram, *J. Electrochem. Soc*., **149**, A1157 (2002).

23. R. V. Chebiam, A. M. Kannan, F. Prado, and A. Manthiram, *Electrochem. Commun.*, **3**, 624 (2001).

24. R. V. Chebiam, F. Prado and A. Manthiram, *Chem. Mater.*, **13**, 2951 (2001).

25. L. Croguennec, C. Pouillerie, and C. Delmas, *J. Electrochem. Soc.*, **147**, 1314 (2000).

26. L. Croguennec, C. Pouillerie, A. N. Mansour, and C. Delmas, *J. Mater. Chem.*, **11**, 131 (2001).

27. A. Van der Ven, M. K. Aydino, G. Ceder, G. Kresse, and J. Hafner, *J. Phys. Rev. B*, **58**, 2975 (1998).

28. A. Van der Ven, M. K. Aydino, and G. Ceder, *J. Electrochem. Soc.*, **145**, 2149 (1998).

29. S. Venkatraman and A. Manthiram, *Chem. Mater.*, **14**, 3907 (2002).

30. I. Nakai, K. Takahasi, Y.Shiraishi, T. Nakagone, and F. Nishikawa, *J. Solid State Chem.*, **140**, 145, (1998).

31. G. Dutta, A. Manthiram, and J. B. Goodenough, *J. Solid State Chem.*, **96**, 123 (1992).

32. J. Morales, C. Perez-Vincente, and J. L. Tirado, *Mat. Res. Bull.*, **25**, 623 (1990).

33. H. Arai, S. Okada, H. Ohtsuka, M. Ichimura, and J. Yamaki, *Solid State Ionics*, **80**, 261 (1995).

34. J. E. Huheey, *Inorganic Chemistry: Principles of structure and Reactivity*, Harper & Row, NY (1972).

35. W. Li and J. Curie, *J. Electrochem.Soc.*, **144,** 2773 (1997).

36. E. Zhecheva and R. Stoyanova, *Solid State Ionics*, **66**, 143 (1993).

37. C. Delmas, I. Saadoune, and A. Rougier, *J. Power Sources*, **43-44**, 595 (1993).

38. T. Ohzuku, A. Ueda, M. Nagayama, Y. Iwakoshi and H. Komori, *Electochem. Acta.*, **38**, 1159 (1993).

39. M. M. Thackeray, P. J. Johnson, L. A. De Picciotto, P. G. Bruce, and J. B. Goodenough, *Mater. Res. Bull.*, **19**, 179, (1984).

40. M. M. Thackeray, L. A. De Picciotto, A. De Kock, P. J. Johnson, V. A. Nicholas, and K. T. Adendorff, *J. Power Sources.*, **21**, 1 (1987).

41. G. Pistoia and D. Wang, *Solid State Ionics*, **66**, 135 (1993).

42. M. M. Thackeray, *J. Electrochem. Soc.*, **142**, 2558 (1995).

43. M. K. Aydinol and G. Ceder, *J. Electrochem. Soc.*, **144,** 3832 (1997).

44. R. J. Gummow, A. De Kock, and M. M. Thackeray, *Solid State Ionics*, **69,** 59 (1994).

45. M. M. Thackeray, *J. Am. Ceram. Soc.*, **82,** 3347 (1999).

46. D. H. Jang, Y. J. Shin, and S. M. Oh, *J. Electrochem. Soc.*, **143**, 2204 (1996).

47. M. M. Thackeray, Y. Shoa-Horn, A. J. Kahaian, K. D. Kepler, E. Skinner, J. T. Vaughey, and S. A. Hackney, *Electrochem. Solid-state Lett.,* **1**, 7 (1998).

48. Y. Xia and M. Yoshio, *J. Electrochem. Soc.*, **143**, 825 (1996).

49. Y. Shin and A. Manthiram, *Electrochem. Solid-state Lett.,* **5**, A55 (2002).

50. Y. Shin and A. Manthiram, *Electrochem. Solid-state Lett.,* **6**, A34 (2003).

51. Y. Shin and A. Manthiram, *Chem. Mater.*, **15**, 2954 (2003).

52. Y. Shin and A. Manthiram, *J. Electrochem. Soc.,* **151**, A204 (2004).

53. A. de Kock, M. H. Rossouw, L. A. de Picciotto, M. M. Thackeray, W. I. F. David, and R. M. Ibberson, *Mat. Res. Bull.*, **25**, 657 (1990).

54. M. H. Rossouw, A. de Kock, L. A. de Picciotto, M. M. Thackeray, W. I. F. David, and R. M. Ibberson, *Mat. Res. Bull.*, **25**, 173 (1990).

55. S. Choi and A. Manthiram, *J. Electrochem. Soc.*, **147**, 1623 (2000).

56. J. Kim and A. Manthiram, *J. Electrochem. Soc.*, **145**, L53 (1998).

57. F. G. B. Ooms, E. M. Kelder, J. Schoonman, M. Wagemaker, and F. M. Mulder, *Solid State Ionics*, **152**, 143 (2002).

58. R. Alcantara, M. Jaraba, P. Lavela, and J. L. Tirad, *J. Electrochem. Soc.*, **151**, A53 (2004).

59. K. Hong and Y. Sun, *J. Power Sources*, **109**, 427 (2002).

60. R. Alcantara, M. Jaraba, P. Lavela, and J. L. Tirad, *J. Electroanal. chem.,* **566**, 187 (2004).

61. Q. Zhong, A Banakdarpour, M. Zhang, Y. Gao, and J.R. Dahn, *J. Electrochem. Soc.* **144**, 205 (1997).

62. K. Ariyoshi, Y. Iwakoshi, N. Nakayama, and T. Ohzuku, *J. Electrochem. Soc.*, **151**, A296 (2004).

63. J. H. Kim, C. S. Yoon, S. T. Myung, J. Prakash, and Y. K. Sun, *Electrochem. Solid-State Lett.,* **7**, A216 (2004).

64. S. Mukerjee, X. Q. Yang, X. Sun, S. J. Lee, J. McBreen, and Y. Ein-Eli, *Electrochimica Acta*, **49**, 3373 (2004).

65. M. N. Obrovac, Y. Gao, J. R. Dahn, *Phys. Rev. B*, **57,** 5728 (1998).

66. C. Sigala, D. Guyomard, A. Verbaere, Y. Diffard, and M. Tournoux, *Solid State Ionics*, **81,** 167 (1995).

67. H. Kawai, M. Nagata, M. Tabuchi, H. Tukamoto, and A. R. West, *Chem. Mater.,* **10,** 3266 (1998).

68. H. Shigemura, H. Sakaebe, H. Kageyama, H. Kobayashi, A. R. West, R. Kanno, S. Morimoto, S. Nasu, and M. Tabuchi, *J. Electrochem. Soc.*, **148,** A730 (2001).

69. H. Kawai, M. Nagata, H. Tukamoto, H. Kageyama, and A. R. West, *Electrochim. Acta*, **45**, 315 (1999).

70. Y. Gao, K. Myrtle, M. Zhang, J. N. Reimers, and J. R. Dahn, *Phys. Rev. B*, **54**, 16670, (1996).

71. Y. Ein-Eli and W. F. Howard, Jr., *J. Electrochemical Soc.*, **144,** L205 (1997).

72. Y. Ein-Eli, W. F. Howard, Jr., S. H. Lu, S. Mukerjee, J. McBreen, J. T. Vaughey, and M. M. Thackeray, *J. Electrochemical Soc.*, **145,** 1238 (1998).

73. Y. Ein-Eli, J. T. Vaughey, M. M. Thackeray, S. Mukerjee, X. Q. Yang, and J. McBreen, *J. Electrochemical Soc.*, **146,** 908 (1999).

74. H. Kawai, M. Nagata, H. Tukamoto, and A. R. West, *J. Power Sources*, **81-82**, 67, (1999).

75. T. Ohzuku, S. Takeda, and M. Iwanaga, *J. Power Sources*, **81-82**, 90 (1999).

76. K. Amine, H. Tukamoto, H. Yasuda, and Y. Fujita, *J. Power Sources*, **68,** 604 (1997).

77. C. Wu, F. Wu, L. Chen, and X. Huang, *Solid State Ionics*, **152-153**, 335 (2002).

78. K. A. Striebel, A. Rougier, C. R. Horne, R. P. Reade, and E. J. Cairns, *J. Electrochem. Soc.*, **146,** 4339 (1999).

79. M. Wakihara, Li Guohua, H. Ikuta, and T. Uchida, *Solid State Ionics*, **86-88**, 907 (1996).

80. E. Iwata, K. Takahashi, K. Maeda, and T. Mouri, *J. Power Sources*, **81-82**, 430 (1999).

81. A. Manthiram and J. B. Goodenough, *J. Power sources*, **26**, 403 (1989).

82. A. K. Padhi, K. S. Nanjundaswamy, and J. B. Goodenough, *J. Electrochem. Soc.*, **144**, 1188 (1997).

83. A. K. Padhi, K. S. Nanjundaswamy, C. Masquelier, S. Okada, and J. B. Goodenough, *J. Electrochem. Soc.*, **144**, 1609 (1997).

84. H. Huang, S. C. Yin, and L. F. Nazar, *Electrochem. Solid State Lett.*, **4**, A170 (2001).

85. G. T. Fey, W. Li, and J. R. Dahn, *J. Electrochem. Soc.*, **141**, 2279 (1994).

86. S. Panero, P. Reale, F. Bonino, B. Scrosati, M. Arrabito, S. Bodoardo, D. Mazza, and N. Penazzi, *Solid State Ionics*, **128**, 43 (2000).

87. K. Amine, H. Yasuda, and M. Yamachi, *Electrochem. Solid-State Lett.*, **3**, 178 (2000).

88. D. W. Murphy, P. A. Christian, and J. N. Carides, *J. Electrochem. Soc.*, **126**, 497 (1979).

89. C. Tsang and A. Manthiram, *J. Electrochem. Soc.*, **144**, 520 (1997).

90. O. Yamamoto, Y. Takeda, R. Kanno, Y. Oyabe, and Y. Shinya, *J. Power Sources*, **20**, 151, (1987).

91. J. Kim and A. Manthiram, *J. Electrochem. Soc.*, **144**, 3077 (1997).

92. A. Manthiram and J. Gopalakrishnan, *Rev. Inorg. Chem.* **6**, 1 (1984).

93. M. Winter, J. O. Besenhard, M. E. Spahr, and P. Novak, *Adv. Mater.*, **10**, 725 (1998).

94. D. W. Murphy, M. Greenblatt, S. M. Zahurak, R. J. Cava, J. V. Waszczak, G. W. Hull, and R. S. Hutton, *Rev. Chim. Miner.*, **19**, 441 (1982).

95. P. P. Prosini, R. Mancini, L. Petrucci, V. Contini, and P. Villano, *Solid State Ionics*, **144**, 185 (2001).

96. H. Morimoto, M. Nakai, M. Tatsumisago, and T. Minami, *J. Electrochem. Soc.*, **146**, 3970 (1999).

97. N. P. Yao, L. A. heredy, and R. C. Saunders, *J. Electrochem. Soc.*, **118**, 1039 (1971).

98. C. J. Wen, B. A. Boukamp, R. A. Huggins, and W. Weppener, *J. Electrochem. Soc.*, **126**, 2258 (1979).

99. S. Megahed and B. Scrosati, *J. Power Sources*, **51**, 79 (1994).

100. J. M. Tarascon and D. Guyomard, *Solid State Ionics*, **69**, 293 (1994).

101. W. H. Meyer, *Adv. Mater.*, **10**, 439 (1998).

102. R. C. Laman, M. A. Gee, and J. Denovan, *J. Electrochem. Soc.*, **140**, L51 (1993).

103. K. Ozawa, *Solid State Ionics*, **69**, 212 (1994).

104. R. Wizansky, P. E. Rauch, and F. J. DiSalvo, *J. Solid State Chem.*, **81**, 203 (1989).

105. Y. Xia, Y. Zhou, and M. Yoshio, *J. Electrochem. Soc.*, **144**, 2593 (1997).

106. T. Inoue and M. Sano, *J. Electrochem. Soc.*, **145**, 3704 (1998).

107. R. A. Young, *The Rietveld Method*, Oxford University Press, New York (1993).

108. R. A. Young, A. Shakthivel, T. S. Moss, and C. O. Paiva Santos, *J. Appl. Crystallogr.*, **28**, 366 (1995).

109. M. J. Katz, R. C. Clarke, and W. F. Nye, *Anal. Chem.*, **28**, 507 (1956).

110. S. K. Aghara, S. Venkatraman, and A. Manthiram, *J. Radioanal. Nucl. Chem.*, **265**, 321 (2005).

111. R. L. Paul and R. M. Lindstrom, *J. Radioanal. Nucl. Chem.*, **243**, 181 (2000).

112. W. Choi and A. Manthiram, *Journal of the Electrochemical Society*, **153**, A1760 (2006).

113. W. Li and J. C. Currie, *J. Electrochem. Soc.*, **144**, 2773 (1997).

114. T. Ohzuku and Y. Makimura, *Chem. Lett.,* 744 (2001).

115. T. Ohzuku and Y. Makimura, *Chem. Lett.,* 642 (2001).

116. Z. Lu, D. D. Macneil, and J. R. Dahn, *Electrochem. Solid State Lett.,* **4**, A191 (2001).

117. N. Yabuuchi and T. Ohzuku, *J. Power Sources*, **119-121**, 171 (2003).

118. J. Choi and A. Manthiram, *Electrochem. Solid State Lett.,* **7**, A365 (2004).

119. J. Kim and H. Chung, *Electrochimica Acta,* **49**, 937 (2004).

120. R. V. Chebiam, F. Prado, and A. Manthiram, *J. Solid State Chem.*, **163**, 5 (2002).

121. S. Venkatraman, Y. Shin, and A. Manthiram, *Electrochem. Solid State Lett.,* **6**, A9 (2003).

122. S. Venkatraman and A. Manthiram, *Chem. Mater.*, **15**, 5003 (2003).

123. J. Choi and A. Manthiram, *J. Electrochem. Soc.*, **152**, A1714 (2005).

124. W. Martindale, in *Martindale: The Complete Drug Reference,* 34th edition, p. 1471, S. C. Sweetman, Editor, The Pharmaceutical Press, London (2005).

125. A. D. Robertson and P. G. Bruce, *Chem. Mater.*, **15**, 1984 (2003).

126. A. D. Robertson and P. G. Bruce, *Electrochem. Solid State Lett.*, **7**, A294 (2004).

127. J. Choi, E. Alvarez, T. A. Arunkumar, and A. Manthiram, *Electrochem. Solid State Lett.*, **9**, A241 (2006).

128. R J. Gummow, M. M. Thackeray, W. I. F. David, and S. Hull, *Mater. Res. Bull.,* **27**, 327 (1992).

129. R. J. Gummow, D. C. Liles, and M. M. Thackeray, *Mater. Res. Bull.*, **28**, 235 (1993).

130. S. Choi and A. Manthiram, *J. Electrochem. Soc.*, **149**, A162 (2002).

131. S. Choi and A. Manthiram, *J. Solid State Chem.* **164**, 332 (2002).

132. S. H. Kang, Y. K. Sun, and K. Amine, *Electrochem. Solid-State Lett.,* **6**, A183 (2003).

133. Y. J. Park, Y. S. Hong, X. Wu, K. S. Ryu, and S. H. Chang, *J. Power Sources,* **129**, 288 (2004).

134. A. R. Armstrong, M. Holzapfel, P. Novak, C. S. Johnson, S. Kang, M. M. Thackeray, and P. G. Bruce, *J. Am. Chem. Soc.,* **128**, 8694 (2006).

135. Y. Wu and A. Manthiram, *Electrochem. Solid State Lett.*, **9**, A221 (2006).

136. K. Numata, C. Sakaki, and S. Yamanaka, *Solid State Ionics,* **117**, 257 (1999).

137. Y. J. Park, X. Wu, Y. S. Hong, K. S. Ryu, and S. H. Chang, *Solid State Ionics,* **175**, 305 (2004).

138. L. Zhang, H. Noguchi, and M. Yoshio, *J. Power Sources,* **110**, 57 (2002).

139. P. S. Whitfield, S. Niketic, and I. J. Davidson, *J. Power Sources,* **146**, 617 (2005).

140. Z. Lu and J. R. Dahn, *J. Electrochem. Soc.,* **149**, A815 (2002).

141. Y. Wu and A. Manthiram, *Electrochem. Solid State Lett.*, **10**, A151 (2007).

142. R. D. Shannon, *Acta Cryst.,* **A32**, 751 (1976).

143. Y. Shin and A. Manthiram, *Electrochimica Acta*, **48**, 3583 (2003).

144. R. J. Gummow, M. M. Thackeray, W. I. F. David, and S. Hull, *Mat. Res. Bull.*, **27**, 327 (1992).

145. Y. Shao-Horn, S. A. Hackney, C. S. Johnson, A. J. Kahaian, and M. M. Thackeray, *J. Solid State Chem.*, **140**, 116 (1998).

146. Z. Lu, L. Y. Beaulieu, R. A. Donaberger, C. L. Thomas, and J. R. Dahn, *J. Electrochem. Soc.*, **149**, A778 (2002).

147. Z. Lu and J. R. Dahn, *J. Electrochem. Soc.*, **149**, A1454 (2002).

148. D. Carlier, I. Saadoune, L. Croguennec, M. Menetrier, E. Suard, and C. Delmas, *Solid State Ionics,* **144**, 263 (2001).

149. M. Butel, L. Gautier, C. Delmas, *Solid State Ionics,* **122**, 271 (1999).

150. J. Choi and A. Manthiram, *J. Materials Chemistry*, **16**, 1726 (2006).

151. S. Venkatraman and A. Manthiram, *Solid State Ionics*, **176**, 291 (2005).

152. G. G. Amatucci, J. M. Tarascon, L. C. Klein, *J. Electrochem. Soc.*, **143**, 1114 (1996).

153. X. Q. Yang, X. Sun, J. Mcbreen, *Electrochem. Commun.*, **2**, 100 (2000).

154. J. M. Tarascon, G. Vaughan, Y. Chabre, L. Seguin, M. Anne, P. Strobel, G. Amatucci, *J. Solid State Chem.*, **147**, 410 (1999).

Vita

Arun Kumar Tiruvannamalai Annamalai was born in Tiruvannamalai, India, on May 14, 1981, the son of Annamalai and Tamilarasi. After completing his work at Mount Saint Joseph Higher Secondary School, Tiruvannamalai, India, he entered Central Electrochemical Research Institute, Karaikudi, India, in 1998. After receiving his Bachelor of Technology degree in 2002, he entered the graduate school of The University Of Texas at Austin in Fall 2002 and received his Master of Science degree in May 2004.

Permanent address: 29/12, 10th street, Gandhinagar, Tiruvannamalai, India 606602.
This dissertation was typed by the author.